

EXPLOSIVE EVENTS IN THE QUIET SUN: EXTREME ULTRAVIOLET
IMAGING SPECTROSCOPY INSTRUMENTATION AND OBSERVATIONS

by

Thomas Ludwell Rust

A dissertation submitted in partial fulfillment
of the requirements for the degree

of

Doctor of Philosophy

in

Physics

MONTANA STATE UNIVERSITY
Bozeman, Montana

July 2017

©COPYRIGHT

by

Thomas Ludwell Rust

2017

All Rights Reserved

DEDICATION

To my parents Dr. Robert S. and Elizabeth M. Rust – the sacrifices you both have made for me are unfathomable.

To Yvette Converse for the strength, inspiration and happiness you have given me.

In appreciation of the wonders of nature, evidenced nowhere better than in the mountains and skies of Montana.

ACKNOWLEDGEMENTS

This work would not have been possible without support from Dr. Charles Kankelborg. Thank you for the opportunities you have given me, for sharing your ideas and helping me to develop mine. Thanks to committee members Dr. Dana Longcope for help with magnetic context, Dr. Piet Martens for help with physical properties of explosive events, Dr. David McKenzie for help with the presentation of scientific results, Dr. Carla Riedel for help with wavelet methods, and Dr. Joe Shaw for help with optical testing. Thanks for providing feedback which has improved this document. The *MOSES* missions are collective efforts. Thanks in particular to MSU team members J. L. Fox, P. Lokken, R. Smart, H. Courrier, K. Mashburn, J. Plovanic, J. Knoll, M. Norton, J. Maxwell and E. Barth for their contributions. It was my privilege to work with the NSROC team and WSMR staff leading up to the *MOSES-15* launch. MSU Physics Department staff greatly assisted this work: M. Jarrett, S. Heis, B. Glaspey, J. Gay and S. Barutha. N. Williams provided technical support for the optomechanics work. Thanks to Dr. K. Yoshimura for his maintenance of the Solar Group computational servers. Thanks to my parents R. and E. M. Rust for providing a loving home and good education. Y. Converse has been a supportive partner and friend through consuming work. Thanks to B. Carlson for her support of my education. I have been blessed with many good friends. Of those, Y. Converse, M. Jarrett, J. Forbes, Dr. C. Key, Dr. J. Scott, and Dr. N. Childs have given of themselves to directly support me in this work; may I always be there for them.

TABLE OF CONTENTS

1. INTRODUCTION	1
1.1 The Solar Atmosphere	1
1.1.1 The Photosphere	1
1.1.2 The Photospheric Magnetic Field	2
1.1.3 The Chromosphere	2
1.1.4 The Corona	3
1.1.5 The Transition Region	5
1.2 Transition Region Explosive Events	7
1.2.1 Explosive Event Magnetic Reconnection Models	9
1.2.2 Observational Challenges	11
1.3 The <i>Multi-Order Solar Extreme ultraviolet Spectrograph (MOSES)</i>	13
1.3.1 Concept: Slitless Spectroscopy.....	13
1.3.2 Image Model	15
1.3.3 Flight History.....	17
1.3.4 Spectral Passband	17
1.4 Summary of Dissertation Chapters.....	19
2. QUIET SUN EXPLOSIVE EVENTS OBSERVED IN HE II 304 Å WITH MOSES-06	21
2.1 Data	23
2.2 Data Reduction	25
2.2.1 Co-alignment.....	25
2.2.1.1 \mathcal{I}_{-1} and \mathcal{I}_{+1} to \mathcal{I}_0	25
2.2.1.2 \mathcal{I}_0 to SOHO-EIT 304 Å	26
2.2.2 Normalization.....	26
2.3 Difference Images.....	33
2.4 Explosive Event Examples.....	42
2.4.1 Blue Jet Rise Phase	48
2.4.2 Bi-Directional Jet Rise Phase	51
2.4.3 Doppler Shift Estimates	56
2.4.4 Magnetic Context	59
2.4.5 Mass and Kinetic Energy Flux.....	63
2.5 Additional Explosive Event Examples	64
2.6 Summary	69
2.7 Acknowledgements	72

TABLE OF CONTENTS – CONTINUED

3. A NEW TECHNIQUE FOR <i>MOSES</i> INVERSIONS.....	73
3.1 Introduction	73
3.2 Synthetic Data	74
3.3 The Multiplicative Algebraic Reconstruction Technique	77
3.4 Testing MART with Synthetic Data.....	77
3.5 MART with Partial Reconstruction	82
3.6 MART, Partial Reconstruction and Deconvolution.....	88
3.7 Conclusions	95
4. INVERSION OF A BI-DIRECTIONAL JET IN <i>MOSES-06</i>	97
4.1 Data	98
4.2 Partial Reconstruction of a Bi-directional Jet	99
4.3 Inversion of a Single Frame	104
4.4 Time Evolution	108
4.5 Discussion	113
5. OPTICAL TESTING AND INTEGRATION OF <i>MOSES-15</i>	116
5.1 Optical Design.....	116
5.1.1 Changes from <i>MOSES-06</i>	119
5.2 Mirror Mounts.....	120
5.3 Testing Tools.....	121
5.3.1 Theodolite.....	121
5.3.2 Interferometer	121
6. <i>MOSES-15</i> OPTICAL TESTING	123
6.1 <i>MOSES-15</i> Primary Mirror	123
6.1.1 Radius of Curvature.....	123
6.1.2 Figure.....	124
6.1.3 Grating Figure Correction	125
6.2 <i>MOSES-15</i> Secondary Mirror	127
6.2.1 Wedge Angle	127
6.2.2 Figure	127
7. <i>MOSES-15</i> ALIGNMENT AND FOCUS.....	131
7.1 Alignment	132
7.1.1 Secondary to LOTS	132

TABLE OF CONTENTS – CONTINUED

7.1.2 Primary to Filter Tube Target	133
7.2 Focus	134
7.3 Image Quality Results.....	136
7.4 Grating Roll Measurement	137
8. OPTICAL MODELING	140
8.1 Fourier Optics Model	140
8.2 Results – Optical Prescriptions	142
8.3 Point Spread Functions	143
8.3.1 EUV, Modeled.....	143
8.3.2 Visible Light, Measured and Modeled	146
8.4 Distortion Modeling.....	147
8.5 Acknowledgements.....	149
REFERENCES CITED.....	151
APPENDICES	156
APPENDIX A : Movies	157
APPENDIX B : The Wavelet Transform.....	160
B.1 The Continuous Wavelet Transform	161
B.2 The À Trous Discrete Wavelet Transform.....	162
B.2.1 Significance Testing of Discrete Wavelet Coefficients	165
APPENDIX C : Noise Modeling.....	167
C.1 Introduction	168
C.2 Theory.....	168
C.3 Methods.....	172
C.3.1 Light Source.....	172
C.3.2 Data	172
C.4 Analysis	173
C.4.1 Read Noise and Pedestal Measurement	173
C.4.2 Signal Mean and Variance Measurement	174
C.5 Results.....	175
C.6 Noise at Operating Wavelength	182
C.6.1 Noise Power Spectra	185
C.6.2 EUV Noise in Wavelet Space	187
C.7 Acknowledgements.....	190
APPENDIX D : MOSES-06 Point Spread Functions	191
D.1 Introduction	192

TABLE OF CONTENTS – CONTINUED

D.2	Partial Reconstruction	193
D.3	Data	194
D.4	PSF Results	197
D.5	Temporal Variation.....	199
D.6	Additional Compact Sources	201
D.7	Conclusion	201

LIST OF TABLES

Table	Page
1.1 Explosive event properties from Dere (1994). QS stands for quiet sun and CH stands for coronal hole.....	8
1.2 Calibrated active region line list within <i>MOSES-06</i> full width half maximum passband, from Brosius et al. (1998). Intensity shown relative to the He II 304 Åline intensity.....	19
2.1 Spectrograph specifications for the <i>MOSES-06</i> flight.	24
2.2 Catalog of <i>MOSES-06</i> data exposures from Hans Courrier and Roger J. Thomas analysis of strip chart records made during the flight. Table adapted from Fox (2011).	25
2.3 Jet speeds derived from gaussian fits.	59
2.4 Estimates for the upwards mass and kinetic energy flow from the blue jet and bi-directional jet.	64
4.1 Moments of the spatial distribution of $\nu(x, y, -3)$ (blue wing), $\nu(x, y, +3)$ (red wing), and $\nu(x, y, 0)$ (low velocity component) of the inverted bi-directional jet (figure 4.1). Peak radiance is in relative units (DN). The spatial coordinates are given in km. The centroids denoted by $\langle * \rangle$ are given with respect to the center of the inversion spatial domain.	106
4.2 Line shifts, widths and percentage of the total intensity in each of the spectral components discussed in the text.	107
5.1 Optical prescription for the <i>MOSES-15</i> spectrograph. X, Y, and Z are in units of mm. The coordinate axes are depicted in figure 5.1. Pitch and yaw are right hand rotations about the y and z axes, respectively, and are given in degrees.....	118
6.1 Summary of test results for <i>MOSES-15</i> secondary mirror.	130
8.1 <i>MOSES-06</i> design table from Fourier optics model, using grating and secondary position and orientation from Fox (2011). Grating radius of curvature is 9.48 m and grating pitch is 950 l/mm. Angles given are in degrees, and positions in mm.	142

LIST OF TABLES – CONTINUED

Table	Page
8.2 <i>MOSES-15</i> design table from Fourier optics model after moving secondary towards detectors to compensate for change in grating focal length, and adjusting the tip of the grating and secondary equally to center the detectors at z=0 . Grating radius of curvature is 9.295 m and grating pitch is 621 l/mm. Angles given are in degrees, and positions in mm.	143
C.1 Noise Model Parameters. See equation C.3.	182
C.2 Charge Diffusion Kernel κ . Values represent the probability of a free electron being captured by a pixel in the neighborhood of the interaction site.	187
C.3 Wavelet space significance levels from the à trous transform. Size scale decreases as j increases.	190

LIST OF FIGURES

Figure		Page
1.1	S082A slitless spectrograph data in the 200-400 Å spectral range. The bright disk in the upper right hand corner is the transition region He II 304 Å spectral line. Image from (Tousey et al., 1973).....	14
2.1	<i>Upper panel:</i> EIT 304 Å image cropped to the MOSES-06 field of view. <i>Lower panel:</i> \mathcal{I}_0 , exposure number $n = 13$, following data reduction and co-alignment. Both images have been logarithmically scaled after clipping the brightest and darkest 0.3% of all pixels.....	27
2.2	<i>Upper panel:</i> \mathcal{I}_{+1} , and <i>Lower panel:</i> \mathcal{I}_{-1} , exposure number $n = 13$, following data reduction and co-alignment. The images are logarithmically scaled with the same clipping used for the \mathcal{I}_0 image in figure 2.1. Again, north is up, west is right, and the spectrograph dispersion is along the E-W axis. The black pixels located in the center of the bright region at about [20°W, 75°S] are saturated.....	29
2.3	<i>Upper panel:</i> EIT 171 Å, and <i>Lower panel:</i> EIT 284 Å, cropped to MOSES-06 field of view. Images are logarithmically scaled with 0.3% clipping	31
2.4	Line of sight magnetic field measured by MDI. The display is linearly scaled and clipped at about ± 80 gauss. Positive polarity magnetic elements are white and negative polarity elements are black. Grey regions are regions with weak or no magnetic field. The data have been differentially rotated backwards by two hours; see text.	32
2.5	Example difference images $d_{(0,-1)} = \mathcal{I}_0 - \mathcal{I}_{-1}$ (top) and $d_{(0,+1)} = \mathcal{I}_0 - \mathcal{I}_{+1}$ (bottom). Light colors indicate positive differences, dark colors indicate negative differences. The images are displayed on a linear scale and have been clipped at three standard deviations to show faint details.	34
2.6	Scale $j = 6$ wavelet coefficients of $d_{(0,+1)}$. Overplotted arrows show the expected shifts from emission at Si IX/Fe VI 296.1 Å (blue) and Mg VIII 315.0 Å (red).	36

LIST OF FIGURES – CONTINUED

Figure	Page
2.7 Close up of the coronal hole in the <i>MOSES-06</i> data showing the small scale structure of the region. Clockwise from upper left: log scaled \mathcal{I}_0 intensity, difference image $d_{(0,-1)}$, the scale $j = 2$ wavelet coefficients $\tilde{d}_{(0,-1)}^2$, and the $j = 2$ wavelet coefficients $\tilde{\mathcal{I}}_z^2$. The 3σ contours of $\tilde{d}_{(0,-1)}^2$ are overplotted onto the $\tilde{\mathcal{I}}_z^2$ image. Blue contours are positive differences and red contours are negative.	37
2.8 Close up of a region of quiet sun. See figure 2.7 for a description of the different panels.	38
2.9 Close up of a quiet sun region with relatively strong underlying magnetic network. See figure 2.7 for a description of the different panels.	39
2.10 Difference image $\mathcal{I}_{+1} - \mathcal{I}_{-1}$ from (Fox, 2011) showing how different point spread functions \mathcal{P}_m in <i>MOSES-06</i> different channels manifest themselves as strong signatures in difference images.	41
2.11 Snapshots of three compact objects in the <i>MOSES-06</i> data. Each row shows a different object. The columns from left to right show the \mathcal{I}_{-1} , \mathcal{I}_0 , and \mathcal{I}_{+1} data. The blue arrows indicate the blueshift direction in the dispersed orders. Fiducial marks (blue and red vertical lines) indicate $\pm 100 \text{ km s}^{-1}$ shifts relative to the vertical white lines.	44
2.12 Scale $j = 2$ wavelet coefficients of the compact object objects of figure 2.11. See figure 2.11 for further description.....	46
2.13 Rise phase of the blue shifted jet. Profiles are taken along the horizontal white lines in the panels of figure 2.11. From top to bottom the plots show the \mathcal{I}_{-1} , \mathcal{I}_0 , and \mathcal{I}_{+1} profiles. Elapsed times are from the middle of a given exposure to the beginning of the first exposure in the <i>MOSES-06</i> data sequence. Fiducial lines in the images mark the locations of -100 km s^{-1} (blue line) and $+100 \text{ km s}^{-1}$ (red line) doppler shifts relative to the black line. The thick black curve is an approximate background level; see text for details.	50

LIST OF FIGURES – CONTINUED

Figure	Page
2.14 Rise phase of the bi-directional jet. See caption of figure 2.13 and the text for details.	53
2.15 Stack plots of profiles through the compact objects of figure 2.11 with position on the horizontal axes and time on the vertical axes. Fiducial lines in the images mark the locations of -100 km s^{-1} (blue line) and $+100 \text{ km s}^{-1}$ (red line) doppler shifts relative to the white vertical line. The columns from left to right show the \mathcal{I}_{-1} , \mathcal{I}_0 and \mathcal{I}_{+1} profiles. The stack plots show profiles from exposure $n = 2$ to exposure $n = 24$. The remaining exposures are fairly noisy.....	55
2.16 Blue jet doppler shift estimates. See text for details.	57
2.17 Bi-directional jet doppler shift estimates. See text for details.	58
2.18 Magnetic context of the blue jet (top) and bi-directional jet (bottom). Panels from left to right show intensity (log scaled), <i>MDI</i> photospheric line of sight magnetic field strength, and potential field extrapolation up to 5750 km above the photosphere. Jet locations are marked with a red “x”. (Field extrapolation provided by Dr. Dana Longcope)	60
2.19 Plasma β (solid) and the Alfvén speed (dashed) in the transition region.....	62
2.20 <i>MOSES-06</i> \mathcal{I}_0 image with green numbers indicating the locations of the explosive events discussed in section 2.5. The grey numbers indicate point-like emission included with the examples in figure 2.22 to show the instrument point spread functions.	65
2.21 Explosive events identified within the coronal hole.	65
2.22 Examples of explosive events observed by <i>MOSES-06</i> . Shown are the scale $j = 2$ wavelet coefficients of the \mathcal{I}_m . Each panel has three sub-panels. Sub-panels from top to bottom: \mathcal{I}_{+1} , \mathcal{I}_0 and \mathcal{I}_{-1} . Each sub-panel has a 37.5” field of view....	66

LIST OF FIGURES – CONTINUED

Figure	Page
2.23 Explosive event locations (green dots) over-plotted on an <i>MDI</i> magnetogram taken two hours after the <i>MOSES-06</i> flight. Contours show the +5 (white) and -5 (black) gauss contours of a potential field extrapolation up to 5750 km.....	68
2.24 Properties of explosive events observed with <i>MOSES-06</i> . The left table summarizes the event types and locations; the right table summarizes the event magnetic properties. Bi-directional jet* indicates that the event appears strongly bi-directional in one of the \mathcal{I}_{-1} or \mathcal{I}_{+1} but not the other. B values are from the potential field extrapolation. Seven of the 41 explosive events fall outside the field extrapolation field of view so only 34 events are characterized magnetically. See text for further description.....	69
3.1 Synthetic <i>MOSES-06</i> observation of a bi-directional jet. Top row left to right: $m = -1$, $m = 0$, $m = +1$. Bottom row shows the jet spectrum. The blue arrows indicate the blueshift direction in the dispersed channels.....	76
3.2 <i>Top Left:</i> Synthetic \mathcal{I}_0 image. <i>Top Right:</i> \mathcal{I}_0 image reconstructed with MART. The blue contour is the 50% level of the jet intensity above the background. <i>Bottom:</i> Total reconstructed $\nu(x, y, \lambda)$ within the blue contour shown in upper right, over-plotted with the known synthetic jet spectrum.	78
3.3 A slice of the reconstructed radiance through the jet in the dispersion (x) direction.....	79
3.4 The wavelet coefficients of the synthetic \mathcal{I}_m up to scale $j = 3$ over-plotted with contours indicating the 3σ significance level of the coefficients.....	81
3.5 Partial reconstruction of the synthetic jet using $j \leq 2$ (top row) and $j \leq 3$ (bottom row). Columns from left to right show \mathcal{I}_{-1} , \mathcal{I}_0 , and \mathcal{I}_{+1} channels.	84

LIST OF FIGURES – CONTINUED

Figure	Page
3.6 <i>Top row:</i> Profiles through the synthetic jet (black) over-plotted with the residual after subtraction of the partial reconstruction results. The purple residual is from partial reconstruction using the $j = 1$ and $j = 2$ wavelet coefficients; the orange residual uses the wavelet coefficients up to scale $j = 3$. The horizontal black line indicates the true background level. <i>Bottom row:</i> Profiles of the partial reconstruction result using the $j \leq 2$ (purple) and $j \leq 3$ (orange) wavelet coefficients in the reconstruction; the black profiles are the known synthetic profiles.....	85
3.7 An $x - \lambda$ slice of the radiance reconstructed using the methods of section 3.5	86
3.8 Total reconstructed radiance within the blue contour shown in the upper right panel of figure 3.2. The reconstruction uses the methods described in section 3.5. The dotted line plots the known synthetic jet spectrum.....	87
3.9 A $y - \lambda$ slice of the radiance reconstructed using the methods of section 3.5.....	88
3.10 Inverted \mathcal{I}_0 using the methods of section 3.6. The jet area is localized to essentially a single pixel. The \mathcal{I}_0 image is shown in logscale to show faint detail. The 50% intensity contour is shown in blue; only the central pixel in the image lies above this contour.	90
3.11 Inverted line profiles using the methods of section 3.6 calculated both within the 50% level and over the full inversion volume, over-plotted with the known synthetic spectrum.	91
3.12 $x - \lambda$ slice through the jet center of $\nu(x, y, \lambda)$ recovered with the inversion method described in section 3.6.....	92
3.13 $y - \lambda$ slice through the jet center of $\nu(x, y, \lambda)$ recovered with the inversion method described in section 3.6.....	92

LIST OF FIGURES – CONTINUED

Figure	Page
3.14 <i>Top row:</i> Profiles through the synthetic jet (black) plus background over-plotted with the residual after subtraction of the partial reconstruction results (orange) and the inversion results (purple). <i>Bottom row:</i> Profiles through the synthetic jet (black), the partial reconstruction results (orange) and inversion results (purple).....	94
4.1 An example frame from a sequence of <i>MOSES-06</i> images of a bi-directional jet. Left to right: $m = -1$, $m = 0$, $m = +1$. Panels are 64×64 pixels, with angular sampling $0.59'' \text{ pixel}^{-1}$. Dispersion is $29 \text{ km s}^{-1} \text{ pixel}^{-1}$. Blue shift direction is indicated with arrows.....	99
4.2 The wavelet coefficients of the \mathcal{I}_m from exposure $n = 15$. The figure shows coefficients up to scale $j = 3$. The over-plotted contours indicate the coefficients used in the partial reconstruction.....	101
4.3 Partial reconstruction of a bi-directional jet observed with <i>MOSES-06</i> . From top to bottom the rows show the data, the reconstructions, and the residuals after subtracting the reconstructions from the data.....	103
4.4 <i>Left:</i> Intensity image \mathcal{I}_0^ν obtained from inversion of the images in figure 4.1. The intensity image is over-plotted with contours showing the 50% peak intensity (blue), dilation of the 50% contour by one pixel (green), and the one pixel dilated 50% contour of $\nu(x, y, 0)$. <i>Right:</i> Plots of the spatial integral of the inverted ν over the contours shown in the left hand panel. The dotted orange line is the the balance of the total integrated emission after subtraction of the emission within the contours; it is low velocity and distributed faintly.....	105
4.5 <i>Left:</i> Stack plot of the bi-directional jet spectra over-plotted with the centers of the blue and red components determined from gaussian fits. <i>Right:</i> Plots of the blue wing doppler speed (blue curve) and red wing doppler speed (red curve). Elapsed time between exposures is approximately 9 s.....	109

LIST OF FIGURES – CONTINUED

Figure	Page
4.6 Light curves of the jet and low velocity emission components. The total line profile integrated over the whole spatial domain of the inversion is shown by the dotted line.	110
4.7 Time evolution of the spatial centroids of the emission in the blue wing (blue), red wing (red), line core (white) and \mathcal{I}'_0 (green). The plotted numbers 0-6 correspond to exposure numbers $n = 12$ through $n = 18$. The numbers are plotted at the spatial coordinates of the respective centroid at the time of the exposure. Spatial coordinates are given in km with a conversion of about $425 \text{ km pixel}^{-1}$	112
5.1 Schematic of the <i>MOSES</i> spectrograph and coordinate system.....	117
6.1 Test setup for measuring primary mirror radius of curvature.....	123
6.2 Test setup for measuring primary mirror surface figure.	125
6.3 Back plate of the primary mirror mount. The three threaded shafts are the vlier screws that push the primary against the tip/tilt/focus constraints. The grid of threaded holes accepts vlier screws to apply controlled forces to the back of the mirror in an effort to correct the distorted figure.....	126
6.4 Left column: Pre (top) and post (bottom) correction measured primary figure error. Right column: 120 term Zernike polynomial fits, used to obtain a smooth representation of the data. The circular indents are obscuration by the tip/tilt/focus constraint screws. The central diffracting region of the mirror is visible in the measured figure as a 5 nm deep indent relative to the surrounding surface. The white dashed circle is a circular fit to points resulting from an edge finding exercise.	126
6.5 Test setup for measuring secondary wedge angle.....	127
6.6 Measured interferometer reference, stitched together from 6 partial measurements of the beam. Area is $65.3 \text{ mm} \times 53.0 \text{ mm}$. WFE is 10.7 nm RMS and 89.7 nm PV.....	128

LIST OF FIGURES – CONTINUED

Figure	Page
6.7 Measured secondary mirror figure error composed of 7 measurements of overlapping segments of the mirror. Total area is 189.8 mm × 48.8 mm with image pixel resolution 73 μm . An imperfection in the stitching process can be seen around x = 22 mm. Tip and tilt have been subtracted.....	130
7.1 Alignment tool used to reference LOTS axes.....	133
7.2 Filter tube alignment target. The central square is 3.63 mm on a side which corresponds to the width of the converging (square) beam at $x=211.01$ mm (the target x location). The crosshairs are parallel to y and z. The circles have radii of integer multiples of 3 mm, corresponding to about 2.3' of misalignment, or a little under 10% of the field of view in the long y direction.	134
7.3 Test setup for focus. The initial wavefront defocus is precisely zeroed using a high quality flat mirror.	135
7.4 Points show measured Zernike defocus as mirror M2 is translated perpendicular to the optic axis (redirected by M1). Over-plotted red line is a linear fit. Asterisk at x=-15 shows the measured value of the Zernike defocus in the actual spectrograph. This result shows that the optical path length has to be increased by 15 mm. This focus curve is far more sensitive than, e.g. measuring visible light root mean square spot size for focus determination.....	136
7.5 Air force resolution target of the aligned and focused <i>MOSES-15</i> spectrograph. Visible light, $m = 0$ spectral order.	137
7.6 Alignment of translation stage for grating roll measurement.....	138
7.7 The figure shows images of a laser beam after diffraction from the grating in the $m = -1$ and $m = +1$ spectral orders. The camera was mounted to translate parallel to the y axis. The vertical difference in the spot image centroid in the two orders is practically zero, indicating good roll alignment of the primary mirror.....	139

LIST OF FIGURES – CONTINUED

Figure	Page
8.1 Point spread functions in <i>MOSES-06</i> three orders for varying field angle. Viewpoint is facing detectors, sun at your back, with positive z towards the top of the page. Superimposed squares represent 13.5 micron pixels.....	144
8.2 Point spread functions in <i>MOSES-15</i> three orders for varying field angle using the optical design from table 8.2. Viewpoint is facing detectors, sun at your back, with positive z towards the top of the page. Superimposed squares represent 13.5 micron <i>MOSES</i> pixels.	145
8.3 Modeled EUV point spread functions. Top Row: point spread functions from perfect primary mirror. Center Row: point spread functions using measured primary mirror figure (§6.1.2). Bottom Row: point spread functions using corrected primary mirror figure (§6.1.3). Left to right column: $m = -1$, $m = 0$, $m = +1$. All point spread functions are normalized to total of one and displayed on the same scale.....	146
8.4 Top Row from model: Full aperture, full aperture, central obscuration. Bottom Row measured: Full aperture pre flight, full aperture post flight, central obscuration post flight. Left to right column: $m = -1$, $m = 0$, $m = +1$. All point spread functions are normalized to total of one and displayed on the same scale.	147
8.5 Modeled optical distortion in <i>MOSES-06</i> $m = -1$ relative to $m = 0$	148
8.6 Modeled optical distortion in <i>MOSES-06</i> $m = +1$ relative to $m = 0$	148
A.1 A movie of a point-like object observed in the <i>MOSES-06</i> data. The panels from left to right show \mathcal{I}_{-1} , \mathcal{I}_0 , and \mathcal{I}_{+1} . The morphology of the brightening is dominated by the instrument point spread functions.	158

LIST OF FIGURES – CONTINUED

Figure	Page
A.2 A movie of a blue shifted jet observed in the <i>MOSES-06</i> data. The panels from left to right show \mathcal{I}_{-1} , \mathcal{I}_0 , and \mathcal{I}_{+1} . The brightening is point-like but shifted left in \mathcal{I}_{-1} and right in \mathcal{I}_{+1} indicating a blueshift.....	158
A.3 A movie of a bi-directional jet observed in the <i>MOSES-06</i> data. The panels from left to right show \mathcal{I}_{-1} , \mathcal{I}_0 , and \mathcal{I}_{+1} . The brightening has two components in \mathcal{I}_{-1} and \mathcal{I}_{+1} , one shifted right and one shifted left relative to the brightening in \mathcal{I}_0 . The two shifted components indicate a bi-directional jet. A gap between the shifted components shows that very little emission is present from low velocity plasma.....	159
B.1 Frequency response of à trous wavelet filters up to scale $j = 3$, and the low pass filter which gives the smooth residual image. The sum of all filters is equal to one.....	165
C.1 Image produced with the illumination device described in §C.3.1. This image is taken with the $m = -1$ CCD; the other CCD illumination patterns are similar in appearance.....	173
C.2 Photon transfer curve for $m = -1$ CCD. The data is plotted on log-log axes to show the various signal regimes. At low signal, the presence of read noise (magnitude of variance indicated by horizontal red line) results in a deviation of the transfer curve from unity slope (gray curve). At higher signal the read noise becomes insignificant compared to the Poisson distributed shot noise, and the curve takes on a characteristic slope of one, until A/D saturation is reached and the variance drops precipitously, as all pixel values approach $2^{14}-1$ DN (vertical green line). When the read noise variance is subtracted from the total signal variance, the Poisson limited linear curve extends all the way to the zero signal level, indicating good estimation of the read noise variance. For reference the theoretical curve for pure Poisson noise is overplotted as a blue line of slope 1.....	176
C.3 $m=0$ CCD Photon transfer curve. See figure C.2 caption for further details.....	177

LIST OF FIGURES – CONTINUED

Figure	Page
C.4 m=+1 Photon transfer curve. See figure C.2 caption for further details.	178
C.5 Histograms of estimated value of 1/G for the $m = -1$ CCD. The statistics are generated using NxN sub arrays of the noise images. As N is varied, the width of the histogram (which may be taken as an error estimate on the gain) varies, but the centroid remains the same. The symbols represent data, the solid lines are gaussian fits. The gain estimate results from averaging the centroids of the gaussian fits.....	179
C.6 Histograms of estimated value of 1/G for the $m = 0$ CCD. See caption of figure C.5 for further details.	180
C.7 Histograms of estimated value of 1/G for the $m = +1$ CCD. See caption of figure C.5 for further details.	181
C.8 Image produced with EUV illumination of the $m = -1$ CCD; the other CCD illumination patterns are similar in appearance. The contours are smoothed. The underlying grid pattern is produced by the thin metallic filter used to block visible light.	183
C.9 Noise from various sources: Synthetic (upper right), visible light measurement, $m = -1$ CCD (center), and EUV measurement, $m = -1$ CCD (lower left). All noise images are displayed on the same scale.	184
C.10 Power spectral densities of noise from synthetic (left), visible light (center), and EUV (right) data. All panels are displayed with the same scale.	186
C.11 Significance levels as function of wavelet scale for the à trous transform applied to different noise sources. The significance levels are reduced in the EUV data, as the noise is smoothed due to charge diffusion. Note that signal to noise does not increase, as the signal is smoothed accordingly.	189

LIST OF FIGURES – CONTINUED

Figure	Page
D.1 Context image. Full <i>MOSES-06</i> field of view. Over plotted, the red square is shown close up in figure <i>D.2</i> . The green squares indicate the compact sources shown in figure <i>D.7</i>	195
D.2 Close up of the region bounded in red in figure <i>D.1</i> , and its wavelet transform up to scale 4. Original images top row, $m=-1,0,1$ left to right. Wavelet residual (smoothed images \mathcal{I}_s^N) second row. Wavelet scales 4 through 1 are third through last rows. The bright object center left was the subject of a paper by Fox et al. (2010). The shape of the core is dominated by the instrument point spread function, as is the compact source just below center frame.	196
D.3 Reconstruction of a compact source for point spread function estimation, $m=-1$ spectral order. Each row shows an image on left, with the first and second wavelet scales to the right. Top row: original image. Middle Row: Extracted object/point spread function estimate. Bottom Row: Original image minus object.	197
D.4 Reconstruction of a compact source for point spread function estimation, $m=0$ spectral order. Each row shows an image on left, with the first and second wavelet scales to the right. Top row: original image. Middle Row: Extracted object/point spread function estimate. Bottom Row: Original image minus object.	198
D.5 Reconstruction of a compact source for point spread function estimation, $m=+1$ spectral order. Each row shows an image on left, with the first and second wavelet scales to the right. Top row: original image. Middle Row: Extracted object/point spread function estimate. Bottom Row: Original image minus object.	198
D.6 The small active region, \mathcal{I}_0 data scale 1 wavelet coefficients. Each frame is at a different time, covering most of the flight with time increasing from upper left to lower right. Exposures numbers are 1, 2, 4, 6, 10, 14, 18, 23 and 25, of 27 total, going in order from upper left, left to right, top to bottom. UT shown in the titles of the individual panels.	200

LIST OF FIGURES – CONTINUED

Figure	Page
D.7 Panels show the scale $j = 1$ wavelet coefficients of the compact objects from figure D.1. Each panel has three frames that show, from top to bottom, the $m = +1$, $m = 0$, and $m = -1$ data.	201

ABSTRACT

Explosive event is the name given to slit spectrograph observations of high spectroscopic velocities in solar transition region spectral lines. Explosive events show much variety that cannot yet be explained by a single theory. It is commonly believed that explosive events are powered by magnetic reconnection. The evolution of the line core appears to be an important indicator of which particular reconnection process is at work.

The *Multi-Order Solar Extreme Ultraviolet Spectrograph (MOSES)* is a novel slitless spectrograph designed for imaging spectroscopy of solar extreme ultraviolet (EUV) spectral lines. The spectrograph design forgoes a slit and images instead at three spectral orders of a concave grating. The images are formed simultaneously so the resulting spatial and spectral information is co-temporal over the $20' \times 10'$ instrument field of view. This is an advantage over slit spectrographs which build a field of view one narrow slit at a time. The cost of co-temporal imaging spectroscopy with the *MOSES* is increased data complexity relative to slit spectrograph data. The *MOSES* data must undergo tomographic inversion for recovery of line profiles.

I use the unique data from the *MOSES* to study transition region explosive events in the He II 304 Å spectral line. I identify 41 examples of explosive events which include 5 blue shifted jets, 2 red shifted jets, and 10 bi-directional jets. Typical doppler speeds are approximately 100 km s^{-1} . I show the early development of one blue jet and one bi-directional jet and find no acceleration phase at the onset of the event. The bi-directional jets are interesting because they are predicted in models of Petschek reconnection in the transition region.

I develop an inversion algorithm for the *MOSES* data and test it on synthetic observations of a bi-directional jet. The inversion is based on a multiplicative algebraic reconstruction technique (MART). The inversion successfully reproduces synthetic line profiles. I then use the inversion to study the time evolution of a bi-directional jet. The inverted line profiles show fast doppler shifted components and no measurable line core emission. The blue and red wings of the jet show increasing spatial separation with time.

CHAPTER ONE

INTRODUCTION

1.1 The Solar Atmosphere1.1.1 The Photosphere

The photosphere is the visible surface of the sun. Below the photosphere the sun rapidly becomes optically thick. The radiation spectrum of the photosphere is approximately that of a blackbody at 5750 K, punctuated by dark absorption lines caused by cooler atoms and ions overlying the photosphere and absorbing photospheric emission at discrete wavelengths. One of the most prominent features of the photosphere are compact dark regions known as sunspots. Observed since antiquity, Hale (1908) showed that these regions contain strong magnetic fields.

Measurements of plasma velocities in the photosphere show distinct cells where plasma flows upwards in the cell centers, travels horizontally in the cell interiors, then flows downwards in lanes between adjacent cells. These velocity patterns are due to convective motion below the photosphere. This pattern is known as granulation, and the discrete cells are referred to as granules. Granules have typical size scales of 700 - 1400 km and lifetimes of 8 - 20 minutes (Bahng & Schwarzschild, 1961). There are also larger scale convective cells which create a visible pattern in the photosphere known as supergranulation (Leighton et al., 1962). Supergranular cells have length scales of 13,000 - 18,000 km and lifetimes of 1 - 2 days. For a review of supergranulation see Rieutord & Rincon (2010).

1.1.2 The Photospheric Magnetic Field

While the most obvious magnetic features in the solar photosphere are sunspots, the magnetic field is not exclusive to these regions. The *Michelson Doppler Interferometer (MDI)* instrument aboard SoHO measures photospheric line of sight magnetic fields. MDI measurements (figure 2.4) show the photosphere is peppered with small scale concentrations of magnetic field. These small scale fields emerge as ephemeral regions (Harvey & Martin, 1973), or clusters of bipolar concentrations, within the supergranule cells. Convective flows fragment these magnetic concentrations and sweep them to the downflowing supergranular cell boundaries (Roudier et al., 2009). The field in the supergranular lanes forms a clumpy distribution of strong fields known as the magnetic network. The constantly evolving small scale fields in the photosphere suggest a complicated magnetic environment in the atmosphere above. A picture has emerged in which multi-scale magnetic loops, rooted in footpoints in the photosphere, jostle and collide due to turbulent convection. This complicated collection of magnetic structures has been described as the “magnetic junkyard” (Dowdy et al., 1986) or the “magnetic carpet” (Parnell, 2001).

1.1.3 The Chromosphere

Above the photosphere lies the chromosphere. In an average sense the chromosphere is a 2,500 km thick layer over which the temperature first drops to a minimum of 4,000 K before rising again to a maximum of 20,000 K (Vernazza et al., 1981). The density decreases from 10^{17} cm^{-3} to 10^{10} cm^{-3} (Abhyankar, 1977) and the solar spectrum begins to show spectral lines in emission and absorption. Prominent chromospheric spectral lines include H α , Lyman α , Mg II K and Ca II K (Vernazza et al., 1981). The red-hued H α emission may be seen as the colored band at the limb during an eclipse and gives the chromosphere its name.

Images of the chromosphere show many lateral inhomogeneities including spicules (Athay, 1984), filaments (Buehler et al., 2016), and the chromospheric network. The network is a pattern of bright emission seen in many chromospheric spectral lines which overlies the supergranular cell boundaries and is dark in the cell interiors (Bray & Loughhead, 1974; Athay, 1976). The chromospheric network therefore also overlies the photospheric magnetic field which is concentrated in the supergranular lanes. The network indicates that the solar atmosphere is structured and that structure is influenced by magnetic fields rooted in the photosphere.

1.1.4 The Corona

The corona is the outer layer of the solar atmosphere. The temperature ranges from 10^6 K to 10^7 K and the density drops to 10^9 cm^{-3} . The solar spectrum in the corona shows optically thin emission lines formed over this range of temperatures. Exactly how the high temperature of the corona is maintained is one of the enduring mysteries in solar physics (Withbroe & Noyes, 1977). The corona may be observed in visible light during an eclipse; at other times it is too faint to be seen against the glare of the photosphere.

Observational study of the corona was to flourish in the space age. Many emission lines formed at coronal temperatures are in the ultraviolet (UV), extreme ultraviolet (EUV) and soft x-ray (SXR) regions of the electromagnetic spectrum and do not penetrate the Earth's atmosphere. With the advent of space travel it has become possible to observe the sun in this spectral range. Recall that the photospheric spectrum is a relatively cool blackbody spectrum, and therefore does not have significant emission at UV and shorter wavelengths. It is possible to use filters to image the sun in the EUV where the photosphere is dark and thus observe the on disk solar corona. These filtergram images of the corona also show significant

structuring but the network is no longer seen. The preeminent structures in the corona are bright arching loops which have foot points in photospheric magnetic field concentrations.

The brightest coronal emission generally occurs in so called active regions (van Driel-Gesztelyi & Green, 2015) associated with the strongest photospheric magnetic field concentrations. Emission in coronal loops (Rosner et al., 1978) traces closed magnetic field lines which connect opposite polarity photospheric flux concentrations. The darkest coronal features, contiguous regions that appear dark in many coronal lines, are known as coronal holes (Cranmer, 2009). Coronal holes are associated with unipolar magnetic regions with open field lines rooted in the photosphere that connect to opposite polarity sources external to the sun. Open field regions in coronal holes act as conduits for mass loss from the sun carried away by the solar wind (Hassler et al., 1999). Regions of the atmosphere away from active regions and coronal holes and the aforementioned filaments are known as the quiet sun (e.g. Withbroe & Noyes, 1977).

The change from network structures in the chromosphere to loop structures in the corona is the result of a change in the pressure balance between the gas pressure and the magnetic pressure (Gabriel, 1976). The ratio of these pressures is defined as the plasma β :

$$\beta = \frac{8\pi P}{B^2} \quad (1.1)$$

The plasma β varies from $\beta \geq 1$ in the chromosphere and below to $\beta \ll 1$ in the corona (Gary, 2001). In the high β lower atmosphere the gas pressure dominates the magnetic pressure and the magnetic field is concentrated by plasma flows into the supergranular lanes. In the low β corona the magnetic pressure dominates and the magnetic field expands to fill the coronal volume. Furthermore the coronal plasma is a

nearly perfect conductor and thus the plasma is “frozen” into the magnetic field (e.g. Klimchuk, 1992); the plasma may move along but not across the magnetic field lines which may be open (coronal holes) or closed (active regions). Thus in the corona the plasma traces the magnetic field lines and the magnetic field determines the coronal structuring. The intimate connection between the coronal structures and magnetic fields strongly implicates magnetic energy in the coronal heating problem.

1.1.5 The Transition Region

The solar transition region is an interface between the cool solar chromosphere and the million degree solar corona. The transition is most often observed in UV and EUV spectral lines formed between 10^4 K and 10^6 K (Wilhelm et al., 2007). Examples of transition region spectral lines and their temperature of formation include C II 1335 Å (4×10^4 K), Si IV 1403 Å (6.4×10^4 K), He II 304 Å (8×10^4 K), O IV 790 Å (1.9×10^5 K), and O VI 1032 Å (2.8×10^5 K), and Ne VIII 770 Å (6.5×10^5 K) (e.g. Peter, 2001). Transition region spectral lines are formed over narrow temperature ranges and may be isolated spectroscopically, thus these lines provide direct information on the physical state of the plasma at different heights in the transition region (Vernazza & Reeves, 1978).

Measurements at the limb show transition region spectral line emission may be found at heights up to several thousands of kilometers above the (spherically averaged) chromosphere (Brueckner & Nicolas, 1973). Much of this observed thickness however is due to the chromospheric intrusions known as spicules (Brueckner & Nicolas, 1973; Withbroe & Mariska, 1976); the transition from chromospheric to coronal conditions may occur over a distance as small as a few tens of kilometers (Feldman, 1983). Over the temperature range of the transition region the density drops from about $n = 10^{10.7}$ at 10^4 K to $n = 10^{9.3}$ at 3×10^5 K (Brueckner & Nicolas, 1973).

Gabriel (1976) showed that in theory the steep transition region occurs in the throats of magnetic funnels rooted in the chromospheric network and in thermal contact with the corona. These funnels fan out as the plasma β decreases. The model of Gabriel (1976) explains the observed emission measure distribution of the hotter transition region but is unable to explain the low temperature distribution. (Dowdy et al., 1986) proposed that a cool transition region exists and consists of loop structures which do not reach coronal heights and temperatures. Cool loops exist in theory (Klimchuk, 1992) but direct observations are lacking perhaps due to limited spatial resolution (Feldman, 1983, 1987).

Images of the transition region between temperatures of 10^4 K and 3×10^5 K show the same network pattern as seen in the chromosphere albeit somewhat more diffuse than the chromospheric network (Reeves et al., 1974). In the hotter transition region the network disappears and the structuring is more coronal in character (Reeves et al., 1974). Transition region observations also show indications of impulsive energy release from small scale structures such as microflares (Porter et al., 1987), network brightenings (Harra et al., 2000), blinkers (Bewsher et al., 2004), and explosive events (Brueckner & Bartoe, 1983; Dere et al., 1991; Fox et al., 2010; Innes et al., 2015)

The transition region is extremely complex and has been the subject of a large volume of publications (see reviews by Mariska (1986); Innes (2004); Wilhelm et al. (2007)). It may be assumed that transition region dynamics will continue to be of great interest due to their role in the mass and energy balance of the solar atmosphere. It is through this boundary layer (or the associated magnetized plasma structures) that mass and energy must flow to heat the corona and provide mass to the solar wind (Mariska, 1986).

1.2 Transition Region Explosive Events

Many energetic phenomena have been observed in the solar transition region and investigated as sources of solar wind mass and coronal heating (see previous section for references). In this dissertation I will focus on a class of observations known as transition region explosive events. Transition region explosive event is the name given by Dere et al. (1984) to describe slit spectrograph observations of enhanced emission in the far (super-sonic) wings of transition region spectral line profiles. They were first reported by Brueckner & Bartoe (1983) and were characterized as jets and turbulent events depending on whether enhanced emission was present in one or both line wings.

Explosive events have been observed in many transition region spectral lines. These include C II 1334/1336 Å (2×10^4 K), Si IV 1403 Å (8×10^4 K), C IV 1548 Å (1×10^5 K), and N V 1239 Å (2×10^5 K) (Brueckner & Bartoe, 1983) and He II 304 Å (8×10^4 K) (Fox et al., 2010). The Si IV 1393/1402 Å (8×10^4 K) line pair has been a popular choice for explosive events studies (Ning et al., 2004; Innes et al., 1997; Innes, 2001; Innes et al., 2015). The average properties of explosive events observed in C IV from Dere (1994) are summarized in table 1.1. Explosive events have been observed with several instruments including the *High Resolution Telescope and Spectrograph (HRTS)* (Brueckner & Bartoe, 1983; Porter & Dere, 1991), the *Solar Ultraviolet Measurements of Emitted Radiation (SUMER)* (Wilhelm et al., 1995; Innes et al., 1997) instrument aboard SoHO, the *MOSES* (Fox et al., 2010), and the *Interface Region Imaging Spectrograph (IRIS)* (DePontieu et al., 2014; Innes et al., 2015).

Table 1.1: Explosive event properties from Dere (1994). QS stands for quiet sun and CH stands for coronal hole.

Spectroscopic velocities	100 km s^{-1}
Spatial scale	1500 km (2'')
Lifetimes	60 s
QS Birthrate	600 s^{-1}
CH Birthrate	250 s^{-1}
Mass	$6 \times 10^8 \text{ g}$
Kinetic Energy	$6 \times 10^{22} \text{ erg}$

Explosive events are typically located above weak mixed polarity fields along the edges of the quiet sun magnetic network (Porter & Dere, 1991) and are associated with photospheric flux emergence (Dere et al., 1991) and cancellation (Chae et al., 1998). Due to the correlation between explosive event locations and the magnetic network Dere et al. (1991) first suggested that explosive events are driven by magnetic reconnection (Priest & Forbes, 2007) and that the rate of energy release, based on explosive event lifetimes, is consistent with the fast reconnection model of Petschek (1964).

Explosive events sometimes show a spatial offset between red and blue wings (Dere et al., 1989), and between the wings and the core emission (Ning et al., 2004). Innes et al. (1997) reported spatially offset wings which moved outwards from a fixed location over time; they interpreted these results as bi-directional flows resulting from magnetic reconnection in the transition region. Explosive events often show no detectable sky plane motion (Dere et al., 1989).

Many studies have looked at whether energy release in explosive events contributes significant mass and energy to the solar wind and coronal heating, respectively. The energy required to heat the corona is approximately $3 \times 10^5 \text{ ergs cm}^{-2} \text{ s}^{-1}$ (Withbroe & Noyes, 1977). The global energy requirement is therefore $2 \times 10^{28} \text{ ergs s}^{-1}$. Assuming the birthrates and energies associated with

explosive events (table 1.1) it seems unlikely that explosive events contribute significantly to the coronal energy budget. Dere et al. (1989); Teriaca et al. (2004) concluded that explosive events do not contribute significantly to coronal heating. On the other hand it has been argued that explosive events may contribute significantly to the coronal energy budget as part of a range of small scale energetic events, some currently undetectable (Winebarger et al., 2002). It has been estimated that explosive events may contribute significant mass to the solar wind (Brueckner & Bartoe, 1983; Dere et al., 1989).

1.2.1 Explosive Event Magnetic Reconnection Models

Explosive events are interesting in part because they may be observational signatures of magnetic reconnection in the transition region. Magnetic reconnection is a fundamental plasma process in which magnetic energy is converted to plasma kinetic energy. Reconnection is most often associated with energy release in the corona observed as solar flares. Energy release in reconnection events varies by orders of magnitude from 10^{24} ergs in nanoflares (Parker, 1988) to $10^{28}\text{--}10^{32}$ ergs in medium to large size flares (Cargill, 2013). Magnetic reconnection is ubiquitous in the solar atmosphere yet is still poorly understood. This is due in part to low emission measure in the expected (coronal) reconnection sites and the observations are necessarily indirect (Savage et al., 2012). Emission measure in denser transition region plasmas should be two orders of magnitude greater than that in the corona, which suggests that it may be possible to directly observe reconnection sites.

The fast directional and bi-directional flows suggested by spectroscopic measurements of transition region explosive events may be due to plasma which is accelerated as magnetic field lines reconnect and retract to a new lower energy configuration (Innes et al., 1997). The doppler speeds observed in explosive events are reasonable

values for the Alfvén speed in the transition region (Dere et al., 1991). The Alfvén speed is the predicted outflow speed in magnetic reconnection (Priest & Forbes, 2007). If the reconnection scenario is correct then explosive event observations provide powerful diagnostics of the reconnection process itself. Specific reconnection models to date have difficulty explaining all of the observed features of all explosive events.

Innes & Tóth (1999) modeled Petschek reconnection in the context of transition region explosive events. Their results show that at mid transition region temperatures (8×10^4 K to 2×10^5 K) the expected line profiles show almost no emission from low velocity plasma and consist entirely of emission from fast oppositely directed jets. Importantly, there is no line core emission in this model.

On the other hand, line core brightening associated with explosive events has frequently been reported (Dere et al., 1991; Innes, 2001; Innes et al., 1997). Ning et al. (2004) reported a spatial separation between the core and wing emission. Innes et al. (2015) showed examples of line core brightening in explosive events observed in Si IV 1402 Å with *IRIS*. In order to explain the presence of this low velocity emission, Innes et al. (2015) modeled reconnection in a scenario where the tearing mode instability (Priest & Forbes, 2007) results in the creation of magnetic islands. The plasma in these islands is confined and explains the line core emission.

The time evolution of the line profiles from the plasmoid model of Innes et al. (2015) can be described in three separate phases. First an acceleration phase lasting for 60 s shows plasma being accelerated from rest into bi-directional jets at the characteristic Alfvén speed. The next phase lasts approximately 150 s and is similar to the steady state Petschek model of Innes & Tóth (1999): wing emission at the Alfvén speed and no emission from low velocity plasma, i.e., no line core. Core brightening begins after 300 s with core emission dominating the profiles through the end of the simulation (400 s).

It is expected that the detailed reconnection process will vary with different physical conditions. This expectation has been described by a reconnection phase diagram (Ji & Daughton, 2011). If explosive events are due to reconnection in the transition region it may be that the observed variability in the line profiles is due to different kinds of reconnection. Given that explosive events occur rather frequently there exists great potential to study reconnection itself under transition region conditions. The particular reconnection models of Innes & Tóth (1999) and Innes et al. (2015) suggest that the observed strength of emission in the line core is a vital clue to help distinguish which reconnection process is at work.

1.2.2 Observational Challenges

The emission line spectra characteristic of the solar atmosphere contain a wealth of information about the physical conditions of the emitting plasma. In particular, plasma flows and/or turbulence will variably result in line center shifts, wing enhancements, and broadening of spectral line profiles. The measurement of emission as a function of wavelength is called spectroscopy. As described above the solar emission varies in both space and time, as well as wavelength. I'll call this variable emission the solar *spectral radiance*, and denote it as $\nu(x, y, \lambda, t)$. The concern of spectroscopy, then, is the measurement of ν over some wavelength range of interest.

One approach to measuring ν uses filters. Filters reject emission away from some small range of wavelengths and a filtergram thus approximately samples ν at a single wavelength. It is currently not possible, however, to build filters with a passband narrow enough to resolve spectral line profiles in the EUV. Interference methods, such as the Fabry-Perot etalon, use multiple reflections within an optical cavity to sample ν within extremely narrow wavelength bands. Unfortunately this is

not a viable solution at EUV wavelengths, which do not reflect easily off of known materials. After a few reflections all of the photons are gone.

High spectral resolution spectroscopy in the EUV is therefore traditionally done using a slit spectrograph. One such instrument is the *SUMER* (Wilhelm et al., 1995) instrument aboard SoHO. An image of the sun is formed on a narrow slit. A concave diffraction grating then images the slit onto a detector. The grating disperses the light that passes through the slit, and the concave shape forms images of the slit at each wavelength in the instrument passband. Slit spectrographs like *SUMER* have sufficient spectral resolution to measure individual EUV spectral line profiles.

Slit spectrographs trade field of view for spectral resolution. The spectral resolution increases as the slit becomes narrower. The drawback is that only a slice of ν is measured, say $\nu(x_0, y, \lambda)$. In order to build a field of view, the *SUMER* primary mirror can be rotated to move the solar image relative to the slit. The slit then samples different slices of the sun as the primary is rotated. Many samples are made to measure ν over a finite field of view. The process of building an image in this way is known as rastering.

The problem with rastering is that ν varies with time, and it takes time to measure each raster scan. As an example, Innes et al. (1997) used *SUMER* to study explosive events in the Si IV 1393/1402 Å line pair. Each raster scan took 5 s plus readout time. Scans were made at 1.1" sampling rate. Eight scan positions were used to build a field of view of 9" with 1.1" spatial resolution. Building this field of view takes approximately 60 s, perhaps more depending on the image read out time. From table 1.1, this is about the average lifetime of an explosive event. Since the raster scans are not co-temporal, it is not possible to know for sure whether measured changes in ν are due to spatial or temporal variation. This adds much uncertainty to the study of the spatial and temporal evolution of any emitting source. The problem is

particularly acute with highly dynamic sources such as explosive events (Innes, 2004).

Another drawback to slit spectrographs is that one simply cannot predict the locations of explosive events or other interesting dynamical phenomena. Observing dynamical phenomena is then to some degree a matter of luck: the slit must be in the right place at the right time. Furthermore, given the raster times involved in building a field of view, it will be nearly impossible to investigate potential spatio-temporal relationships between explosive events, as well as other dynamical transition region phenomena.

For instance, as described above, explosive events occur preferentially on the edges of the magnetic network and along magnetic neutral lines, and are associated with changes in the photospheric magnetic field. One may speculate then that these events may track the evolution of the small scale magnetic field of the quiet sun. It would be interesting to know if there are any correlations in time between the onset and evolution of events at different spatial locations. Given the relevant length scale of the supergranule cells ($20''$) and explosive event lifetimes, this type of question will be extremely difficult to answer using slit spectrographs.

1.3 The Multi-Order Solar Extreme ultraviolet Spectrograph (MOSES)

1.3.1 Concept: Slitless Spectroscopy

Slitless spectroscopy, as the name implies, is a spectroscopic system without a slit. The goal in removing the slit is to obtain simultaneous (i.e. co-spatial and co-temporal) image and spectral data over a wide field of view. The NRL Extreme Ultraviolet Spectrograph (S082A) (Tousey et al., 1973) flown on Skylab is an example of a slitless spectrograph. This instrument used a concave diffraction grating to form dispersed images of the sun directly on the recording medium (photographic film). The results show overlapping images of the sun, with each image corresponding to a

different spectral line within the instrument passband (170-630 Å). An example of an S082A slitless spectrograph image is shown in figure 1.1.

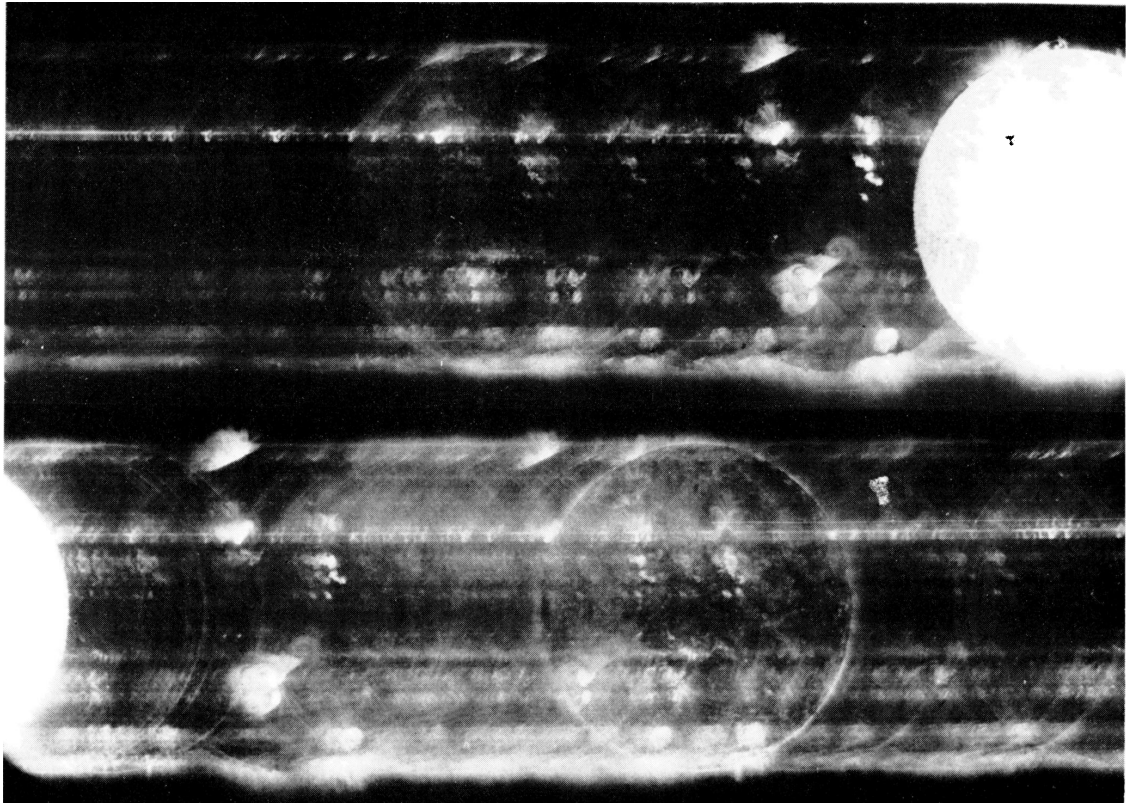


Figure 1.1: S082A slitless spectrograph data in the 200-400 Å spectral range. The bright disk in the upper right hand corner is the transition region He II 304 Å spectral line. Image from (Tousey et al., 1973).

The trade off for wide field of view in the S082A images is a confusion of spatial and spectral content. The images at different wavelengths overlap. This makes it difficult to say for sure what spectral line is responsible for a given image feature. This confusion persists even in cases where a single spectral line dominates the image, e.g., the He II 304 Å line in the upper right of figure 1.1. It is not possible to say whether a given intensity distribution in the He II 304 Å image is due to spatial structure or

spectral structure (e.g., doppler shifts, which would shift or elongate the distribution in the dispersion direction).

The *Multi-Order Solar EUV Spectrograph (MOSES)* (Kankelborg & Thomas, 2001) is designed to address some of these ambiguities. *MOSES* is a slitless spectrograph: images are formed directly with a concave diffraction grating. Key to resolving the spatial/spectral ambiguity described above is that *MOSES* forms images in three diffraction orders, specifically $m = -1$, $m = 0$ and $m = 1$. The $m = 0$ order is not dispersed, and unambiguously shows the location of emission. The $m = -1$ and $m = +1$ dispersed orders are comparable to the S082A images in that overlapping images are formed at all wavelengths in the *MOSES* passband. All images are recorded with charge coupled devices (CCDs).

Ambiguity in *MOSES* data is further reduced by limiting the passband of the instrument. The *MOSES* employs narrowband multilayer filters to restrict the passband to, ideally, a single spectral line. The $m = 0$ image is then a narrowband filtergram. In the ideal case, then, all disparities between the dispersed images and the $m = 0$ filtergram are attributable to doppler shifts of the spectral line under study. In the following section I'll describe the mathematical problem posed by the *MOSES*.

1.3.2 Image Model

The line of sight integrated solar spectral radiance is denoted by $\nu(x, y, \lambda)$ [$\text{erg s}^{-1} \text{cm}^{-2} \text{ster}^{-1} \text{nm}^{-1}$]. The distribution of intensity in the m th order *MOSES* image is modeled as

$$\mathcal{I}_m(x, y) \propto \{\mathcal{P}_m * \mathcal{I}_m^0\}(x, y) + n(x, y) \quad (1.2)$$

where $\mathcal{P}_m(x, y)$ is the point spread function corresponding to \mathcal{I}_m , $n(x, y)$ is additive noise, and $*$ denotes convolution. The instrument noise is discussed in detail in appendix C. \mathcal{I}_m^0 is the ideal geometrical optics image and is given by Kankelborg & Thomas (2001); Fox (2011) as

$$\mathcal{I}_m^0(x, y) \propto \int B(\lambda) \nu(x - m\lambda, y, \lambda) d\lambda \quad (1.3)$$

All coordinates are in image pixels and the spatial coordinates (x, y) are referenced to the center of the m th CCD. The wavelength λ is referenced to the rest wavelength λ_0 of the spectral line under study, and is converted to pixel dimensions using the grating dispersion. Equation 1.3 assumes that the \mathcal{I}_m are co-aligned so that emission at λ_0 images to the same detector coordinates in each spectral order. This co-alignment is described further in section 2.2.1. Equation 1.3 follows directly from the small angle diffraction equation with dispersion along the x direction. $B(\lambda)$ is the spectral passband of the instrument, and ideally isolates a single spectral line for study. The passband is discussed further in section 1.3.4.

Equation 1.3 says that for an ideal instrument, the data are measured projections of the solar spectral irradiance $\nu(x, y, \lambda)$ within the instrument passband. The object is to estimate ν from \mathcal{I}_m . In the units given above, the projection angles correspond to -45 , 0 and $+45$ degrees for $m = -1$, $m = 0$, and $m = +1$ respectively.

Spectral measurements are made by comparing the intensity distribution amongst the orders. Recovery of spectral line profiles from the *MOSES* data can be described mathematically as a three projection tomography problem. The process of producing line profiles from the observations will be referred to as inversion. Inversion from three projections is an ill posed inverse problem. The inversion is not unique; many different solutions exist which can reasonably fit the data. Inversion of *MOSES*

data is the subject of chapter 3.

In the special case of a compact (e.g., small compared to the size of \mathcal{P}_m), isolated object ν , equations 1.2–1.3 reduce to the result expected from a slit spectrograph, i.e., the line profile of the object convolved with the instrument point spread function. If the \mathcal{P}_m are sufficiently narrow compared to the width of the line profile then the *MOSES* directly measures line profiles of compact objects. This property along with high cadence and wide field of view make the *MOSES* an excellent choice for the study of explosive events because the typical size of an explosive event is small and the line profiles are broad (see table 1.1 and chapter 2).

1.3.3 Flight History

The *MOSES* spectrograph is designed to operate at EUV wavelengths that do not penetrate the atmosphere; observations must therefore be made from space. *MOSES* has flown twice at White Sands Missile Range aboard suborbital Terrier boosted Black Brant sounding rockets. The sounding rocket program is an invaluable proving ground for novel instrumentation such as the *MOSES*. The first flight on 8 February 2006 (Fox et al., 2010; Fox, 2011) was designed to observe the lower transition region He II 304 Å spectral line which forms at about 80,000 K. The second flight on 27 August 2015 was optimized for the upper transition region Ne VII 465 Å spectral line which forms at about 500,000 K. When referencing a specific flight I will refer to *MOSES-06* or *MOSES-15*. I will refer to *MOSES* when the distinction is unimportant.

1.3.4 Spectral Passband

$B(\lambda)$, introduced in equation 1.3, is the instrument spectral passband – the relative efficiency of the spectrograph at wavelength λ . By manipulating the shape of B we can select specific wavelength ranges over which $\nu(x, y, \lambda)$ contributes to the

\mathcal{I}_m . The transition region spectral irradiance consists of a forest of emission lines formed by different ionic species under widely varying physical conditions. We can greatly simplify the analysis of slitless spectrograph data by restricting the range over which $B(\lambda)$ differs appreciably from zero. Ideally, $B(\lambda)$ is tuned to isolate an individual spectral line. Kankelborg & Thomas (2001) described such an ideal system and found that a three projection slitless spectrograph is sensitive to the first three moments of the spectral line profile, corresponding to total intensity, mean doppler shift, and doppler broadening. The solar data analysis in this dissertation concerns only the data from *MOSES-06*. Therefore I will describe the *MOSES-06* passband in further detail.

Owens et al. (2005) estimated the total reflectivity of the *MOSES-06* optics which accounts for multilayer reflectivity of the primary and secondary mirrors and grating efficiency. Their measurements show the reflectivity to be a sharply peaked function of wavelength, with maximum reflectivity occurring at approximately $\lambda=307\text{\AA}$ and a full width half maximum reflectivity of 20 \AA . Brosius et al. (1998) used data from the *Solar EUV Rocket Telescope and Spectrograph (SERTS)* instrument to estimate calibrated quiet and active sun EUV spectral line profiles. In the quiet sun the only spectral line in the *MOSES-06* passband is the He II line at 303.8 \AA . In the active sun several other lines appear in the neighborhood of He II; table 1.2 summarizes these lines and their relative intensities.

Table 1.2: Calibrated active region line list within *MOSES-06* full width half maximum passband, from Brosius et al. (1998). Intensity shown relative to the He II 304 Åline intensity.

Ion	Wavelength [Å]	Relative Intensity [%]
Si IX + Fe VI	296.1	0.49
Si XI	303.3	9.33
He II	303.8	100.0
Mn XIV (+ Fe XV)	304.9	0.60
Fe XI + Fe VI	308.5	0.33
Fe XIII	312.2	0.47
Mg VIII	315.0	0.40
Mg VIII	317.0	0.17

In both quiet and active sun, the He II 303.8 Åline dominates the instrument passband.

1.4 Summary of Dissertation Chapters

In this dissertation I have two primary goals:

1. To contribute to our understanding of transition region explosive events, using the *MOSES-06* observations of the He II 304 Å spectral line.
2. To contribute to the advancement of simultaneous imaging spectroscopic techniques through improvements made to *MOSES* inversions and to the instrument itself.

Therefore I present the following. In chapter 2 I present *MOSES-06* observations of transition region explosive events. I use a qualitative description in this chapter. The main conclusions are: that He II 304 Å explosive events, though not to our knowledge reported in the literature prior to *MOSES-06*, are not uncommon and their spectral signatures typically exhibit a distinct lack of emission from low velocity

plasma. This last observation has direct bearing on models of reconnection and plasma flows and is discussed in this chapter.

In chapter 3 I delve into proper tomographic inversions of *MOSES* data. Relevant to this chapter are instrumental considerations described in appendices *C* and *D*. Although explosive events represent perhaps the simplest possible object for inversion, this process is not trivial. Building on past inversion efforts, I use algebraic reconstruction to solve the tomography problem. In this chapter I develop the inversion method using synthetic data. I show how inversion artifacts arise and how they are mitigated.

In chapter 4 I apply the inversion method developed in chapter 3 to the *MOSES-06* data. I show that the line profiles of an example explosive event have no discernible core emission and are consistent with the predictions of the Petschek reconnection model of (Dere et al., 1991). The time evolution of the event shows no indication of increasing emission from low velocity plasma over the times analyzed. The blue and red wings of the jet line profile are spatially separate and move apart with time. This is expected in a scenario where the plasma traces reconnecting field lines.

I devote the remaining chapters to optical integration and testing in support of the *MOSES-15*. In chapter 6 I describe the instrument optical design and testing of the components. In chapter 7 I describe alignment and focus of the spectrograph including improvements made to the spectrograph focus procedure. Finally, in chapter 8 I present optical modeling work done in support of the optical integration and testing.

CHAPTER TWO

QUIET SUN EXPLOSIVE EVENTS OBSERVED IN HE II 304 Å WITH
MOSES-06

In this chapter I will describe the *MOSES-06* observations in detail. The instrument concept has been described in section 1.3. The *MOSES-06* instrument is a three order slitless spectrograph. The measurements comprise a narrowband filtergram and two dispersed images which contain a mix of spatial and spectral information. The equation which describes the *MOSES-06* image formation process is given in equation 1.2. The *MOSES-06* is designed to make measurements of solar He II 304 Å spectral line profiles. The instrument passband is discussed in section 1.3.4.

The He II 304 Å emission line ($\lambda = 303.78 \text{ \AA}$) is the Lyman α transition of singly ionized helium. The formation temperature of the line is approximately 50,000 K (Arnaud & Rothenflug, 1985) which places the emission in the lower transition region. The thermal speed $v_T = \sqrt{k_B T / m_{He}}$ at this temperature is approximately 10 km s^{-1} . Andretta et al. (2000) reported that the average He II 304 Å spectral line profile was very nearly gaussian in both the quiet and active sun. The 304 Å line is one of the brightest of the transition region EUV lines (see figure 1.1). The 304 Å line has an anomalous intensity with enhancement of up to an order of magnitude relative to model predictions which reproduce the intensities of other transition region lines (Jordan, 1975; MacPherson & Jordan, 1999).

Transition region explosive events have been described in section 1.2. In slit spectrograph observations they are characterized by strong doppler shifts of small spatial extent seen in transition region spectral lines. In order to obtain line profiles

from the *MOSES-06* measurements it is generally necessary to invert equations 1.2 and 1.3. This inversion is the subject of chapter 3. Explosive events are a special case because they are *compact* objects, i.e., they have small spatial extent. As discussed in section 1.3.2 the effect of limited spatial extent of the emission is similar to the effect of limited field of view imposed by a spectrograph slit: The dispersed images of emission from a compact object are proportional to the average line profile of the emission.

Compact objects are also most likely to suffer from resolution effects. In particular any compact object smaller than the image point spread function will take on the shape of the point spread function. In appendix *D* I present evidence for many sub-resolution compact objects in the *MOSES-06* data, and derive estimates for the instrument point spread functions which differ in each spectral order. The point spread functions have a significant impact on the appearance of the data at small resolution scales. In order to properly interpret the *MOSES-06* data at small scales the point spread functions must be taken into account.

I begin by in section 2.1 describing the *MOSES-06* dataset along with coronal and magnetic context data from SoHO. I will then examine difference images (section 2.3) to locate spectrally interesting features in the data. Of particular interest are significant differences between the dispersed and filtergram images within compact regions. I will show that at least some of these difference signatures are due to doppler shifted emission whose properties are consistent with the explosive event properties described in section 1.2. Many strong difference signatures are due to differing point spread functions in the different spectral orders.

In section 2.4 two explosive event observations are presented in detail. The filtergram images of these events show a compact object brighten with respect to the surrounding emission. The *MOSES-06* dispersed images reveal the spectral character

of these events. One event is strongly blue shifted. The other has two components, one strongly red shifted and one strongly blue shifted. These events are identified as a blue shifted jet, and a bi-directional jet, respectively. The shift magnitudes are approximately 100 km s^{-1} , consistent with other reported explosive event velocities. Both events appear to have little or no emission at small doppler shifts. Both events exhibit a “switch on” characteristic with no acceleration phase during the event onset despite a 10 s cadence. I will describe the magnetic context of these example events and derive estimates for mass and energy.

In section 2.5 I will show additional examples of explosive events in the *MOSES-06* data. Explosive events do not appear to be rare in He II 304 Å.

2.1 Data

MOSES-06 took flight on 2006 February 8 at 18:44:01 UT aboard a Terrier boosted Black Brant sounding rocket from White Sands Missile Range in New Mexico, USA. The optical characteristics of the *MOSES-06* instrument are shown in table 2.1. In all *MOSES-06* spent approximately 5 minutes above 160 km and recorded 27 data exposures between 18:44:17 and 18:49:13 UT. Each exposure consists of the three images \mathcal{I}_{-1}^n , \mathcal{I}_0^n , and \mathcal{I}_{+1}^n , where the superscript n indicates the exposure number. The images are 2048×1024 pixels with angular sampling rate of $0.59''/\text{pixel}$. Dark exposures were recorded during flight before and after the data sequence to measure the detector pedestal. The raw images are pedestal subtracted and then corrected for flat field variation. The flat fields were measured by Fox (2011).

Table 2.1: Spectrograph specifications for the *MOSES-06* flight.

Focal length	4.74 m
Aperture	8 cm square (f/59)
Detectors	Rear Illuminated CCD
Sampling	2048 × 1024 pixels, 13.5 μm pitch
Pixel subtent	0.59'', 29 mÅ, 29 km s ⁻¹ , 440 km
FOV	20'x10'
Grating	9.48 m sphere, 950 lines/mm
Coatings	B ₄ C/Mg ₂ Si multilayer
Bandpass	20 Å FWHM centered at 307 Å
Target Line	He II 303.8 Å

The times, exposure lengths, and altitudes of the data are shown in table 2.2. The exposure times are from Hans Courrier’s analysis of strip chart records from the flight. The heights are from radar data taken at the range. Both are reproduced from Fox (2011). Exposure times vary between 0.25 s and 24 s with approximately 6 s readout time in between. The long exposures are saturated in the brightest regions. The shortest exposures are somewhat underexposed. 15 exposures taken mid flight between 18:47:15 UT and 18:49:24.75 at nearly uniform 9 s cadence (exposure + readout) are almost perfectly exposed.

Co-observations made by the instrument suite aboard the Solar and Heliospheric Observatory (SoHO) provide context for the *MOSES-06* observations. The *Extreme ultraviolet Imaging Telescope (EIT)* (Delaboudinière et al., 1995) is a normal incidence multilayer EUV filtergraph. *EIT* measures full disk images in He II 304 Å, Fe IX-X 171 Å, Fe XII 195 Å, and Fe XV 284 Å. The temperatures of formation of these lines are 8.0×10^4 K, 1.3×10^6 K, 1.6×10^6 K, 2.0×10^6 K, respectively.

The *Michelson Doppler Imager (MDI)* (Scherrer et al., 1995) aboard SoHO measures line of sight photospheric magnetograms. I will discuss the magnetic context of the *MOSES-06* observations with respect to an *MDI* magnetogram taken on 2006

February 8 at 20:48:27 UT, two hours after the *MOSES-06* flight.

Table 2.2: Catalog of *MOSES-06* data exposures from Hans Courrier and Roger J. Thomas analysis of strip chart records made during the flight. Table adapted from Fox (2011).

Exposure # (n)	Start [UT]	End [UT]	Duration [s]	Altitude [km]
0	18:45:54.00	18:45:54.25	0.25000	161.80 - 162.14
1	18:46:00.30	18:46:01.05	0.75000	170.32 - 171.30
2	18:46:07.00	18:46:08.50	1.50000	178.84 - 180.69
3	18:46:14.55	18:46:20.55	6.00000	187.87 - 194.73
4	18:46:26.70	18:46:38.70	12.00000	201.46 - 213.49
5	18:46:44.95	18:47:08.99	24.0396	219.19 - 237.97
6	18:47:15.15	18:47:18.22	3.06981	241.99 - 243.84
7	18:47:24.40	18:47:27.48	3.07972	247.26 - 248.85
8	18:47:33.65	18:47:36.75	3.09981	251.76 - 253.11
9	18:47:42.95	18:47:46.03	3.07982	255.53 - 256.61
10	18:47:52.20	18:47:55.27	3.06970	258.52 - 259.34
11	18:48:01.45	18:48:04.45	3.00000	260.71 - 261.26
12	18:48:10.70	18:48:13.77	3.06974	262.14 - 262.44
13	18:48:19.95	18:48:23.04	3.08979	262.79 - 262.84
14	18:48:29.20	18:48:32.28	3.07981	262.67 - 262.46
15	18:48:38.60	18:48:41.60	3.00000	261.76 - 261.30
16	18:48:47.85	18:48:50.85	3.00000	260.07 - 259.35
17	18:48:57.05	18:49:00.14	3.08983	257.65 - 256.66
18	18:49:06.30	18:49:09.36	3.05984	254.42 - 253.18
19	18:49:15.50	18:49:18.58	3.07980	250.44 - 248.94
20	18:49:24.75	18:49:27.84	3.08983	245.70 - 243.94
21	18:49:34.10	18:49:58.19	24.0897	240.06 - 221.94
22	18:50:04.35	18:50:16.35	12.0000	216.50 - 204.83
23	18:50:22.65	18:50:28.65	6.00000	198.06 - 191.37
24	18:50:35.00	18:50:36.56	1.55980	183.99 - 182.11
25	18:50:42.75	18:50:43.50	0.75000	174.35 - 173.39
26	18:50:49.70	18:50:49.95	0.25000	165.34 - 165.01

2.2 Data Reduction

The dark subtracted, flat field corrected data must be aligned and normalized prior to quantitative analysis. These data reduction steps are briefly described in this section.

2.2.1 Co-alignment

2.2.1.1 \mathcal{I}_{-1} and \mathcal{I}_{+1} to \mathcal{I}_0 The extent to which equation 1.3 holds true is sensitive to the spatial co-alignment between the measured \mathcal{I}_m . Given the instrument

dispersion ($29 \text{ km s}^{-1} \text{ pixel}^{-1}$) it is desirable to achieve sub pixel co-alignment. I have used the alignment method described in Fox et al. (2010). In this method it is assumed that the mapping of coordinates from \mathcal{I}_{-1} to \mathcal{I}_0 and \mathcal{I}_{+1} to \mathcal{I}_0 is described by a linear polynomial transformation. The polynomial coefficients are optimized with respect to the reduced χ^2 statistic. Fox et al. (2010) reports co-alignment repeatability from exposure to exposure of <0.2 pixel rms. This co-alignment assumes that there is zero net doppler shift averaged over the field of view.

2.2.1.2 \mathcal{I}_0 to SOHO-*EIT* 304 Å Solar coordinates are obtained from co-alignment of the \mathcal{I}_0 with a SoHO-*EIT* 304 Å image via cross correlation. The *EIT* image was taken at 18:39:34 UT, about 9 minutes prior to the mid-point of the *MOSES-06* flight. The *MOSES-06* images are oriented with solar north up and solar west to the right. The instrument field of view is approximately [1004"E, 197"W] by [302"S, 299"N] heliocentric cartesian coordinates. The dispersion direction is E-W. Emission to the blue of He II 304 Å line center shifts west in \mathcal{I}_{+1} and east in \mathcal{I}_{-1} relative to \mathcal{I}_0 ; emission to the red of He II 304 Å is shifted in the opposite sense.

2.2.2 Normalization

I have chosen to work primarily in data units. *MOSES-06* three channels are normalized for source intensity to account for atmospheric extinction and channel sensitivity.

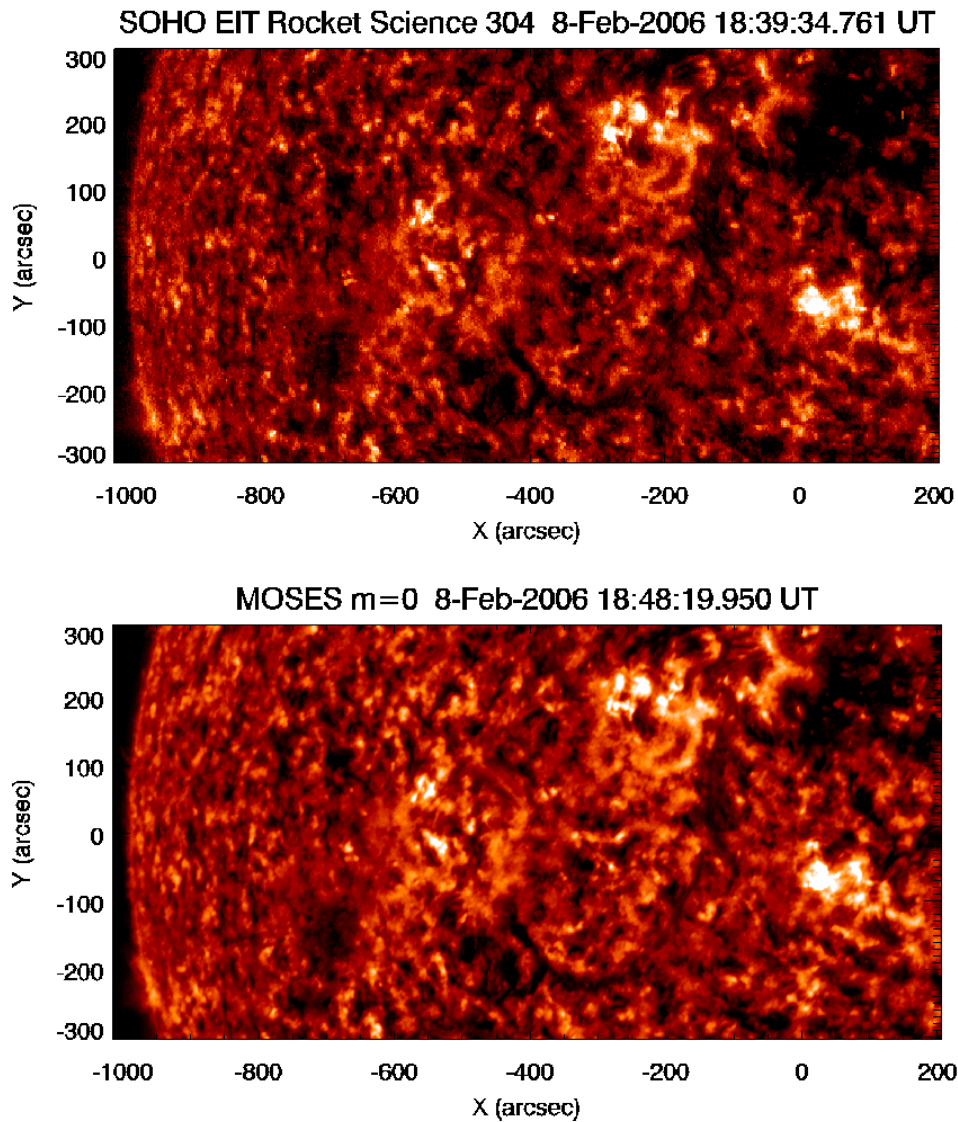


Figure 2.1: *Upper panel:* EIT 304 Å image cropped to the MOSES-06 field of view. *Lower panel:* \mathcal{I}_0 , exposure number $n = 13$, following data reduction and co-alignment. Both images have been logarithmically scaled after clipping the brightest and darkest 0.3% of all pixels.

Figure 2.1 shows an example exposure of the prepared \mathcal{I}_0 next to a near co-temporal *EIT* 304 Å image cropped to the *MOSES-06* field of view. North is up, west is right. The spectrograph dispersion is parallel to the E-W axis. The \mathcal{I}_0 image appears to be a high quality filtergram with very good contrast and resolution. Solar activity was very low on this date and the mottled emission of the quiet sun network dominates over most of the field of view. The primary exception a coronal hole in the upper NW corner, between approximately [0°, 200°]W and [100°, 300°]N. A dark filament channel runs in a backwards "j" shape starting at [100°E, 200°N], reaching a low point at [300°E, 200°S], then curling upwards to terminate at about [450°E, 100°S]. No active regions were present on this date. Three regions, centered on coordinates [550°E, 0°N], [250°E, 200°N], and [50°W, 75°S] show enhanced emission relative to the surrounding network. Figure 2.2 shows \mathcal{I}_{-1} and \mathcal{I}_{+1} . At a glance they appear very similar to \mathcal{I}_0 . In section 2.3 I will examine differences between the \mathcal{I}_m in detail.

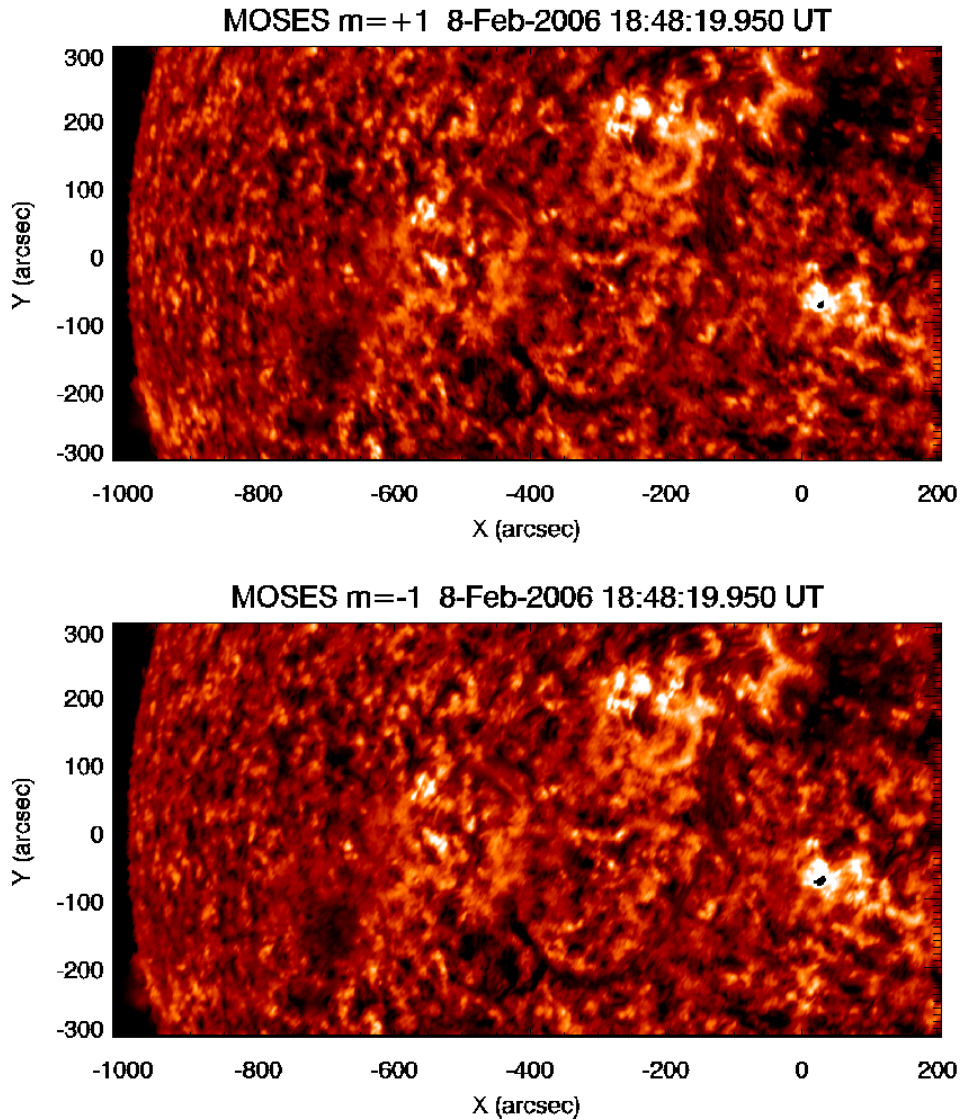


Figure 2.2: *Upper panel:* \mathcal{I}_{+1} , and *Lower panel:* \mathcal{I}_{-1} , exposure number $n = 13$, following data reduction and co-alignment. The images are logarithmically scaled with the same clipping used for the \mathcal{I}_0 image in figure 2.1. Again, north is up, west is right, and the spectrograph dispersion is along the E-W axis. The black pixels located in the center of the bright region at about [20°W, 75°S] are saturated.

Figure 2.3 shows the corona viewed in *EIT* 171 and *EIT* 284. A coronal hole is particularly visible in the 284 Å channel. The strongest network regions in the *MOSES-06* data lie below bright loop structures visible at these coronal temperatures. Both channels show brightening above the limb.

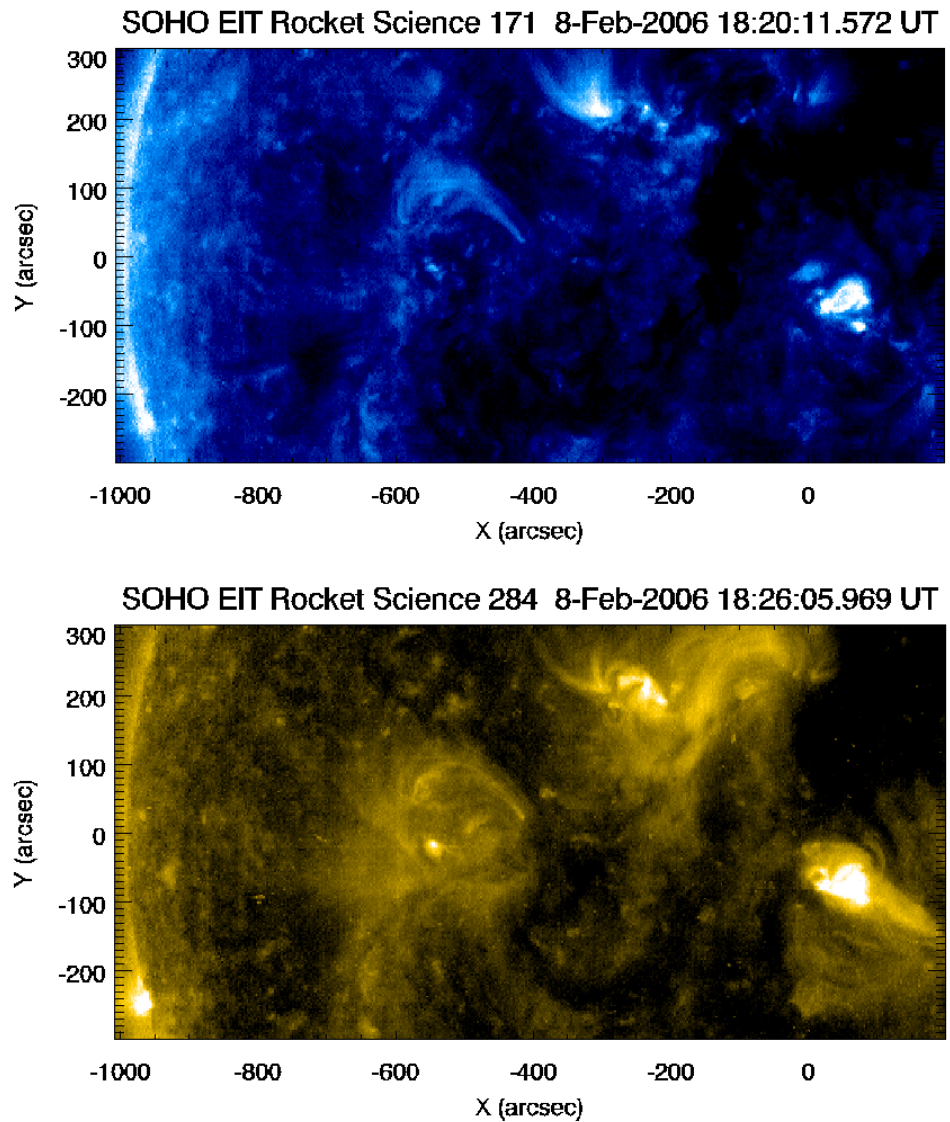


Figure 2.3: *Upper panel:* EIT 171 Å, and *Lower panel:* EIT 284 Å, cropped to MOSES-06 field of view. Images are logarithmically scaled with 0.3% clipping.

Finally, figure 2.4 shows the line of sight photospheric magnetic field measured with *MDI*. This magnetogram was made on 8 February 2006 at 20:48:27 UT, two hours after the *MOSES-06* flight. In order to facilitate visual comparison with the *MOSES-06* measurements I derotated the magnetogram by two hours using the *drot_map()* function, written in the Interactive Data Language (IDL) and part of the SolarSoft software suite (Freeland & Handy, 1998). The time shown in the figure is the derotated time.

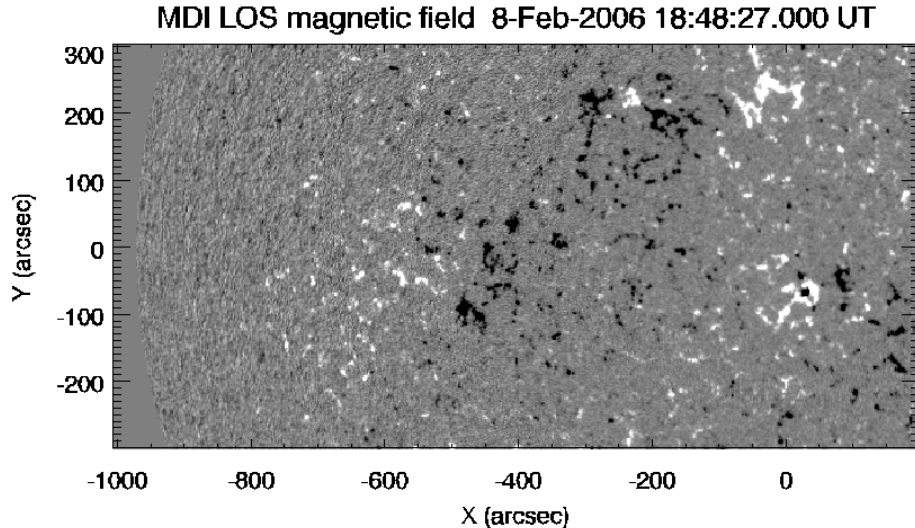


Figure 2.4: Line of sight magnetic field measured by MDI. The display is linearly scaled and clipped at about ± 80 gauss. Positive polarity magnetic elements are white and negative polarity elements are black. Grey regions are regions with weak or no magnetic field. The data have been differentially rotated backwards by two hours; see text.

The bright concentrations in the magnetogram constitute the magnetic network – field that has been concentrated by convective motions into the downflow lanes bordering supergranular cells. The strongest magnetic regions underlie the brightest emission in the *MOSES-06* data (figures 2.1 and 2.2), as well as the (magnetic) loops

visible in the coronal data (figure 2.3). Away from the stronger concentrations the mixed grayscale shows weak, mixed polarity fields.

2.3 Difference Images

The search for interesting phenomena in the *MOSES-06* data set begins with the difference images $d_{(0,-1)} = \mathcal{I}_0 - \mathcal{I}_{-1}$ and $d_{(0,+1)} = \mathcal{I}_0 - \mathcal{I}_{+1}$. Examples of difference images are shown in figure 2.5.

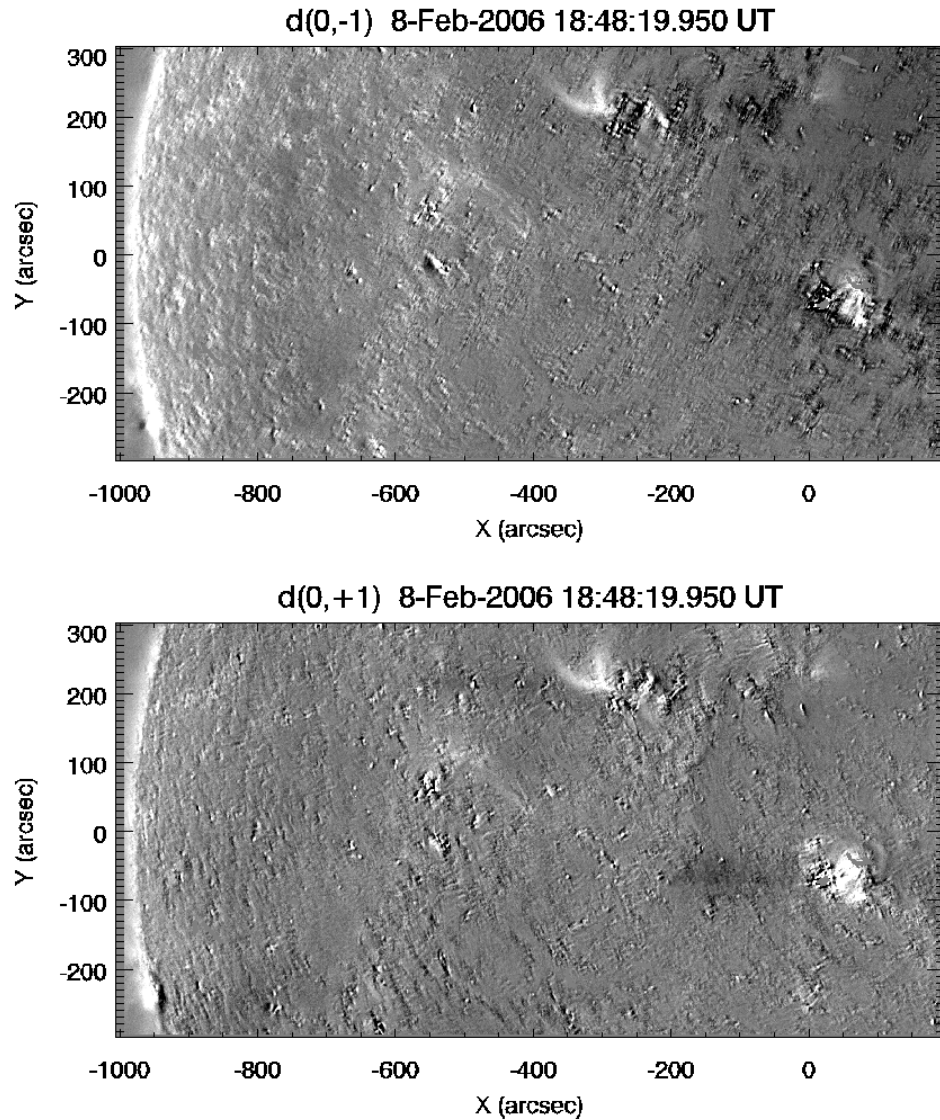


Figure 2.5: Example difference images $d_{(0,-1)} = \mathcal{I}_0 - \mathcal{I}_{-1}$ (top) and $d_{(0,+1)} = \mathcal{I}_0 - \mathcal{I}_{+1}$ (bottom). Light colors indicate positive differences, dark colors indicate negative differences. The images are displayed on a linear scale and have been clipped at three standard deviations to show faint details.

The structure in the difference images is striking. Perhaps the most obvious features have coronal morphology: the limb, and the loops seen near [350°E,225°N] (the “wishbone”) and [50°W,75°S] in the coronal images show strong positive differences. Close inspection shows the loop system near [550°E,0°N] is positive as well. Positive differences mean that e.g., $\mathcal{I}_0 > \mathcal{I}_{-1}$. The most obvious explanation for a positive difference is dispersion of emission at wavelengths different than He II 304 Å. The coronal morphology of these features suggests that this is contaminant emission due to ions at coronal temperatures, not singly ionized helium.

In order to explore the various features in the difference images more deeply I employ a wavelet transform. In general terms wavelet transforms may be used to view images in a range of *resolution scales*. The wavelet transform is defined and described in appendix *B*. Figure 2.6 shows large scale ($j = 6$) wavelet coefficients of $d_{(0,+1)}$. Overplotted arrows show the expected shifts from emission at Si IX/Fe VI 296 Å (blue) and Mg VIII 315 Å (red) (contaminant lines in *MOSES-06* passband; see table 1.2). Notice the distinct depressions near the arrow tips: these depressions are the locations where the emission has been shifted to in \mathcal{I}_{+1} . The blue line shows up at the limb, and the red line in the strong network regions. These depressions are visible in $d_{(0,+1)}$, but appear much more clearly in the scale 6 wavelet coefficients. It is possible that a number of contaminant lines contribute to these coronal features which are too faint to identify.

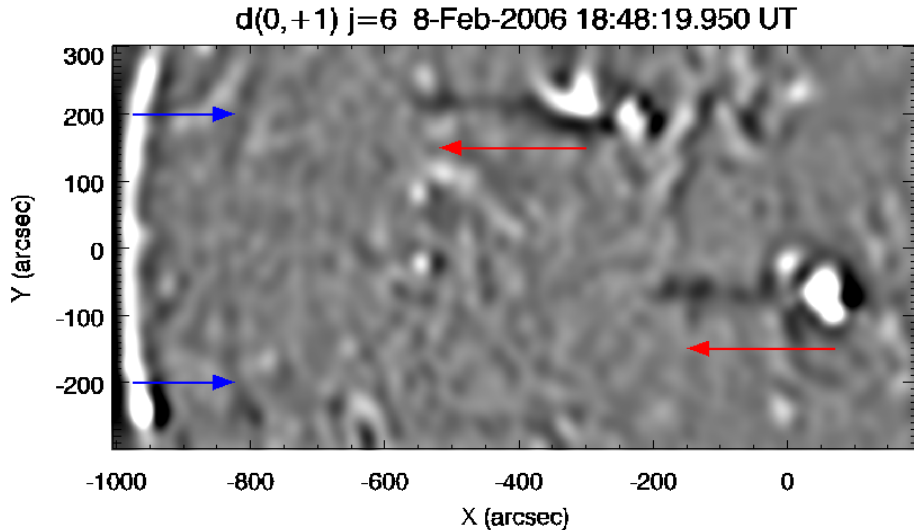


Figure 2.6: Scale $j = 6$ wavelet coefficients of $d_{(0,+1)}$. Overplotted arrows show the expected shifts from emission at Si IX/Fe VI 296.1 Å (blue) and Mg VIII 315.0 Å (red).

A second class of objects in the difference images are strong, compact, and *isolated* positive features scattered across the field of view. For example, three such objects form a bright triangle in the coronal hole region of $d_{(0,-1)}$. Comparison with $d_{(0,+1)}$ shows corresponding features for two of the three; the SE object shows significantly less contrast in $d_{(0,+1)}$. Another example, strongly positive in both difference images, sits about 50" east of the eastern tip of the “wishbone”.

Figures 2.7, 2.8, and 2.9 show the small scale structure of both intensity and difference images within three fields of view covering the coronal hole, a region of quiet sun, and strong network, respectively. Clockwise from upper left figures 2.7, 2.8, and 2.9 show (log scaled) \mathcal{I}_0 , $d_{0,1}$, $\tilde{\mathcal{I}}_0^2$, and $\tilde{d}_{0,-1}^2$, where \tilde{f}^j is the wavelet transform of f at scale j (see appendix B). The wavelet coefficients at the finest scale, $j = 1$, are very noisy, hence the choice of $j = 2$ to show small scale variation.

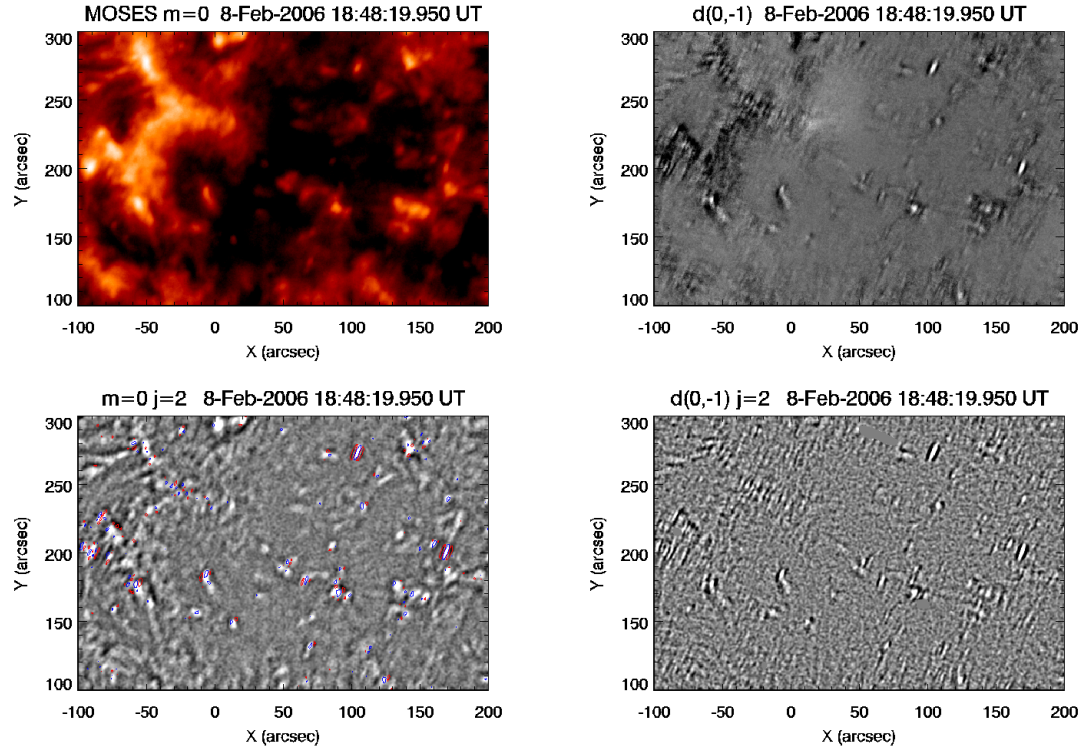


Figure 2.7: Close up of the coronal hole in the *MOSES-06* data showing the small scale structure of the region. Clockwise from upper left: log scaled I_0 intensity, difference image $d_{(0,-1)}$, the scale $j = 2$ wavelet coefficients $\tilde{d}_{(0,-1)}^2$, and the $j = 2$ wavelet coefficients \tilde{I}_z^2 . The 3σ contours of $\tilde{d}_{(0,-1)}^2$ are over-plotted onto the \tilde{I}_z^2 image. Blue contours are positive differences and red contours are negative.

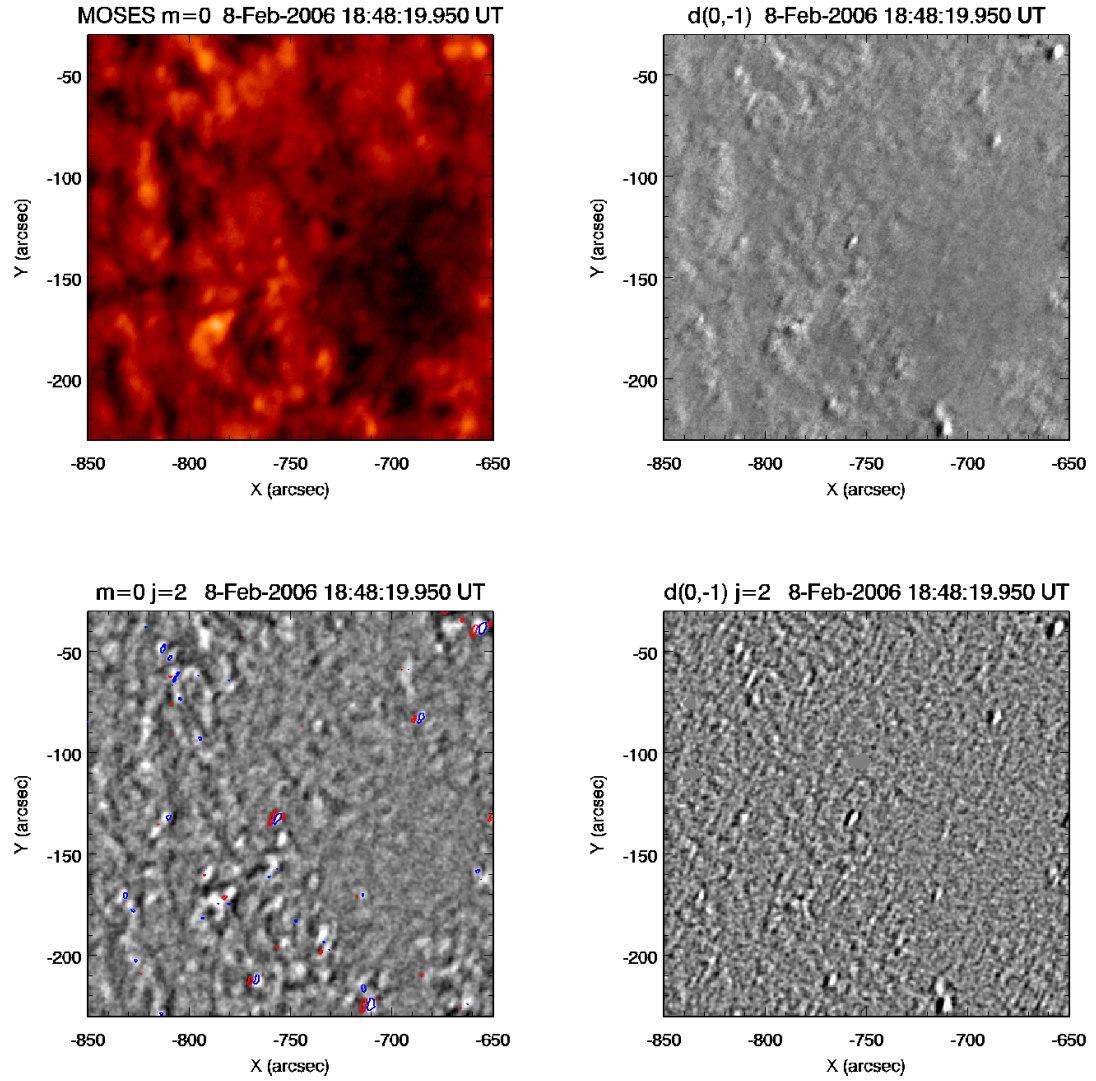


Figure 2.8: Close up of a region of quiet sun. See figure 2.7 for a description of the different panels.

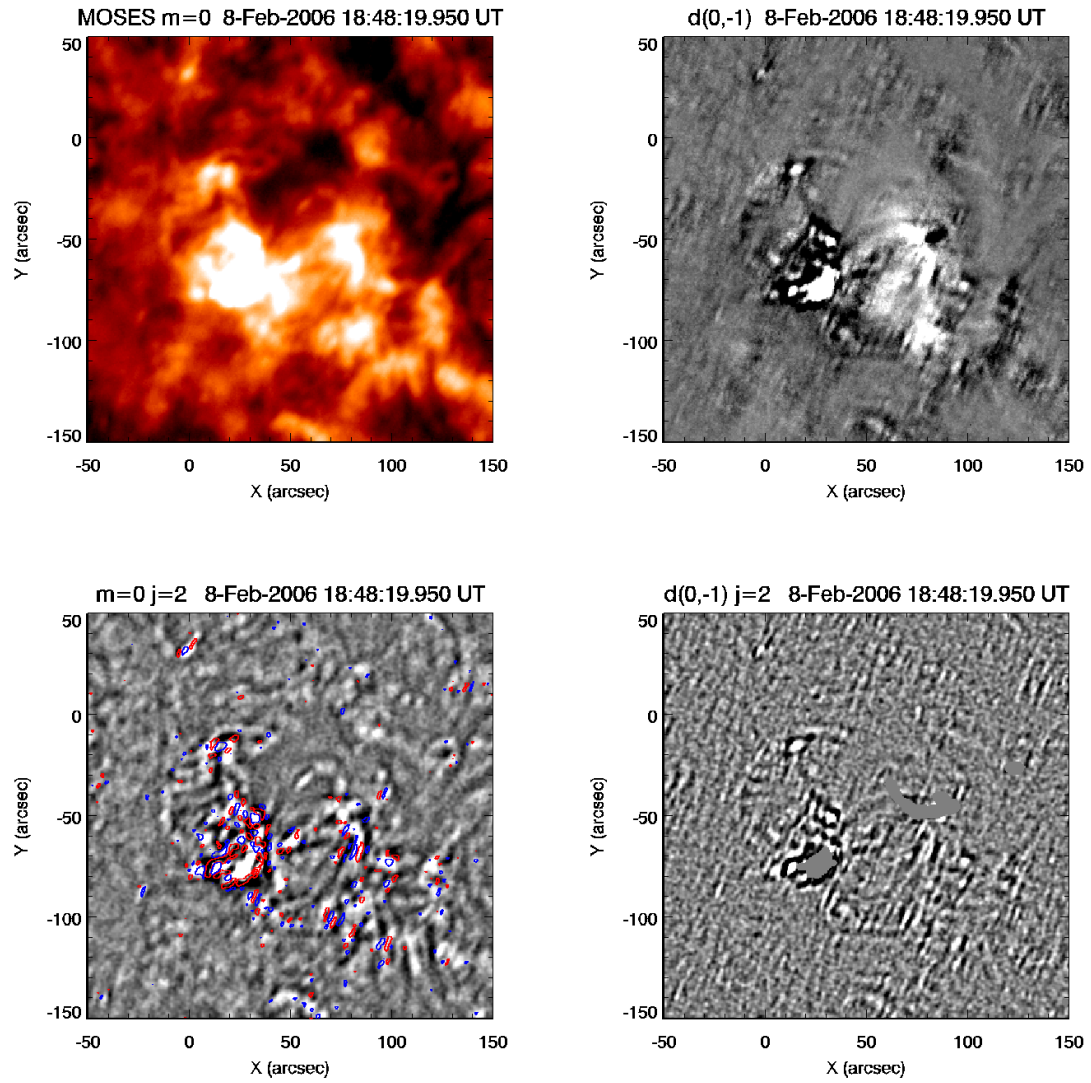


Figure 2.9: Close up of a quiet sun region with relatively strong underlying magnetic network. See figure 2.7 for a description of the different panels.

Both the intensity images (\mathcal{I}_0) and the difference images ($d_{0,-1}$) show lots of small scale variation. The strong differences contoured in figures 2.7, 2.8, and 2.9 are almost always associated with significant¹ positive wavelet coefficients. This association can roughly be characterized one of two ways: the strong difference contours can either coincide with the contours of the wavelet coefficients, or, the difference contours can lie on the periphery of the positive wavelet coefficients. Notable examples of the former type include the features located at [100'',270''] and [160'',200''] in figure 2.7 and the feature at [-750'',-130''] in figure 2.8. These examples are all compact emission with relatively high contrast. They are relatively isolated, i.e., no other strong sources in the immediate neighborhood.

Many if not most of the difference contours are an example of the latter case. A particular example that I show in more detail is located at coordinates [-30'',285''] in figure 2.7. (Fox, 2011) noted that the point spread functions \mathcal{P}_m differ and those differences manifest themselves as a quadrupolar pattern in difference images (figure 2.10, reproduced from (Fox, 2011)). To bring this discussion back to the point, I am trying to locate doppler shifted emission in the *MOSES-06* data by identifying strong differences between the \mathcal{I}_m . (Fox, 2011) showed that due to different \mathcal{P}_m any bright, compact emission will show a strong signature in difference images. These point spread function induced differences will tend to be brightest on the periphery of the actual emission location.

¹In the present context this term is used subjectively; statistical significance testing is discussed in appendices *B* and *C* and applied in chapters 3 and 4.

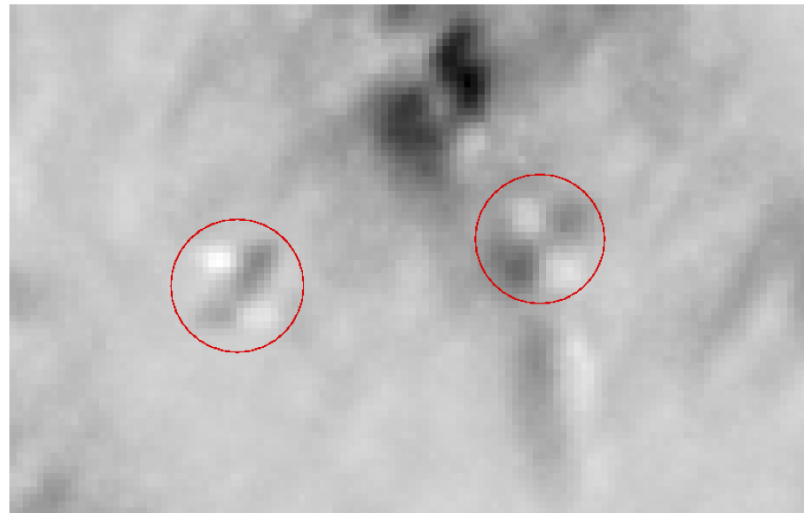


Figure 2.10: Difference image $\mathcal{I}_{+1} - \mathcal{I}_{-1}$ from (Fox, 2011) showing how different point spread functions \mathcal{P}_m in *MOSES-06* different channels manifest themselves as strong signatures in difference images.

The artifacts shown in figure 2.10 arise from compact isolated sources of emission. Consider, then, regions with complicated small scale structure, e.g., the network emission shown in figure 2.9. When every compact source produces something like this quadrupolar pattern in difference image it becomes difficult to say whether a particular peak in the difference image is due to doppler shifts or an artifact caused by the differing point spread functions. Many strong differences show up in the bright network and across the field of view. What is an artifact, and what is not? In the following section I will show by example that at least some of the small scale disparities in $d_{0,-1}$ and $d_{0,+1}$ are due to doppler shifted emission from transition region explosive events.

2.4 Explosive Event Examples

Figure 2.11 shows three compact sources of emission observed by *MOSES-06*. Each row is a different field of view and the object of interest lies in the center of the field of view, near the intersection of the over-plotted white lines. Within each row the \mathcal{I}_{-1} , \mathcal{I}_0 and \mathcal{I}_{+1} channels are ordered from left to right. Remember that the \mathcal{I}_0 images show the location where the emission occurs. The location where the emission is observed in the \mathcal{I}_{-1} and \mathcal{I}_{+1} images depends on the emission wavelength. The dispersion direction in these images is in the horizontal (solar E-W) direction. Emission at He II 304 Å will image to the same location in all of the \mathcal{I}_m . Emission to the blue of He II 304 Å will be shifted to the left in \mathcal{I}_{-1} , and to the right in \mathcal{I}_{+1} . Emission to the red of He II 304 Å will be shifted to the right in \mathcal{I}_{-1} , and to the left in \mathcal{I}_{+1} . The \mathcal{I}_{-1} and \mathcal{I}_{+1} observations in figure 2.11 are over-plotted with blue and red vertical lines to indicate $\pm 100 \text{ km s}^{-1}$ doppler shifts relative to the vertical white line.

The \mathcal{I}_0 data each show a roughly rectangular bright object with 5" spatial extent centered near the intersection of the over-plotted white lines. The objects in each of the separate \mathcal{I}_0 observations have a similar appearance to one another. As seen in \mathcal{I}_{-1} and \mathcal{I}_{+1} , the top row observation shows a compact object centered horizontally on the vertical white line. The middle row observation shows a compact object centered on the blue line in both \mathcal{I}_{-1} and \mathcal{I}_{+1} . The bottom row observation shows two components to the object seen in \mathcal{I}_{-1} and \mathcal{I}_{+1} . One component is centered over the blue line, and one component is centered over the red line.

These observations each have simple interpretations. The top row observation is a compact source emitting at He II 304 Å. The middle row observation is a blue shifted (-100 km s^{-1}) He II 304 Å jet, and the bottom row is a bi-directional ($\pm 100 \text{ km s}^{-1}$)

He II 304 Å jet. In table 1.2 I list potential contaminant (i.e., not He II 304 Å) lines within the *MOSES-06* passband as measured by *SERTS-95* (Brosius et al., 1998). In figure 2.6 I have shown the appearance of contaminant lines in the data and the large horizontal shifts expected from nearby lines. The contaminant line nearest in wavelength to He II 304 Å is the Si 303.3 Å line. At rest emission in this line is shifted 17 pixels relative to He II 304 Å. The shifts seen in the observations of figure 2.11 are 3-4 pixels. These observations are highly unlikely to be due to emission from contaminant lines. They are most likely as just described: doppler shifted He II 304 Å emission.

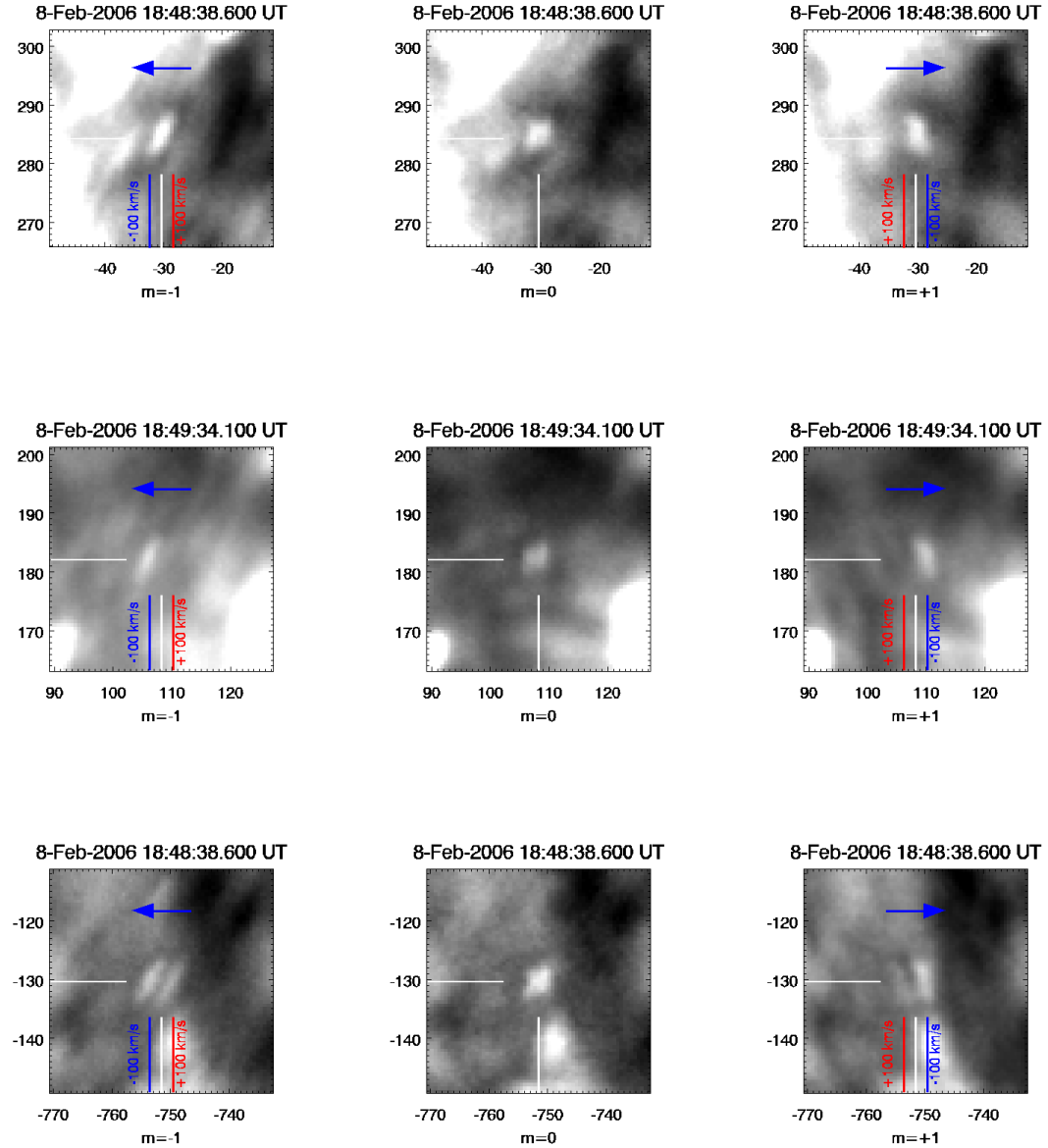


Figure 2.11: Snapshots of three compact objects in the *MOSES-06* data. Each row shows a different object. The columns from left to right show the \mathcal{I}_{-1} , \mathcal{I}_0 , and \mathcal{I}_{+1} data. The blue arrows indicate the blueshift direction in the dispersed orders. Fiducial marks (blue and red vertical lines) indicate $\pm 100 \text{ km s}^{-1}$ shifts relative to the vertical white lines.

Figure 2.12 shows the scale $j = 2$ wavelet coefficients of the observations from figure 2.11. These wavelet images show the small scale structure in the observations. I chose $j = 2$ because it seems to best show the object structure. The $j = 1$ (smallest scale) coefficients are very noisy. The $j = 3$ coefficients appear blurred, e.g., the prominent gap between the two jet components in the bottom row observations is smoothed out in the $j = 3$ coefficients.

The small scale structure of the observations is highlighted in the $j = 2$ wavelet coefficients because high contrast but slowly varying background emission has been filtered out of the data. While the different objects show different spectral characteristics as described above, there are also similarities between the different observations. It has already been noted that the shape of each object is similar in the \mathcal{I}_0 channel. In the \mathcal{I}_{-1} and \mathcal{I}_{+1} channels, the shapes of the shifted emission in the blue jet (middle row, figures 2.11 and 2.12) are similar to the shapes of the unshifted emission in the top tow observation: a SE to NW trending slash in \mathcal{I}_{-1} and a SW to NE trending slash in \mathcal{I}_{+1} . The bi-directional jet (bottom row, figures 2.11 and 2.12) as seen in \mathcal{I}_{-1} and \mathcal{I}_{+1} has two shifted components. The shapes of each of these components are themselves very similar to the shapes of the shifted and unshifted components in the middle and top row observations. In appendix *D* I show many more examples of these shapes associated with compact sources emission in the *MOSES-06* data. It is most likely that this common spatial structure seen in compact emission is due to the instrument point spread functions. The *MOSES-06* primary mirror is a square aperture off-axis sphere, and the design is therefore astigmatic. Combined astigmatism and defocus can largely explain the observed shape of the point spread functions.

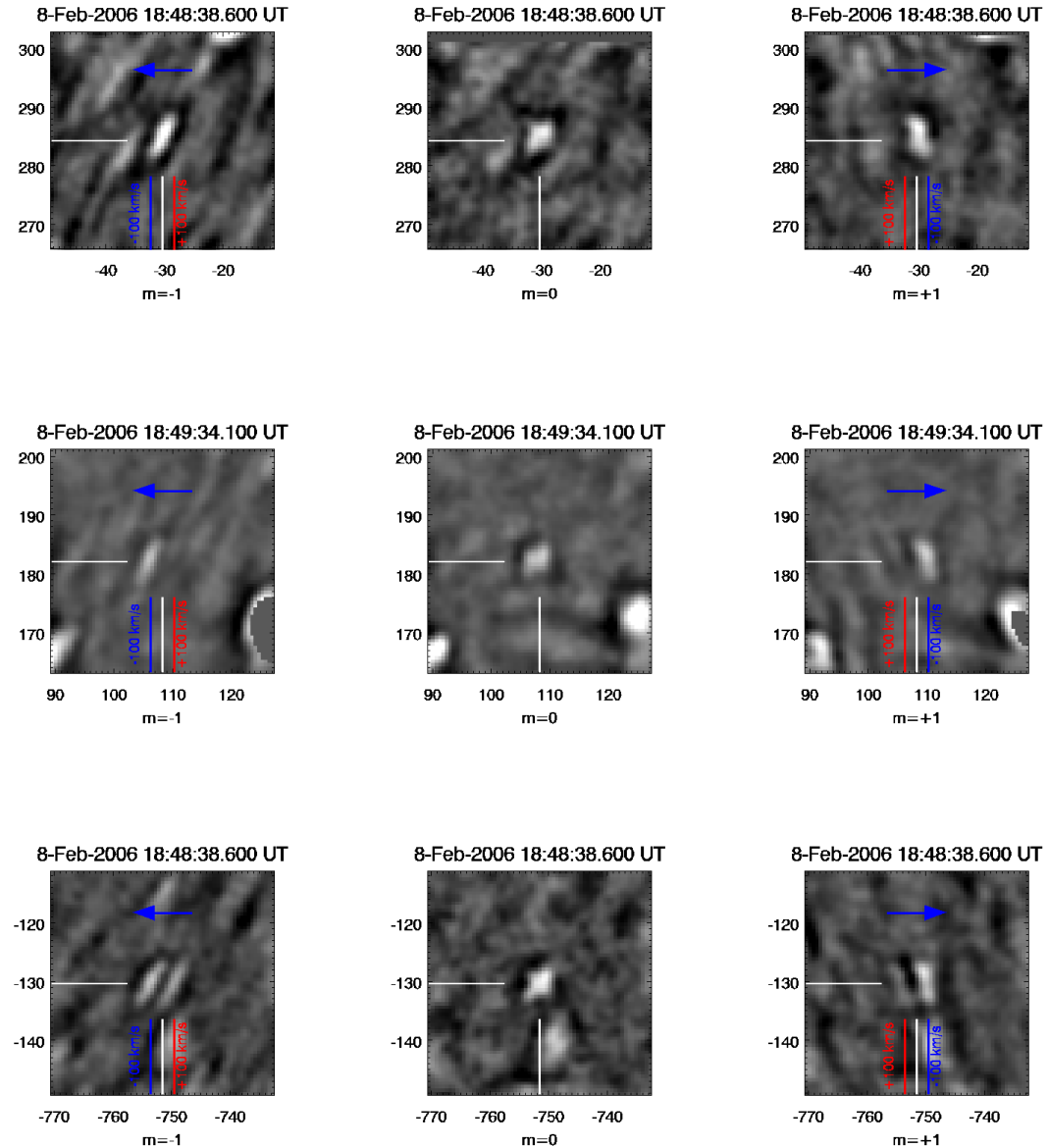


Figure 2.12: Scale $j = 2$ wavelet coefficients of the compact object objects of figure 2.11. See figure 2.11 for further description.

The point-like object is not the only emission present in the observations. A complicated intensity distribution constitutes a background to the object of interest in each of the \mathcal{I}_m . Movies of these objects (appendix A) clearly support a distinction between the compact objects and the background. The compact objects brighten suddenly without noticeable change in the surrounding background intensity. Significantly, the background intensity distribution is approximately the same in each of the \mathcal{I}_m . This can be seen clearly in the upper right panel difference image in figure 2.8. The strong difference region at $[-750'', -130'']$ corresponds to the bi-directional jet observation (bottom row figure 2.11), and is confined to the neighborhood of the compact emission seen in the \mathcal{I}_0 channel. Surrounding the strong difference region the grayscale indicates weak differences, e.g., the \mathcal{I}_m have approximately equal intensity in this wider region. Any spectral radiance distribution in which the line profile does not vary in space will give rise to the same intensity distribution in each of the \mathcal{I}_m . The simplest explanation for the background is spatial variation in the intensity of a spatially uniform He II 304 Å line profile, e.g., the quiet sun profile measure by Andretta et al. (2000).

Regardless of the exact nature of the background, there is a clear distinction between the compact source and the background. This can be seen in the line plots in figures 2.13 and 2.14 which show the rise phase of the blue jet and bi-directional jet, respectively. The profiles are E-W profiles (i.e., along the dispersion direction) through the centers of the compact objects as seen in the \mathcal{I}_0 . The panels in figures 2.13 and 2.14 show, from top to bottom, the \mathcal{I}_{-1} profiles, the \mathcal{I}_0 profiles, and the \mathcal{I}_{+1} profiles. The thicker black profile shown in each panel is the average of a number of profiles from earlier in the flight. The average is taken over time (multiple exposures) and over spectral order (i.e., averaged over \mathcal{I}_{-1} , \mathcal{I}_0 and \mathcal{I}_{+1}). This average profile represents an approximation to the background on which the explosive events are

seen to rise. The vertical blue and red lines indicate the expected shifts (relative to the vertical black line) due to line of sight velocities of $\pm 100 \text{ km s}^{-1}$. The times given are elapsed time (s) since 18:45:54 UT in the middle of a given exposure.

2.4.1 Blue Jet Rise Phase

The rise phase of the blue jet is shown in figure 2.13. The blue jet rise phase shows a “switch on” character within the time resolution of the *MOSES-06* observations. The three profiles in each spectral order at $t = 194 \text{ s}$, $t = 203 \text{ s}$ and $t = 212 \text{ s}$ vary little with time and track reasonably well with the black background profile. Seen in \mathcal{I}_0 (middle panel) the compact source is first clearly present at $t = 232 \text{ s}$, brightens further by $t = 256 \text{ s}$, then appears to fade slightly at $t = 272 \text{ s}$ and again at $t = 282 \text{ s}$. The profile at $t = 282 \text{ s}$ is from a short (1.5 s) exposure and is somewhat underexposed and noisy. The \mathcal{I}_0 profiles of the blue jet appear to change in amplitude but not in shape or location. The vertical black lines in the panels of figure 2.13 indicate the approximate position of the center of the brightening observed in the \mathcal{I}_0 .

The top and bottom panels of figure 2.13 show the \mathcal{I}_{-1} and \mathcal{I}_{+1} profiles of the blue jet. These profiles also show a “switch on” character. Through $t = 212 \text{ s}$ the profiles track with the background profile, then at $t = 232 \text{ s}$ brightening occurs. The vertical blue and red vertical lines plotted over the \mathcal{I}_{-1} and \mathcal{I}_{+1} profiles indicate the expected shifts (relative to the vertical black line) due to $\pm 100 \text{ km s}^{-1}$ doppler speeds. The brightening in the \mathcal{I}_{-1} and \mathcal{I}_{+1} profiles at $t = 232 \text{ s}$ is approximately centered on the blue vertical line. The profiles brighten further at $t = 256 \text{ s}$ then get slightly dimmer at later times. As with the \mathcal{I}_0 profiles, the evolution of the \mathcal{I}_{-1} and \mathcal{I}_{+1} profiles predominantly suggest amplitude changes of a fixed profile shape. Over the observation period the peak of the brightening seen in \mathcal{I}_{-1} and \mathcal{I}_0 remains approximately centered at 100 km s^{-1} blueshift (the blue vertical line).

The observed rise phase of the jet seen in \mathcal{I}_{-1} and \mathcal{I}_{+1} will depend on the acceleration and heating of the emitting plasma. By heating I mean the process which leads to enhanced emission in the He II 304 Å line within the jetting region. If the heating precedes the acceleration there should be brightening at small shifts in \mathcal{I}_{-1} and \mathcal{I}_{+1} which is not observed. If heating occurs during acceleration then the rise phase profiles in \mathcal{I}_{-1} and \mathcal{I}_{+1} should brighten at a range of doppler speeds with the detailed profile depending on the plasma acceleration and heating as well as the temporal and spectral resolution of the observations. The profile at $t = 232$ s is a 24 s exposure preceded by 6 s of readout time. Sometime over this 30 s period the jet brightens, and 24 s of evolution are integrated to form the $t = 232$ s profiles. These profiles are broad but much of that broadening is attributable to the point spread functions. Most of the emission is from fast moving (-100 km s^{-1}) plasma. This implies that either the heating trails the plasma acceleration or the acceleration up to about -100 km s^{-1} is very rapid. After reaching -100 km s^{-1} the plasma speed remains approximately constant for at least the next 50 s.

The profiles and a movie (figure A.2) of this object show hints that there is also a red shifted component to this event. In the profiles this is seen as a broad shoulder on the red side of the vertical black line, which rises starting at $t = 256$ s. In the movie it is fairly clear that there is a faint red component. The blue shifted emission clearly dominates, however, hence the characterization of this object as a blue shifted jet.

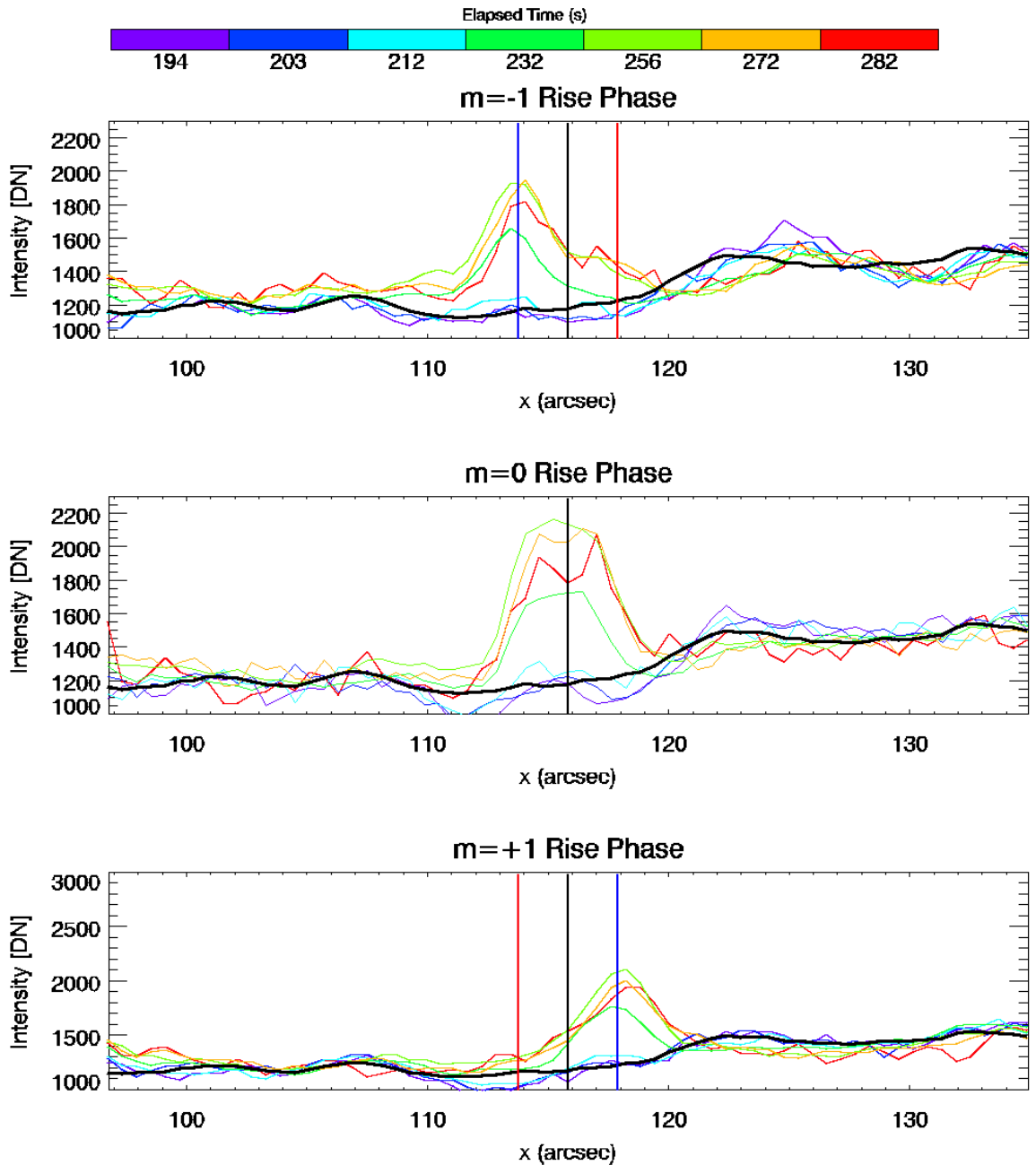


Figure 2.13: Rise phase of the blue shifted jet. Profiles are taken along the horizontal white lines in the panels of figure 2.11. From top to bottom the plots show the \mathcal{I}_{-1} , \mathcal{I}_0 , and \mathcal{I}_{+1} profiles. Elapsed times are from the middle of a given exposure to the beginning of the first exposure in the *MOSES-06* data sequence. Fiducial lines in the images mark the locations of -100 km s^{-1} (blue line) and $+100 \text{ km s}^{-1}$ (red line) doppler shifts relative to the black line. The thick black curve is an approximate background level; see text for details.

2.4.2 Bi-Directional Jet Rise Phase

The rise phase intensity profiles of the bi-directional jet is shown in figure 2.14. The cadence of these observations (about 10 s) is more rapid than the cadence during the blue jet rise phase. The \mathcal{I}_0 profiles (center panel figure 2.14) show a gradual brightening starting at $t = 129$ s and continuing until $t = 157$ s, with roughly half of the peak brightness reached by $t = 138$ s. The profile is approximately unchanged in the next exposure at $t = 166$ s. This brightening again appears to be an amplitude change of a particular profile shape which is almost certainly the profile of the point spread function \mathcal{P}_0 .

As the jet brightens in \mathcal{I}_0 it also brightens in \mathcal{I}_{-1} and \mathcal{I}_{+1} (top and bottom panels of figure 2.14 respectively). At the earliest stage of the brightening ($t = 129$ s) the \mathcal{I}_{-1} and \mathcal{I}_{+1} profiles are indistinct. The most significant deviation of these profiles from the background profile (black line) at this time is the peak just to the red of the -100 km s^{-1} indicator (blue vertical line) in the \mathcal{I}_{-1} profile. By $t = 138$ s a two component profile is plainly visible in both \mathcal{I}_{-1} and \mathcal{I}_{+1} . The blue and red components in the \mathcal{I}_{-1} profiles peak at about $\pm 90 \text{ km s}^{-1}$ as seen in the plotted profiles. The blue and red components in the \mathcal{I}_{+1} profiles suggest about -75 km s^{-1} and $+150 \text{ km s}^{-1}$, respectively.

The blue component in both the \mathcal{I}_{-1} and \mathcal{I}_{+1} profiles brightens in a similar fashion to the brightening in the \mathcal{I}_0 profiles, reaching peak brightness over the period shown at $t = 157$ s then maintaining that profile in the next exposure at $t = 166$ s. The locations of the blue peaks do not change significantly during the rise phase. Curiously, the red component in \mathcal{I}_{-1} appears to brighten throughout the rise phase, while the red component in the \mathcal{I}_{+1} profiles reaches peak brightness by about $t = 138$ s and then maintains that amplitude. In the movie (figure A.3) there appears to be a faint secondary brightening seen in the \mathcal{I}_0 images to the N-W of the jet center.

This secondary source may contribute to the discrepancies between the \mathcal{I}_{-1} and \mathcal{I}_0 observations with respect to the red component evolution and the observed shift magnitudes.

The evolution of the profiles during the bi-directional jet rise phase have a similar character to the blue jet: brightening of a fixed profile shape. This shows as well in the movie (figure A.3). At no time do the \mathcal{I}_{-1} and \mathcal{I}_{+1} profiles appear to be dominated by emission from low speed plasma. After brightening the shifted peak locations do not change significantly; the plasma appears to reach a preferred speed and then remain there. If the plasma is emitting during acceleration the 10 s cadence of these observations places an upper bound on the time required for the plasma to reach this preferred speed, i.e., significantly less than 10 s. Otherwise emission from low speed plasma during acceleration would blur the \mathcal{I}_{-1} and \mathcal{I}_{+1} profiles and more emission would be present at small shifts. At the observed temporal resolution there is a pronounced gap between the blue and red components of the \mathcal{I}_{-1} and \mathcal{I}_{+1} profiles when they first brighten ($t = 138$ s) which indicates that not much emission is present from low speed plasma. Alternatively it is possible that the heating lags the acceleration in time.

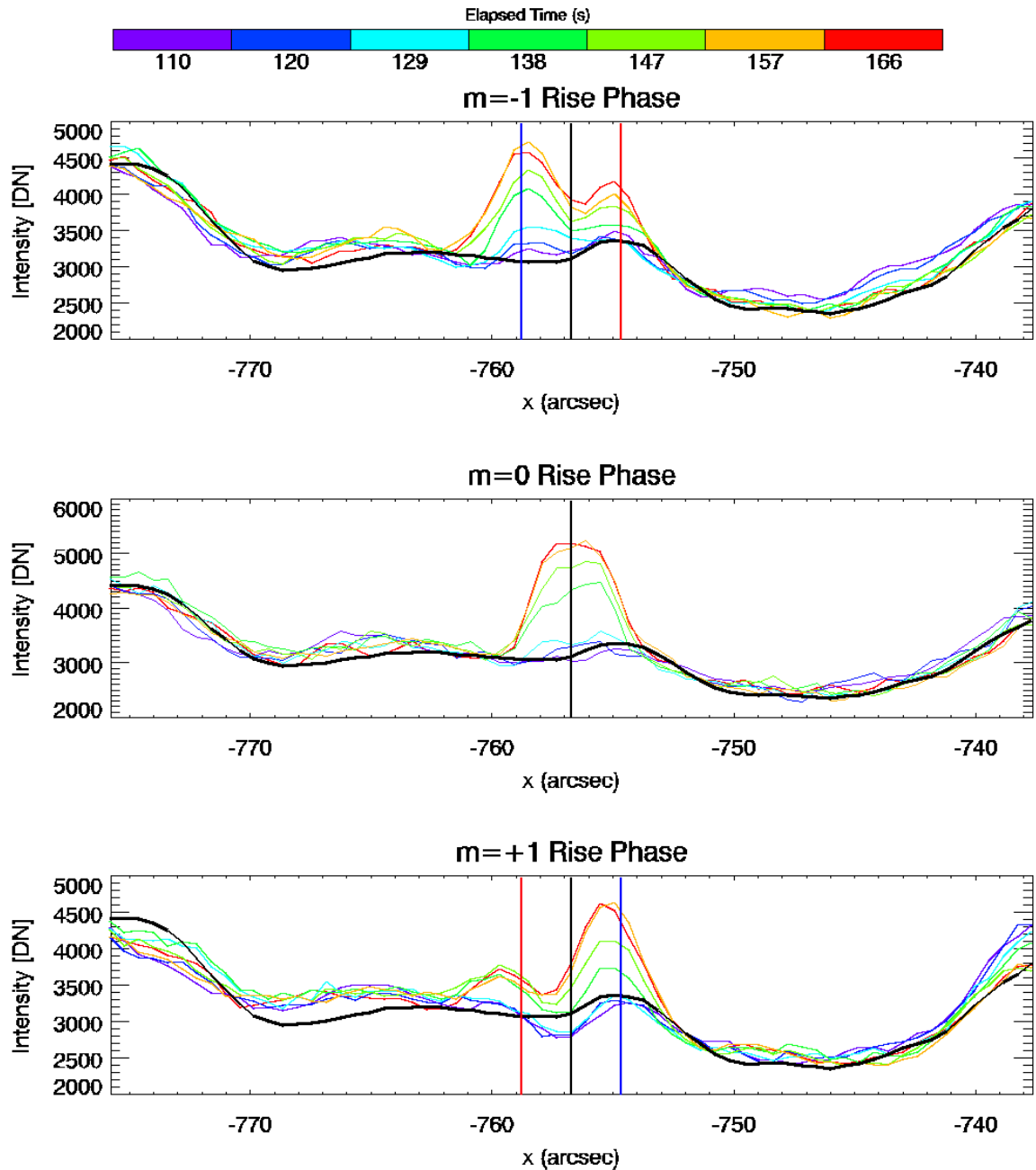


Figure 2.14: Rise phase of the bi-directional jet. See caption of figure 2.13 and the text for details.

The full time evolution of both the blue shifted jet and the bidirectional jet are shown in the middle and bottom rows of figure 2.15. These figures show stack plots of dispersion direction intensity profiles through the centers of the jets. The unshifted compact source (top row figure 2.11) is also shown in the top row for comparison. The red and blue lines over-plotted on the stack plots again show the expected $\pm 100 \text{ km s}^{-1}$ shift locations relative to the over-plotted white lines. I excluded the final two *MOSES-06* exposures from figure 2.15 because they are very noisy. The blue jet is present in four exposures lasting approximately 60 s. The bi-directional jet is present in 13 exposures lasting 145 s. These lifetimes are lower bounds and the events may last beyond the end of the *MOSES-06* flight.

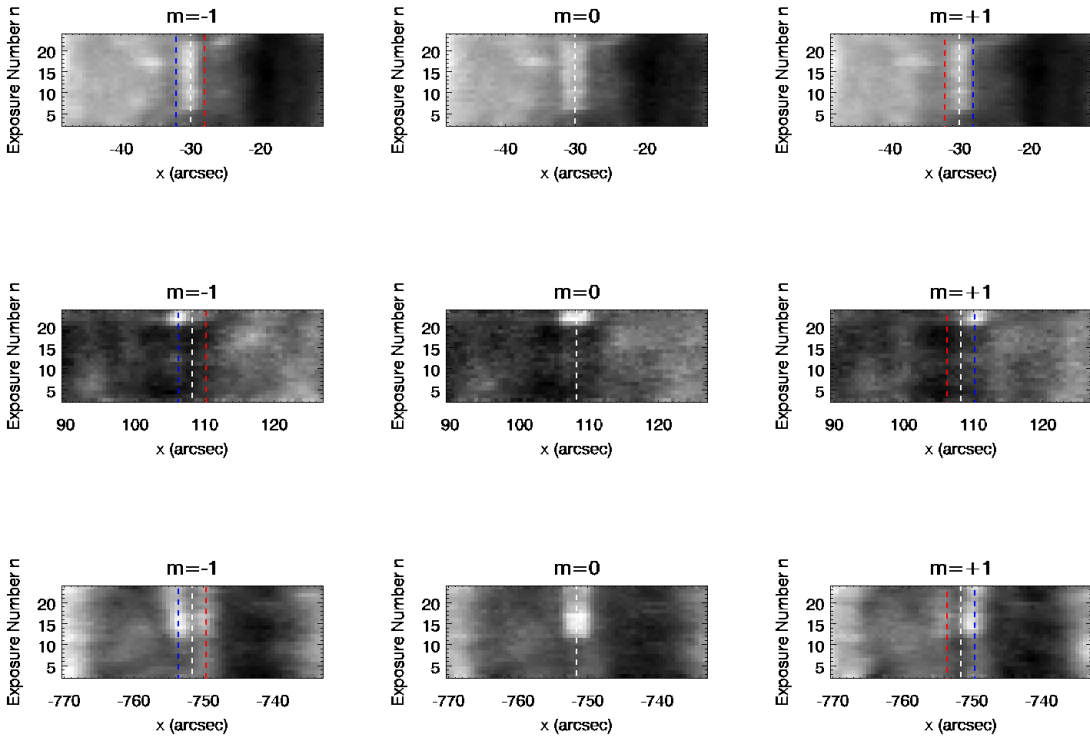


Figure 2.15: Stack plots of profiles through the compact objects of figure 2.11 with position on the horizontal axes and time on the vertical axes. Fiducial lines in the images mark the locations of -100 km s^{-1} (blue line) and $+100 \text{ km s}^{-1}$ (red line) doppler shifts relative to the white vertical line. The columns from left to right show the \mathcal{I}_{-1} , \mathcal{I}_0 and \mathcal{I}_{+1} profiles. The stack plots show profiles from exposure $n = 2$ to exposure $n = 24$. The remaining exposures are fairly noisy.

2.4.3 Doppler Shift Estimates

Detailed line profile estimates from inversion of equation 1.2 are the subject of chapter 3. Up to this point in this chapter I have relied on image fiducial marks to estimate the speeds of doppler shifted components observed in a blue shifted jet and a bi-directional jet. In this section I will estimate the numerical values of these speeds by fitting the intensity profiles with one gaussian component (blue shifted jet) and two gaussian components (bi-directional jet). This type of fitting to obtain velocity estimates from *MOSES-06* data is similar to the “parallax analysis” of Fox et al. (2010).

Figures 2.16 and 2.17 show the \mathcal{I}_{-1} , \mathcal{I}_0 , and \mathcal{I}_{+1} profiles of the blue jet and bi-directional jet, respectively, after subtracting off the black background profile shown in figures 2.13 and 2.14. The blue jet profile is taken from exposure number $n = 22$. The bi-directional jet profile is from $n = 15$. The profile in each spectral order is fitted with one or two gaussians as appropriate. The velocity scale is set by the \mathcal{I}_0 profile fit, with zero velocity corresponding to the centroid of the \mathcal{I}_0 fit.

The fits (figure 2.16) to the blue jet components are best in the component cores near the peak intensity. The fits remain good over a span of about 150 km s^{-1} (about the width of the point spread functions), which covers most of the emission. The fit centroids then should be a good approximation to the doppler velocity of the blue shifted emission.

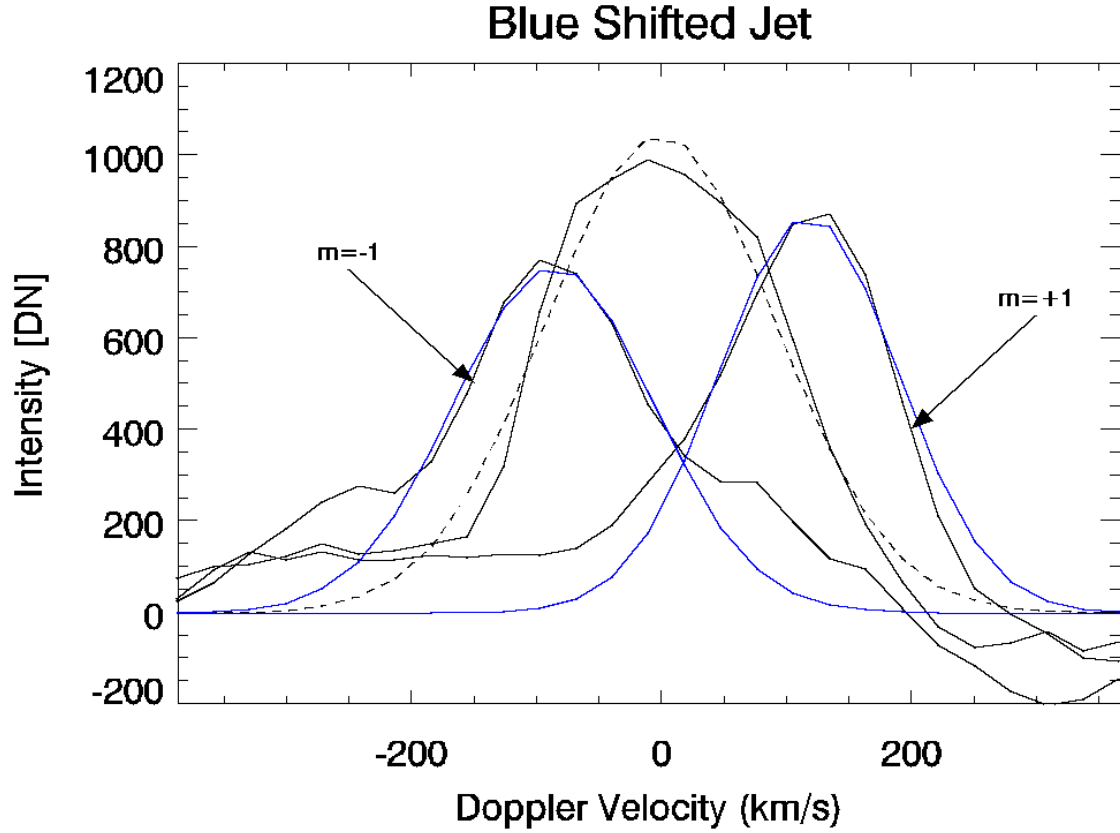


Figure 2.16: Blue jet doppler shift estimates. See text for details.

The fits (figure 2.17) to the bi-directional jet components show good agreement with the data in two important respects. First, the fits well describe the peak regions of the jet components and thus should provide accurate doppler shift estimates. Second, note how well the two component model fits the \mathcal{I}_{-1} and \mathcal{I}_{+1} profiles at small doppler velocities where the components overlap. This is a clue that the emission seen at low velocities is probably due to limited instrument resolution rather than actual emitting plasma.

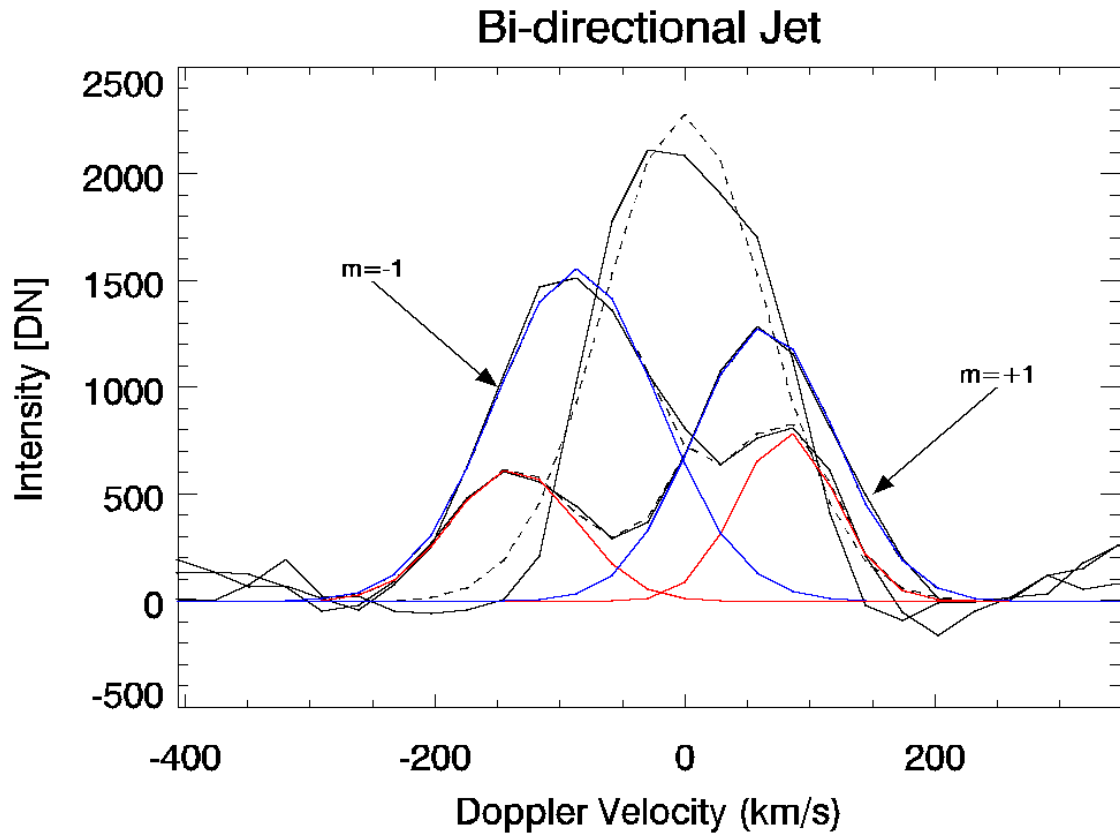


Figure 2.17: Bi-directional jet doppler shift estimates. See text for details.

The estimated doppler speeds for the blue jet and bi-directional jet are summarized in table 2.3.

Table 2.3: Jet speeds derived from gaussian fits.

	Blue Jet	BD Jet Red	BD Jet Blue
$m = -1$	-85	+82	-86
$m = +1$	-118	+136	-64

2.4.4 Magnetic Context

The speeds of the doppler shifted components in the above examples are an order of magnitude larger than the expected width of the thermal velocity distribution at the He II 304 Å formation temperature (50,000 – 80,000 K). This indicates that the energy driving the plasma flows is probably magnetic energy transferred to the plasma during magnetic reconnection. The magnetic context of the blue jet and bi-directional jet (red “x”) are shown in the top and bottom rows of figure 2.18.

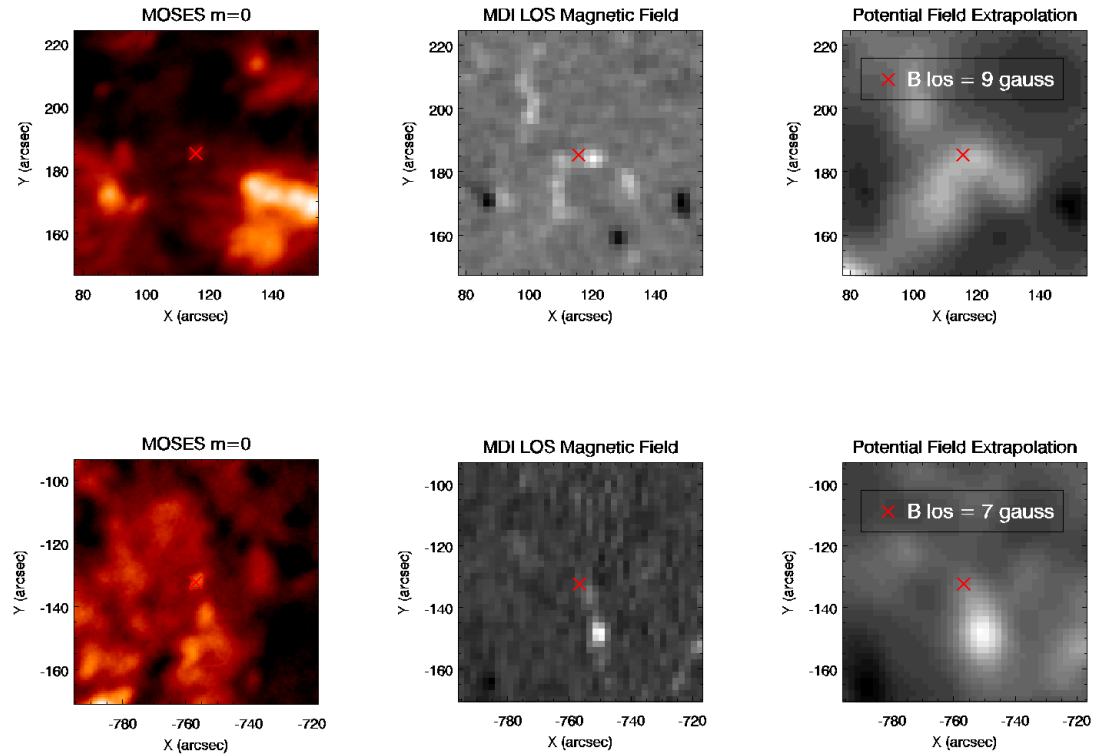


Figure 2.18: Magnetic context of the blue jet (top) and bi-directional jet (bottom). Panels from left to right show intensity (log scaled), *MDI* photospheric line of sight magnetic field strength, and potential field extrapolation up to 5750 km above the photosphere. Jet locations are marked with a red “x”. (Field extrapolation provided by Dr. Dana Longcope)

The blue jet location sits along an arc of locally strong positive polarity magnetic concentrations. These may be network fields in the downflow lane between supergranular cells. The diameter of the arc is about $20''$ which is a reasonable diameter for a supergranule cell. The bi-directional jet is found next to the weaker of a pair of positive polarity magnetic concentrations. The surrounding region is characterized by weak mixed polarity fields.

Magnetic reconnection models predict a characteristic speed for plasma outflows along reconnecting field lines. This speed is the Alfvén speed v_A :

$$v_A = \frac{B}{\sqrt{4\pi\rho}} \quad (2.1)$$

where $\rho = n_e m_p$ is the plasma density, n_e is the electron density, m_p is the proton mass and B is the magnetic field strength. Assuming a pressure $P = 0.05 \text{ dyne cm}^{-2}$ (MacPherson & Jordan, 1999) and temperature $T = 50,000 K$ (peak He II 304 Å ionization fraction from Arnaud & Rothenflug (1985)), $n_e = 3.6 \times 10^9 \text{ cm}^{-3}$ and $\rho = 6 \times 10^{-15} \text{ g cm}^{-3}$. The extent to which the emitting plasma traces reconnecting field lines depends on the plasma β (equation 1.1). When $\beta \ll 1$ the plasma is frozen onto the field lines. Figure 2.19 shows β and v_A plotted as a function of the magnetic field strength.

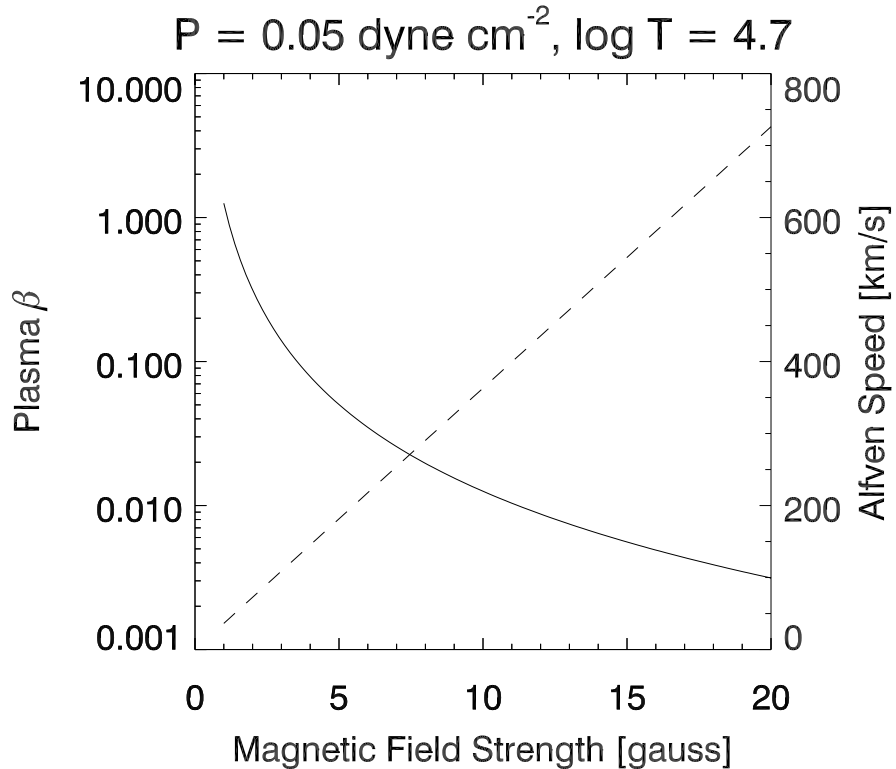


Figure 2.19: Plasma β (solid) and the Alfven speed (dashed) in the transition region.

The magnetic field strength present in the blue and bi-directional jet examples are estimated from a potential field extrapolation of the photospheric magnetic field to be 9 gauss and 7 gauss respectively. The calculated plasma β is then 0.015 in the blue jet and 0.025 in the bi-directional jet. In both cases β is small and thus the emission should trace reconnecting field lines. Assuming the density derived above is appropriate for the reconnection region the expected Alfven speeds are $v_A = 326 \text{ km s}^{-1}$ for the blue jet and $v_A = 254 \text{ km s}^{-1}$ for the bi-directional jet. These values are in excess of what is observed by a factor of three (see table 2.3). The

plasma density was calculated using an assumed filling factor – the ratio of observed volume to emitting volume – is unity. Dere et al. (1987) found filling factors of 1% in observations of C IV 1548 Å in the transition region. An independent density measurement would help to constrain the expected Alfvén speed.

2.4.5 Mass and Kinetic Energy Flux

The spectral signatures of the blue jet and the blue component of the bi-directional jet suggest a flow of mass and energy from the reconnection site upwards into the atmosphere. The total mass in the upward flow is approximated as

$$M = \rho A v t \quad (2.2)$$

where ρ is the density derived above, A is the cross sectional area of the outflow, v is the outflow speed, and t is the event lifetime. The total kinetic energy carried by the flow is

$$E_K = \frac{1}{2} M v^2 \quad (2.3)$$

The minimum lifetime for the blue jet is $t_{blue} = 60$ s. The minimum lifetime of the bi-directional jet is $t_{bd} = 145$ s. The area of the outflow region can be approximated from the area of the brightening seen in these events in the I_0 channel. These areas are approximately 5" wide but given the size of the *MOSES-06* point spread functions the true outflow area must be much smaller than this. I will assume a circular outflow area of diameter 1"; this gives $A = 2.1 \times 10^{16}$ cm². The average upwards outflow speed in the blue jet and bi-directional jet are 101 km s⁻¹ and 75 km s⁻¹ respectively (see table 2.3). Using these parameters the total mass and kinetic energy flow upwards from the reconnection sites is given in table 2.4 assuming a filling factor of one. The kinetic energy values are within the range given by Winebarger et al. (2002).

Table 2.4: Estimates for the upwards mass and kinetic energy flow from the blue jet and bi-directional jet.

	M [g]	E_K [erg]
Blue Jet	1.5×10^{10}	7.7×10^{23}
Bi-directional Jet	2.7×10^{10}	7.6×10^{23}

2.5 Additional Explosive Event Examples

The events in this section were selected manually based on clear evidence of strong doppler shifts in the *MOSES-06* image data. Candidate locations were selected based on strong difference image signatures; many candidates were rejected because the differences appeared to be artifacts due to the point spread functions. Figure 2.20 shows an \mathcal{I}_0 image from the 2006 flight overlaid with the locations of the objects presented in this section. A close up view of the coronal hole is shown in figure 2.21. The objects themselves are shown in figure 2.22. Panels 1 through 41 are snapshots of different explosive events. Panels 42 through 45 are examples of compact emission without obvious shifts and are included to show the shape of the point spread functions. The panels are arranged into three sub-panels with the \mathcal{I}_{-1} , \mathcal{I}_0 , and \mathcal{I}_{+1} data from bottom to top. The events are displayed as the scale $j = 2$ wavelet coefficients in order to show the small scale structure. The strong influence of the instrument point spread functions can be seen in all of these observations.

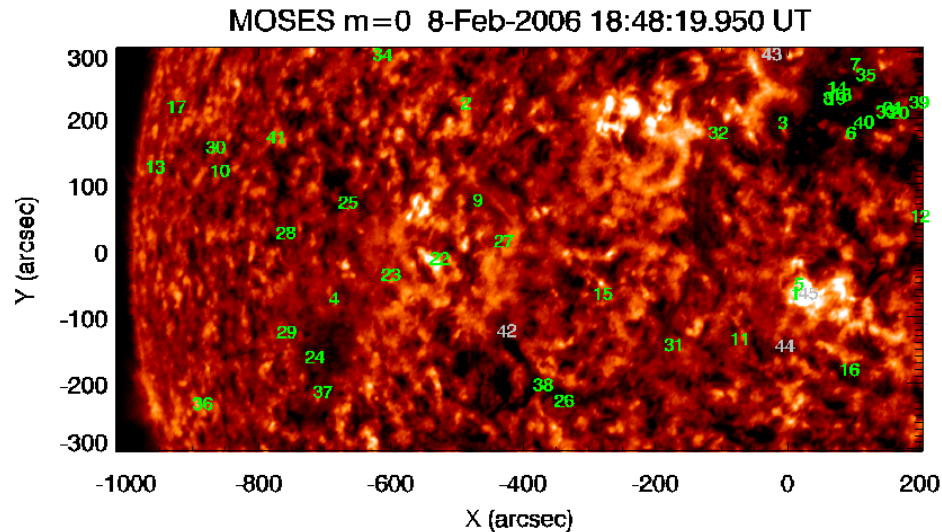


Figure 2.20: *MOSES-06* \mathcal{I}_0 image with green numbers indicating the locations of the explosive events discussed in section 2.5. The grey numbers indicate point-like emission included with the examples in figure 2.22 to show the instrument point spread functions.

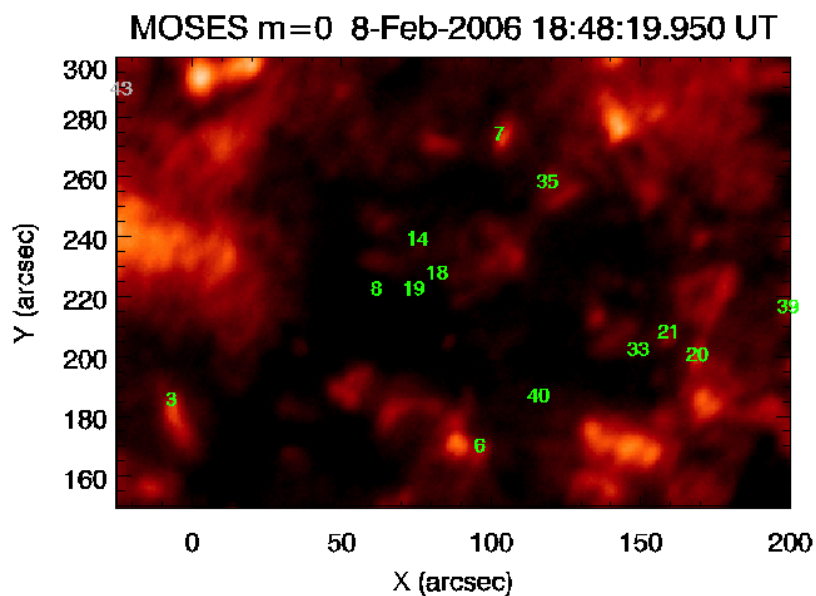


Figure 2.21: Explosive events identified within the coronal hole.

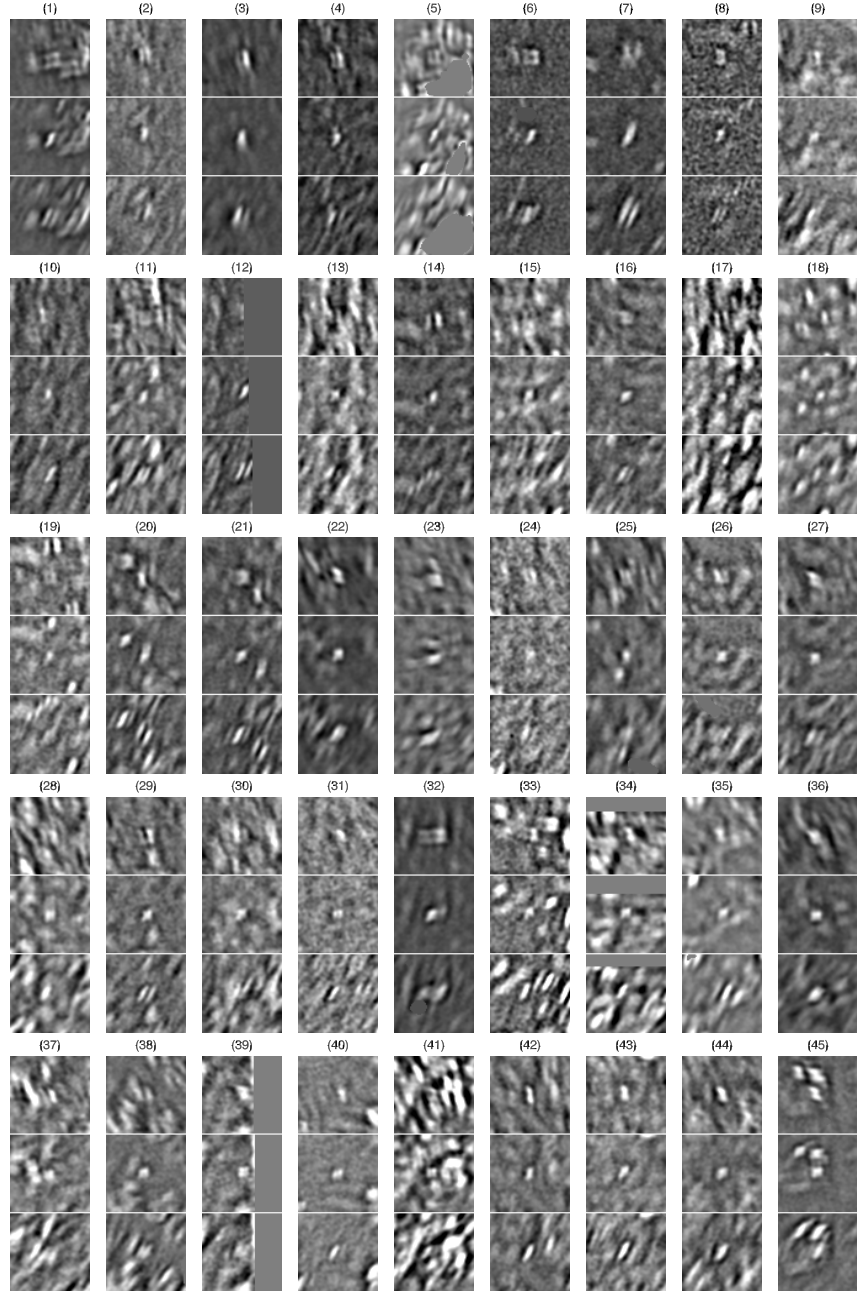


Figure 2.22: Examples of explosive events observed by *MOSES-06*. Shown are the scale $j = 2$ wavelet coefficients of the \mathcal{I}_m . Each panel has three sub-panels. Sub-panels from top to bottom: \mathcal{I}_{+1} , \mathcal{I}_0 and \mathcal{I}_{-1} . Each sub-panel has a 37.5" field of view.

In total 41 explosive events are identified in figures 2.20-2.22. 34 of these events

were within the potential field extrapolation field of view. Figure 2.24 summarizes the properties of these explosive events.

The explosive events were classified as red jets, blue jets, or bi-directional jets if the \mathcal{I}_m visually supported that designation. Red jet examples are shown in figure 2.22 panels 10 and 35. Blue jet examples are shown in figure 2.22 panels 18, 31, 33, 34, and 40. Bi-directional jet examples are shown in figure 2.22 panels 1, 3, 7, 15, 17, 20, 24, 26, 29, and 32. Events classified as Bi-directional jet* are events that appear strongly bi-directional in one of the \mathcal{I}_{-1} or \mathcal{I}_{+1} but not the other. Examples of bi-directional jet* are shown in figure 2.22 panels 5, 8, 11, 12, 16, 19, 27, and 28. The remaining events, classified as other, are for one reason or another difficult to classify in the previous categories. In all 12 events out of 41 (29% of all events) were identified within the coronal hole which is only about 5% of the *MOSES-06* field of view. These results are summarized in the left hand table of figure 2.24.

Figure 2.23 shows the explosive event locations plotted over the *MDI* magnetogram between [799°E, 198°W] and [302°S, 300°N]. The over-plotted contours are the +5 gauss (white) and -5 gauss (black) contours of a potential field extrapolation provided by Dr. Dana Longcope. The field was extrapolated from the *MDI* photospheric magnetic field measurements to a height of about 5750 km above the photosphere. The explosive event locations are over-plotted with a green dot at each event site. This magnetogram was taken two hours after the *MOSES-06* flight so the event locations have been shifted 18" to the west to account for solar rotation.

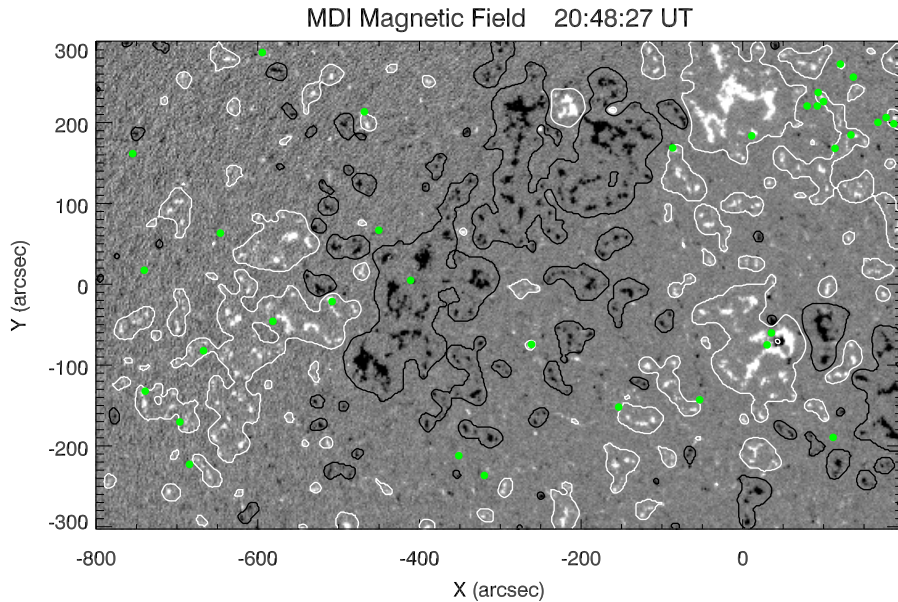


Figure 2.23: Explosive event locations (green dots) over-plotted on an *MDI* magnetogram taken two hours after the *MOSES-06* flight. Contours show the +5 (white) and -5 (black) gauss contours of a potential field extrapolation up to 5750 km.

The magnetic context of 34 out of 41 total explosive events is characterized in the right hand table of figure 2.24. Six events were not included because they fell outside of the field of view of the magnetic field extrapolation. More than 80% of 34 events were found in positive field regions. The mean field magnitude averaged over all events is 8.0 G although examples exist within regions of stronger field. Two explosive events are found in regions with no measurable line of sight magnetic field. Inspection of figure 2.23 shows many events are located near the boundary where weak mixed field regions meet unipolar field concentrations. Of 34 events plotted in figure 2.23 24 (70.5%) are located within 10" of a 5 G contour line.

Property	# Occurrences	Magnetic Properties	Value
Red Jet	2 (5%)	# Events	34
Blue Jet	5 (12%)	$\langle B \rangle$	8.0 G
Bi-directional Jet	10 (24%)	B_{min}	-19 G
Bi-directional Jet*	8 (20%)	B_{max}	61 G
Other	15 (37%)	$\# B > 0$	28 (82%)
Coronal Hole	12 (29%)	$\# B < 0$	4 (12%)
Quiet Sun	28 (68%)	$\# B = 0$	2 (6%)

Figure 2.24: Properties of explosive events observed with *MOSES-06*. The left table summarizes the event types and locations; the right table summarizes the event magnetic properties. Bi-directional jet* indicates that the event appears strongly bi-directional in one of the \mathcal{I}_{-1} or \mathcal{I}_{+1} but not the other. B values are from the potential field extrapolation. Seven of the 41 explosive events fall outside the field extrapolation field of view so only 34 events are characterized magnetically. See text for further description.

2.6 Summary

In this chapter I have described the *MOSES-06* observations of He II 304 Å emission in the solar transition region. Of particular interest, many compact, bright features in the images have been identified as transition region explosive events. The spatial structure of the compact features is heavily influenced by the point spread functions, different in each image channel.

I looked at the rise and time evolution of two example events: a blue shifted jet and a bi-directional jet. The doppler speeds associated with the jet components were calculated by assuming the intensity distribution in the *MOSES-06* dispersed channels was equivalent to average spectrum of the event plus a variable background. Upon background subtraction and gaussian fitting the example events show doppler speeds of approximately 75-100 km s⁻¹.

Characteristic of both types of jets is an apparent lack of emission from low speed plasma. The blue jet line profile can be described with a single gaussian component that peaks at a doppler velocity of approximately 100 km s^{-1} (figure 2.16). The bi-directional jet line profile can be described by two gaussian components with peak shifts of -75 km s^{-1} and $+100 \text{ km s}^{-1}$ (figure 2.17). The bi-directional jet components are well separated and the two gaussian fit well describes the low velocity region of the line profile suggesting that the observed low velocity emission may be due to the instrument resolution. Regardless of the precise strength of the low velocity emission the example event line profiles are dominated by high speed emission.

It is interesting to contrast these observations with the explosive events observed in Si IV 1402 Å with *IRIS* by Innes et al. (2015). The Si IV line profiles have significant emission at high velocity but are dominated by a low velocity core. The line profiles may sometimes be well represented by a single broad gaussian (Innes et al., 2015). As the Si IV line profiles evolve in time they sometimes show additional brightening at low velocity which Innes et al. (2015) argue is evidence for tearing mode reconnection based on magnetohydrodynamic (MHD) modeling. The example *MOSES-06* explosive events have weak line core emission and show no indication of core brightening over the observation period. The bi-directional jet in particular supports the Petschek reconnection explosive event model of Innes & Tóth (1999) rather than the tearing mode model of Innes et al. (2015). The difference between the He II and Si IV line profiles – core dominated versus wing dominated – may indicate that He II and Si IV explosive events fall in different regions of the reconnection phase diagram of Ji & Daughton (2011). It would be interesting to investigate the relationship between He II and Si IV explosive events via a *MOSES* underflight of *IRIS*.

The MHD model of Innes et al. (2015) also predicts an acceleration phase at the

onset of an explosive event, wherein emitting plasma is accelerated to the Alfvén speed. I looked in detail at the rise phase of the two example explosive events and could find no indication of an early acceleration phase. Both the blue and bi-directional jets had a “switch-on” characteristic where from first appearance the event line profiles are wing dominated. See the discussion in sections 2.4.1 and 2.4.2.

I showed 41 additional explosive event examples from the *MOSES-06* data and looked at their locations in relation to the surrounding atmosphere. Almost 30% of the identified events were located in a coronal hole in the NW corner of the *MOSES-06* field of view. The coronal hole covers just 5% of the field of view. The coronal hole lacks network emission and the He II 304 Å intensity distribution is somewhat simpler than in the quiet sun. It is possible that a selection bias exists that favors coronal hole explosive events in the *MOSES-06* data. My experience suggests that the coronal hole has an unusual density of explosive events relative to the surrounding quiet sun. In order to develop the tentative conclusion that He II 304 Å explosive events occur preferentially in coronal holes it will be necessary to carefully evaluate selection biases in the identification of explosive events. Automatic detection of explosive events and evaluation of selection bias is a major goal of future work.

I also examined the explosive event locations relative to the photospheric magnetic field. A potential field extrapolation of a *MDI* observation was used to estimate magnetic field strength in the transition region. The average magnetic field strength over all identified explosive events is 8 G. At this field strength the Alfvén speed is of order 100 km s^{-1} given a reasonable estimate for the transition region density.

2.7 Acknowledgements

I would like to thank Dr. Dana Longcope for helping to analyze and interpret the magnetic observations shown in this chapter, and to Dr. Piet Martens and Dr. Jim Klimchuk for helpful discussions about the physical properties of explosive events and the transition region.

CHAPTER THREE

A NEW TECHNIQUE FOR *MOSES* INVERSIONS3.1 Introduction

In this chapter I'll expand on the observational analyses of chapter 2. I wish to estimate spectral line profiles from the *MOSES-06* data using all of the available data in a self consistent way. I will generally refer to the passage from data to spectral line profile estimates as *inversion*. As noted in chapter 1, the ideal image equation that describes the *MOSES-06* images (equation 1.3) says that the \mathcal{I}_m are projections of the solar spectral radiance $\nu(x, y, \lambda)$. I wish to use the \mathcal{I}_m to estimate ν .

The reconstruction of a function from its projections is called *tomography* (Kak & Slaney, 1988). Two classes of solution methods have thus far dominated the literature: Fourier Backprojection methods (Bracewell & Riddle, 1967), and Algebraic Reconstruction Techniques (ART) (Gordon et al., 1970). Based on promising results from Fox (2011) I have chosen to perform inversions using an algebraic reconstruction technique.

Algebraic reconstruction techniques were introduced by Gordon et al. (1970). Under simple assumptions relating to the way the projections are approximated the tomography problem is reduced to the solution of a set of linear algebraic equations. The equations are solved using the Kacmarz method (Kaczmarz, 1937) in which corrections are iteratively applied to an initial guess based on the disparity between the data and projections of the guess. Two correction methods were proposed by Gordon et al. (1970), one using an additive correction and one using a multiplicative correction (multiplicative ART, or MART). The additive correction is based on the difference between the data and projections in a given iteration; the multiplicative

method uses ratios. MART has one obvious consequence that, given positive definite data, the solution is positive definite. This is advantageous in the present context in that the physical quantity of interest $\nu(x, y, \lambda)$ must be positive definite.

This chapter is organized as follows. In section 3.3 I will describe the particular MART algorithm due to Mishra et al. (1999) and use it as a starting point for *MOSES-06* inversions. In order to investigate systematic errors inherent in the solution method I use a synthetic explosive event observation modeled on the bi-directional jet observation of chapter 2. In section 3.4 I show artifacts that result from the limited number of projection angles (three) available in the inversion. In section 3.5 I will improve the inversion results by inverting the explosive event in isolation. I isolate the explosive event from the background using a technique called partial reconstruction from partial wavelet coefficients (Bijaoui & Rué, 1995; Starck et al., 1998). Once isolated, the explosive event inversion shows artifacts due to the point spread functions, different in each spectral order. I combined the MART algorithm with the Richardson-Lucy deconvolution algorithm (Richardson, 1972; Lucy, 1974). The combined algorithm when applied to the isolated explosive event is able to recover the known spectrum.

3.2 Synthetic Data

In order to test the MART algorithm I have generated a synthetic observation for reconstruction. I synthesized a bi-directional jet with similar characteristics to the bi-directional jet described in chapter 2 (bottom panel of figure 2.11). The synthesized spectrum has two thermal width gaussian components, one blue shifted and one red shifted with doppler shift magnitude of 100 km s^{-1} . The jetting region is assumed to occupy one pixel. The background for the synthetic observation consists of spatially uniform gaussian emission at zero doppler shift and He II 304 Å thermal

width. Together the background and jet spectrum constitute a synthetic spectral radiance. The peak intensity in the synthetic \mathcal{I}_0 image is 990 DN and the background intensity is 540 DN.

The appearance of compact objects in the *MOSES-06* data is strongly influenced by the instrument point spread functions. In appendix *D* I derive an estimate for the *MOSES-06* point spread functions using the compact unshifted object shown in the top panel of figure 2.11. The synthetic radiance is projected in accordance with equation 1.3 to form synthetic images. The synthetic images are then convolved with their respective point spread functions. Finally noise is added to the synthetic images. The *MOSES-06* noise model is the subject of appendix *C*. The synthetic images and the underlying jet spectrum is shown in figure 3.1.

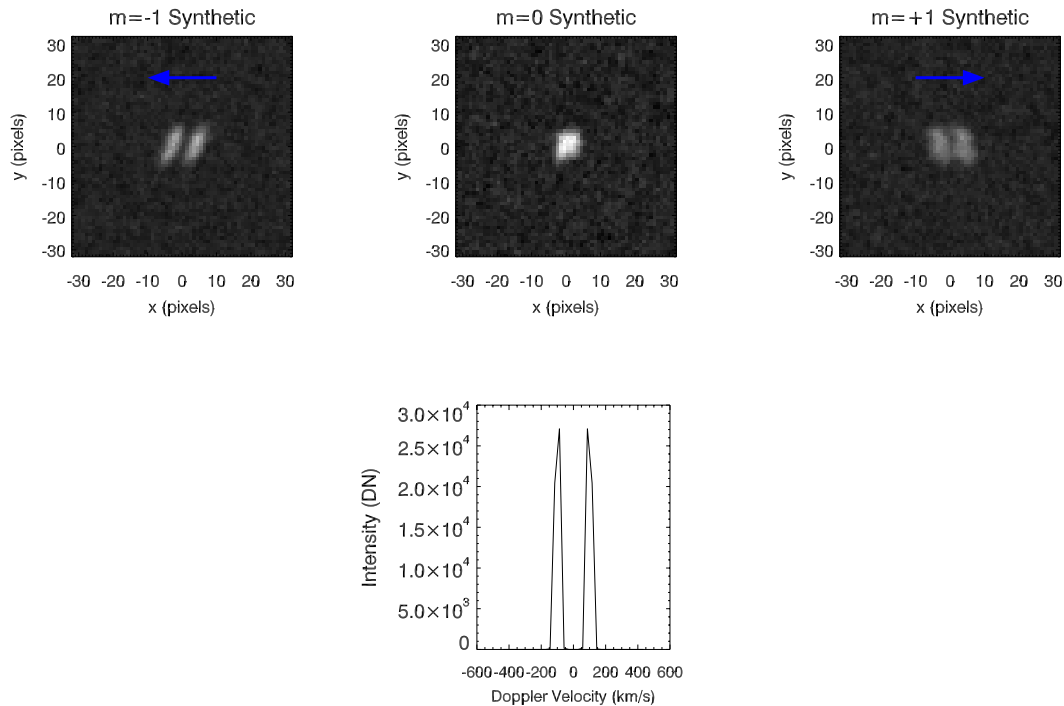


Figure 3.1: Synthetic *MOSES-06* observation of a bi-directional jet. Top row left to right: $m = -1$, $m = 0$, $m = +1$. Bottom row shows the jet spectrum. The blue arrows indicate the blueshift direction in the dispersed channels.

3.3 The Multiplicative Algebraic Reconstruction Technique

A variety of MART algorithms are available to choose from. The basic MART algorithm used in this chapter is due to Mishra et al. (1999):

1. Initialize guess cube $\nu(x, y, \lambda) = 1$
2. Project $\nu(x, y, \lambda)$ to form guess projections p_m
3. Calculate multiplicative error: $\epsilon_m(x, y) = \mathcal{I}_m/p_m$
4. Threshold $\epsilon_m(x, y)$; retain coefficients that are significant (3σ) with respect to the noise
5. Extrude $\epsilon_m(x, y)$ along the relevant projection direction to obtain error cubes $\epsilon_m(x, y, \lambda)$
6. Correct: $\nu = \nu \prod_m \epsilon_m^{(1/N_m)}$
7. Iterate steps 2–6

The algorithm was implemented in the Interactive Data Language (IDL) and the code is based on the Smooth Multiplicative Algebraic Reconstruction Technique (SMART) code (Kankelborg et al., 2012). Step 4 (thresholding) is a wavelet based noise reduction method described in section *B.2.1*.

3.4 Testing MART with Synthetic Data

I applied MART to the synthetic data of figure 3.1. The solution volume has 64×64 spatial pixels, and 31λ pixels centered on $\lambda = 0$. Figure 3.2 shows the reconstructed \mathcal{I}_0 image and the reconstructed spectrum of the jet.

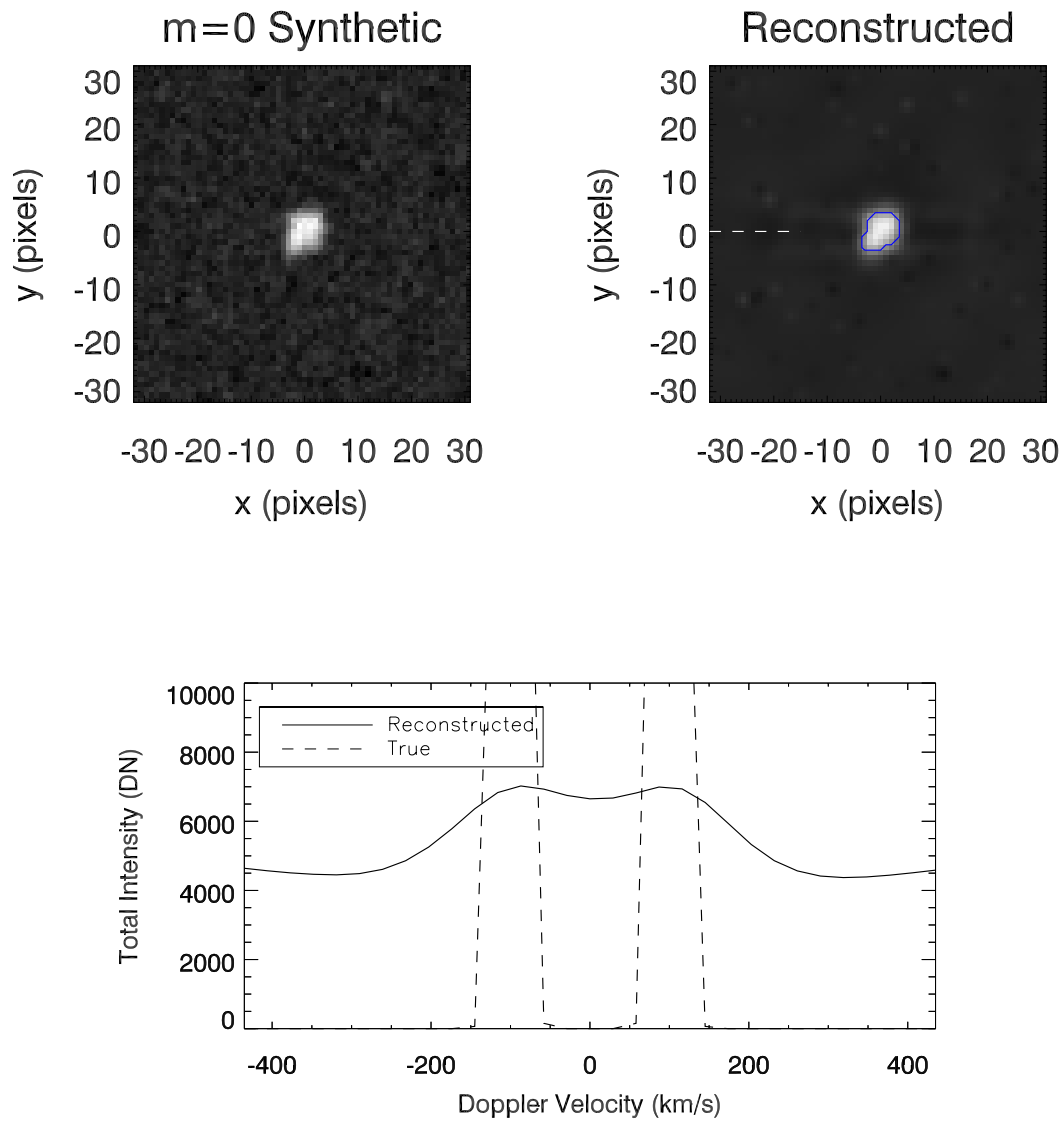


Figure 3.2: *Top Left:* Synthetic \mathcal{I}_0 image. *Top Right:* \mathcal{I}_0 image reconstructed with MART. The blue contour is the 50% level of the jet intensity above the background. *Bottom:* Total reconstructed $\nu(x, y, \lambda)$ within the blue contour shown in upper right, over-plotted with the known synthetic jet spectrum.

The reconstructed \mathcal{I}_m appear to agree with the data but the reconstructed jet spectrum differs significantly from the known synthetic spectrum. It is possible to identify the two jet components in the reconstructed spectrum but the contrast of the components is low. At large doppler shifts ($>250 \text{ km s}^{-1}$) the reconstructed spectrum shows nearly uniform non-zero intensity. The reconstructed spectrum looks like a low resolution version of the synthetic spectrum riding on a nearly uniform background.

A slice (figure 3.3) of the reconstructed radiance through the jet center (horizontal white line in figure 3.2, upper right panel) shows some interesting features of the MART reconstruction.

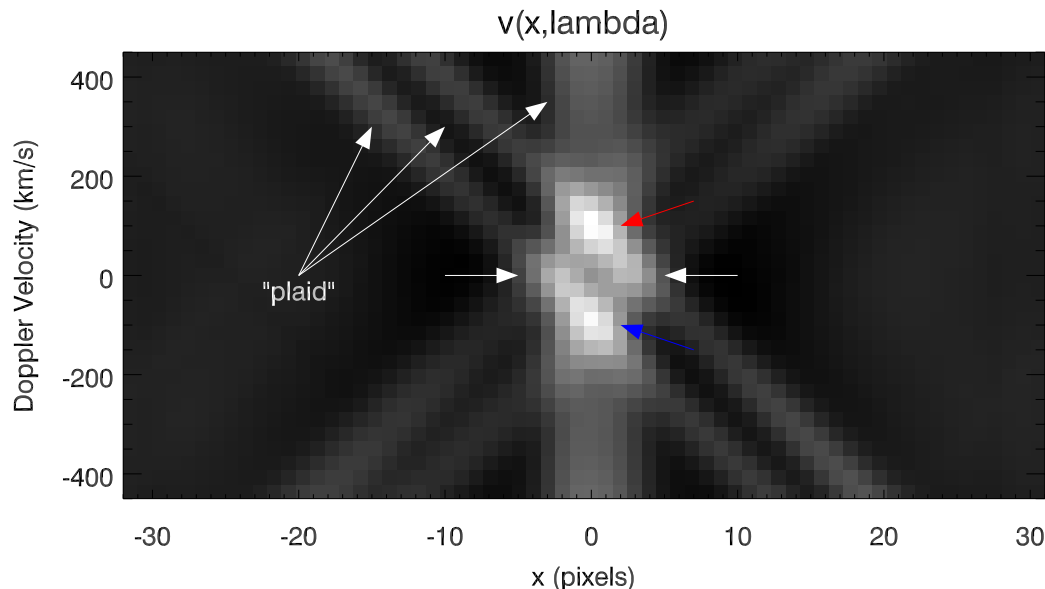


Figure 3.3: A slice of the reconstructed radiance through the jet in the dispersion (x) direction.

The jet components can be identified and are marked with the blue and red arrows in figure figure 3.3. There are also significant structures that are artifacts of the reconstruction. Three white arrows in figure 3.3 marked “plaid” point to ridges or streaks of intensity that have a plaided appearance. These streaks are known to

occur in tomographic reconstructions where there are very few measured projections (Agafonov, 2004). The *MOSES-06* measures only three projections and thus these streak artifacts are very prominent in the reconstructions. Locations where the streaks intersect are amplified. This amplification is desirable at the locations of the blue and red jet components but can occur elsewhere as indicated by the horizontal white arrows in figure 3.3. The peaks indicated by the horizontal white arrows are artifacts that arise from the intersection of streaks in the reconstruction that do not correspond to real spectral features. A naive interpretation of the radiance of figure 3.3 suggests four emitting sources: blue and red jet components, and two spatially separate low velocity components. The low velocity components lie partially within the envelope of the jet location as outlined in the upper right panel of figure 3.2 so the reconstructed jet spectrum (bottom panel figure 3.2) is erroneously enhanced at low velocity.

I will now show that the “plaid” or streak artifacts may be greatly reduced by reconstructing the jet emission separately from the background emission. The synthetic jet is a compact source on a uniform background. The discrete wavelet coefficients corresponding to the jet and background then peak at different scales: large scales in the background and small scales in the jet. The wavelet coefficients of the synthetic \mathcal{I}_m up to scale $j = 3$ are shown in figure 3.4. The blue contours indicate where the coefficients are 3σ statistically significant (see section *B.2.1*) with respect to the image noise. The 3σ noise level is calculated from the noise model (chapter *C* table *C.3*) and not from the observations. In the case of this trivial background the contours show the jet emission is well separated in wavelet space from the uniform background. This wavelet space separation makes it possible to reconstruct the jet emission using a technique known as *partial reconstruction from significant wavelet coefficients*, or partial reconstruction.

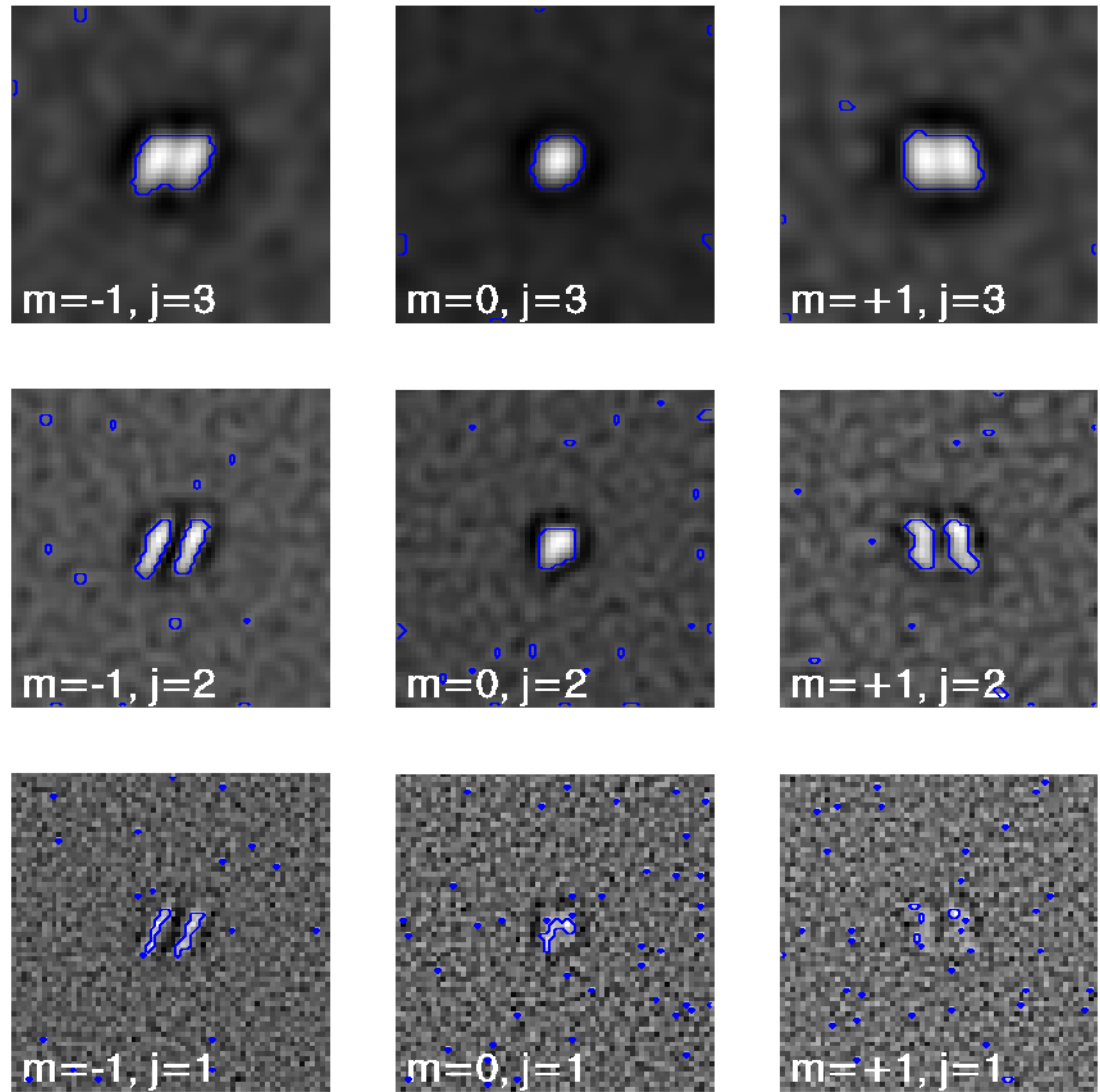


Figure 3.4: The wavelet coefficients of the synthetic \mathcal{I}_m up to scale $j = 3$ over-plotted with contours indicating the 3σ significance level of the coefficients.

3.5 MART with Partial Reconstruction

An algorithm to reconstruct astronomical image features from wavelet coefficients is described in Bijaoui & Rué (1995); Starck et al. (1998) and is known as partial reconstruction. The wavelet transform is described in appendix *B*. In partial reconstruction an object is generally described as a local maximum among positive, significant coefficients in wavelet space. Significant wavelet coefficients which are connected to the maxima in both scale and space are part of the same object. The object coefficients therefore occupy a volume in wavelet space. The goal of partial reconstruction is to construct an image whose wavelet coefficients are the same as those of the object, within the volume on which the object is defined. If the reconstructed image is p , the object coefficients are \tilde{q} , and A is the operator which transforms p and projects the result onto the support of \tilde{q} , the partial reconstruction problem is minimization of $\|Ap - \tilde{q}\|$, where $\|\cdot\|$ represents the L^2 norm. The partial reconstruction method is iterative, beginning with $p(x, y) = 0$:

1. Initialize $p(x, y) = 0$
2. Calculate $Ap = \tilde{p}(x, y, j)$
3. Determine the additive error in the coefficients on the support of the object:

$$\tilde{\epsilon} = \tilde{p} - \tilde{q}$$
4. Threshold $\tilde{\epsilon}$; retain only statistically significant (3σ) coefficients
5. Calculate correction $\epsilon(x, y) = A^{-1}\tilde{\epsilon}$
6. Update $p = p + \epsilon$
7. Threshold $p > 0$

8. Iterate steps 2 through 7. Iterations end when no significant coefficients may be found in $\tilde{\epsilon}$

The operator A^{-1} is inverse to the operation A . A projects an image into a list of wavelet coefficients; A^{-1} back projects a list of wavelet coefficients into an image. A^{-1} resolves the stepped appearance created by hard thresholding of the wavelet coefficients by applying a scale dependent smoothing to the significant coefficients at each scale. The smoothing at scale j , $j > 1$ is implemented by applying the wavelet transform up to scale $j - 1$ to the scale j significant coefficients. The result of this transform is $j - 1$ wavelet images, and the smooth residual c_{j-1} . The A^{-1} operator replaces the scale j significant residuals with c_{j-1} . I also chose to smooth the scale 1 significant coefficients, with the kernel aa^T , where $a^T = [0.25, 0.5, 0.25]$ and T denotes the transpose.

I used partial reconstruction to separate the synthetic jet emission from the background in each of the \mathcal{I}_m . The coefficients used for the reconstruction are those inside contours obviously associated with the jet emission as indicated in figure 3.4. Two partial reconstructions were carried out, one using coefficients up to scale $j = 2$, and one using coefficients up to scale $j = 3$. These reconstructions are shown in figure 3.5.

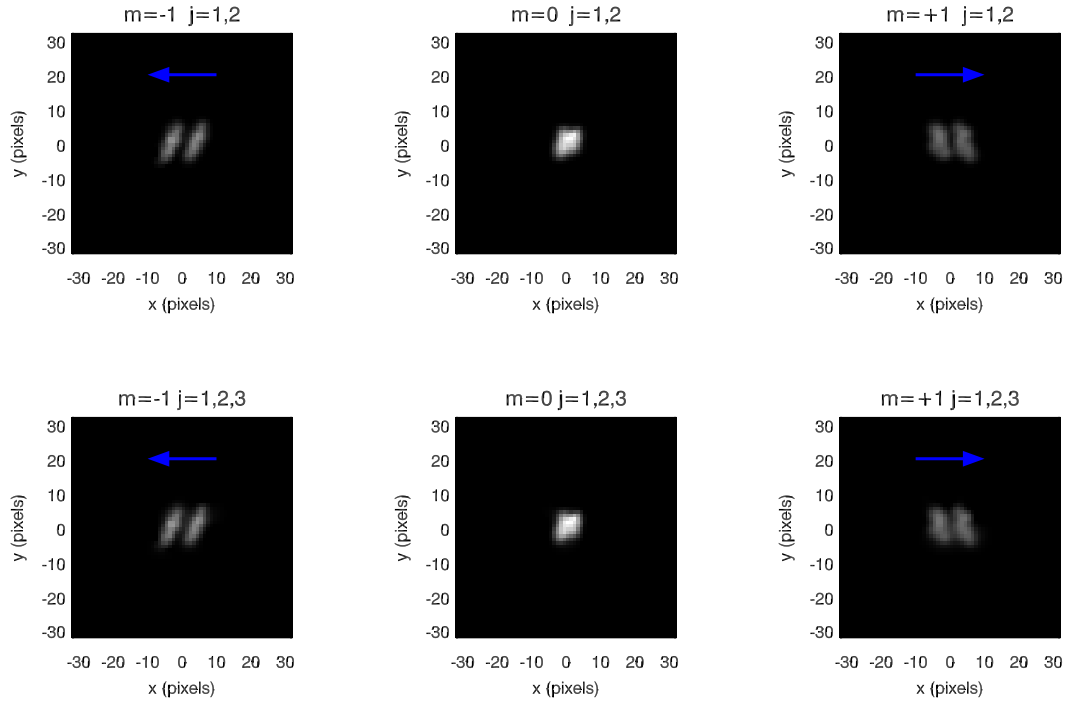


Figure 3.5: Partial reconstruction of the synthetic jet using $j \leq 2$ (top row) and $j \leq 3$ (bottom row). Columns from left to right show \mathcal{I}_{-1} , \mathcal{I}_0 , and \mathcal{I}_{+1} channels.

Figure 3.6 shows profiles through the synthetic data (top row) and the reconstructions (bottom row). The top row profiles are over-plotted with the residual after subtracting the reconstructions from the synthetic data. The inclusion of the scale $j = 3$ coefficients makes little difference in the reconstructions in the \mathcal{I}_{-1} and \mathcal{I}_0 channels. In the \mathcal{I}_{+1} channel it is apparently necessary to include the scale $j = 3$ coefficients in the reconstructions to recover all of the jet emission in that channel. The bottom row of figure 3.6 plots the partial reconstructions over the known jet profiles.

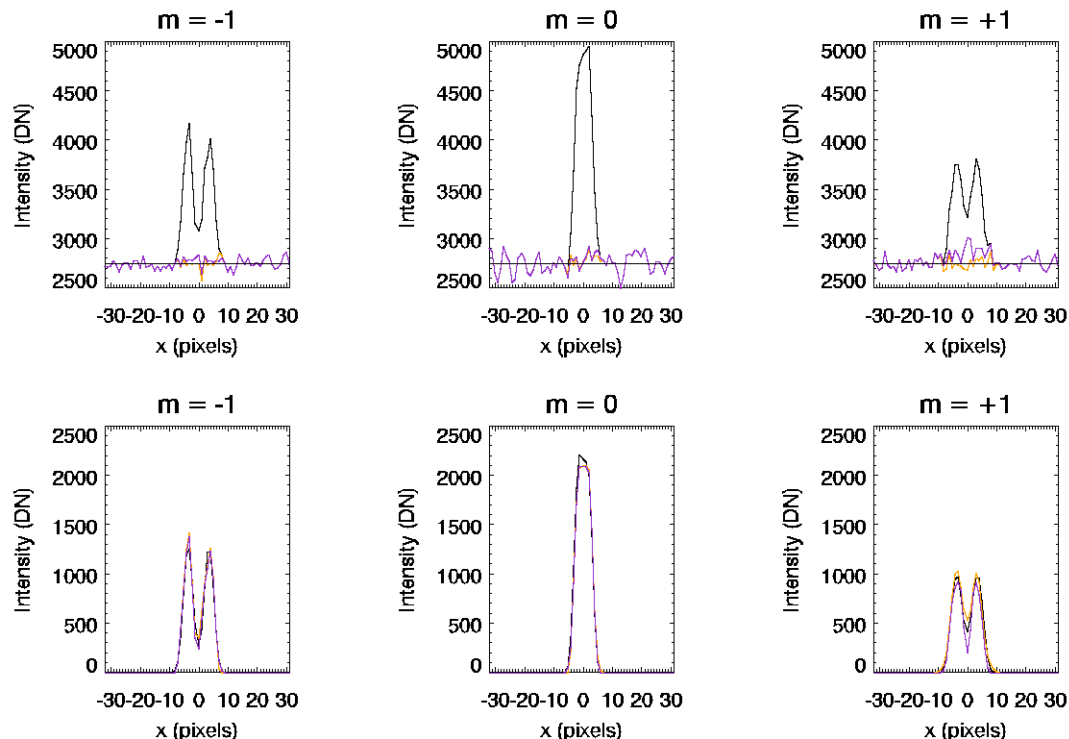


Figure 3.6: *Top row:* Profiles through the synthetic jet (black) over-plotted with the residual after subtraction of the partial reconstruction results. The purple residual is from partial reconstruction using the $j = 1$ and $j = 2$ wavelet coefficients; the orange residual uses the wavelet coefficients up to scale $j = 3$. The horizontal black line indicates the true background level. *Bottom row:* Profiles of the partial reconstruction result using the $j \leq 2$ (purple) and $j \leq 3$ (orange) wavelet coefficients in the reconstruction; the black profiles are the known synthetic profiles.

I applied MART to the partial reconstruction results in the bottom panel of figure 3.5. A slice of the reconstructed radiance is shown in figure 3.7. The streak artifacts are now gone but the spurious low velocity peaks (indicated by the white arrows) remain.

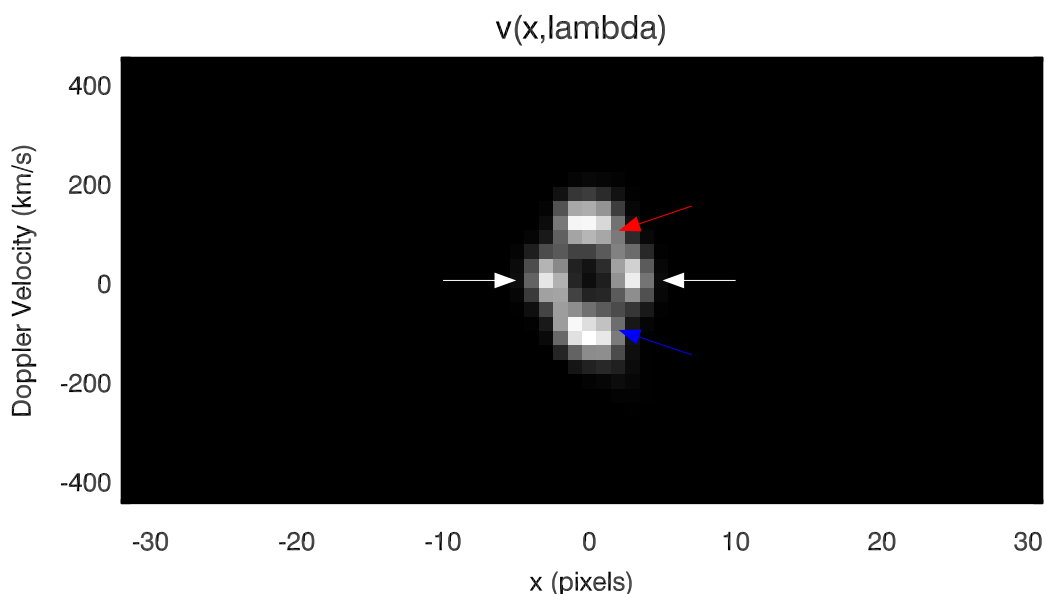


Figure 3.7: An $x - \lambda$ slice of the radiance reconstructed using the methods of section 3.5.

The reconstructed spectral line profile is plotted in figure 3.8. The blue and red components of the line profile show improved contrast relative to the MART reconstruction of section 3.4, but the profile also shows a strong low velocity component and significant broadening in the wings. The low velocity component results from the peaks indicated by white arrows in figure 3.7.

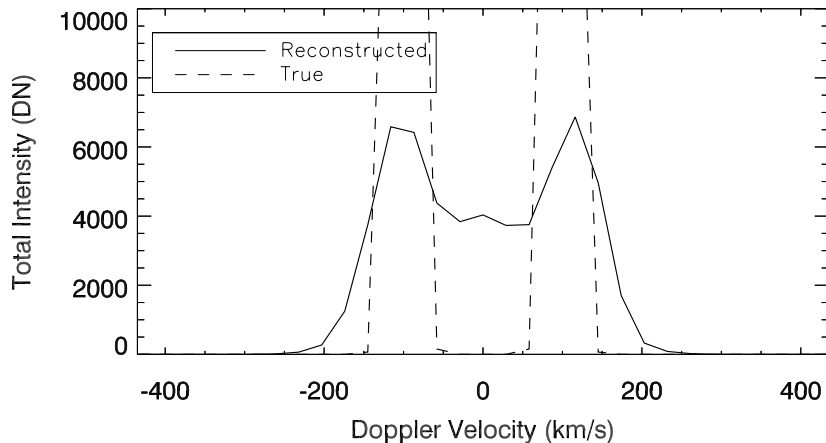


Figure 3.8: Total reconstructed radiance within the blue contour shown in the upper right panel of figure 3.2. The reconstruction uses the methods described in section 3.5. The dotted line plots the known synthetic jet spectrum.

The broadening in the wings can be understood by looking at a $y - \lambda$ slice of the reconstructed radiance (figure 3.9). The $y - \lambda$ slice shows a significant red-ward shift in the spectrum with increasing y . This occurs because the \mathcal{I}_{-1} and \mathcal{I}_0 point spread functions are tilted relative to the dispersion axis. Recall that Fox (2011) observed that compact objects can show a quadrupolar pattern in difference images (see figure 2.10) that was attributed to the instrument point spread functions. The quadrupolar patterns of figure 2.10 imply a change from blueshift to redshift with increasing y . That change from blue to red is exactly what is observed in the $y - \lambda$ slice of figure 3.9. The inversion interprets the spatial structure resulting from tilted point spread functions as real doppler shifts. The velocity of each jet component moves red-wards by about 60 km s^{-1} over the approximate y length of the jet (10 pixels). When averaged over the whole jet the line profile (figure 3.8) is broadened due to the sum of these spurious shifts.

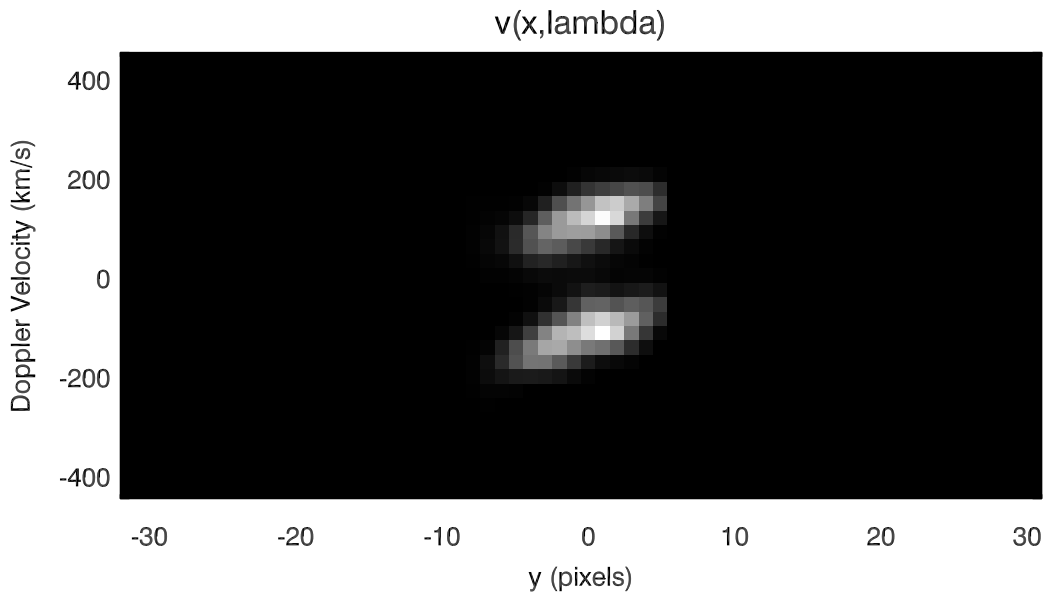


Figure 3.9: A $y - \lambda$ slice of the radiance reconstructed using the methods of section 3.5.

In summary, at this point two outstanding systematic errors dominate the *MOSES-06* inversions: a low velocity component and substantial broadening. Both the low velocity component and the broadening are systematic errors due to the instrument point spread functions. In section 3.6 I will show how to account for the point spread functions in *MOSES-06* inversions.

3.6 MART, Partial Reconstruction and Deconvolution

In order to account for the instrument point spread functions in the inversion I will combine the MART algorithm with the well known Richardson-Lucy deconvolution algorithm (Richardson, 1972; Lucy, 1974). I do this by enclosing each MART iteration in a Richardson-Lucy iteration as follows:

1. Initialize guess cube $\nu(x, y, \lambda) = 1$

2. Project to form guess projections p_m
3. Convolve: $p_m \rightarrow p_m * \mathcal{P}_m(x, y)$
4. Calculate multiplicative error: $\epsilon_m(x, y) = \mathcal{I}_m/p_m$
5. Threshold $\epsilon_m(x, y)$; retain only statistically significant (3σ) coefficients
6. Convolve: $\epsilon_m \rightarrow \epsilon_m * \mathcal{P}_m(-x, -y)$
7. Extrude $\epsilon_m(x, y)$ along the relevant projection direction to obtain error cubes
 $\epsilon_m(x, y, \lambda)$
8. Correct: $\nu = \nu \prod_m \epsilon_m^{(1/N_m)}$
9. Iterate

I applied the MART with deconvolution algorithm to the partial reconstruction results shown in the bottom panel of figure 3.5. Figure 3.10 shows the \mathcal{I}_0 image resulting from the inversion. Prior to deconvolution the jet area was defined by the blue contour in the upper right of figure 3.2. The deconvolution localizes the jet emission much more accurately; the new jet area is indicated by the blue contour in figure 3.10 and approximately outlines a single pixel.

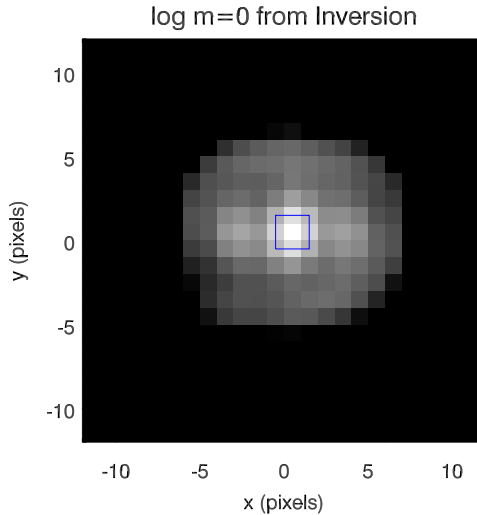


Figure 3.10: Inverted \mathcal{I}_0 using the methods of section 3.6. The jet area is localized to essentially a single pixel. The \mathcal{I}_0 image is shown in logscale to show faint detail. The 50% intensity contour is shown in blue; only the central pixel in the image lies above this contour.

The line profile of the jet within the blue contour indicated in figure 3.10 is shown in figure 3.11 over-plotted with the known synthetic spectrum. The blue contour is the 50% level of the peak inverted intensity. Within this 50% contour the inversion recovers 70% of the true jet intensity which recall should be localized to a single pixel. The line profile calculated by summing over the whole inversion volume (labeled as th 0% contour in figure 3.11) recovers additional intensity but the shape of the profile is unchanged. So the deconvolution is unable to perfectly localize the jet emission spatially but this does not degrade the spectral characteristics of the inverted jet.

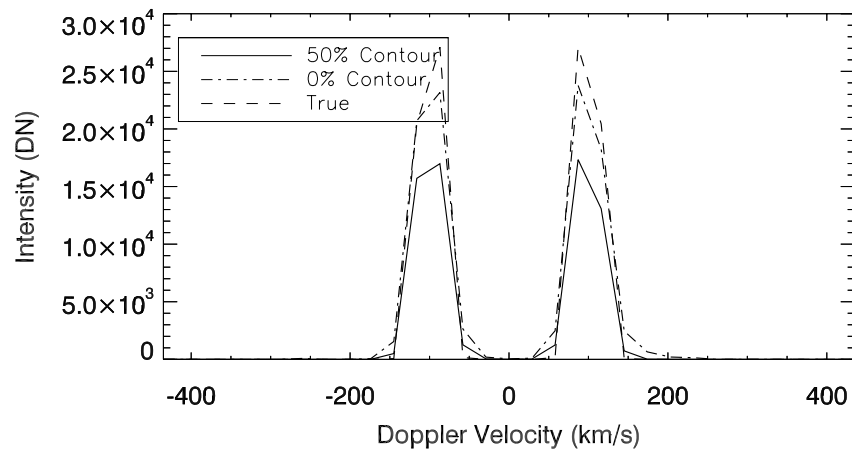


Figure 3.11: Inverted line profiles using the methods of section 3.6 calculated both within the 50% level and over the full inversion volume, over-plotted with the known synthetic spectrum.

Figures 3.12 and 3.13 show $x - \lambda$ and $y - \lambda$ slices of the reconstructed radiance through the jet center. The $x - \lambda$ slice shows that the spurious low speed peaks are now gone. The $y - \lambda$ slice shows that the south to north trending red-wards shift is gone as well.

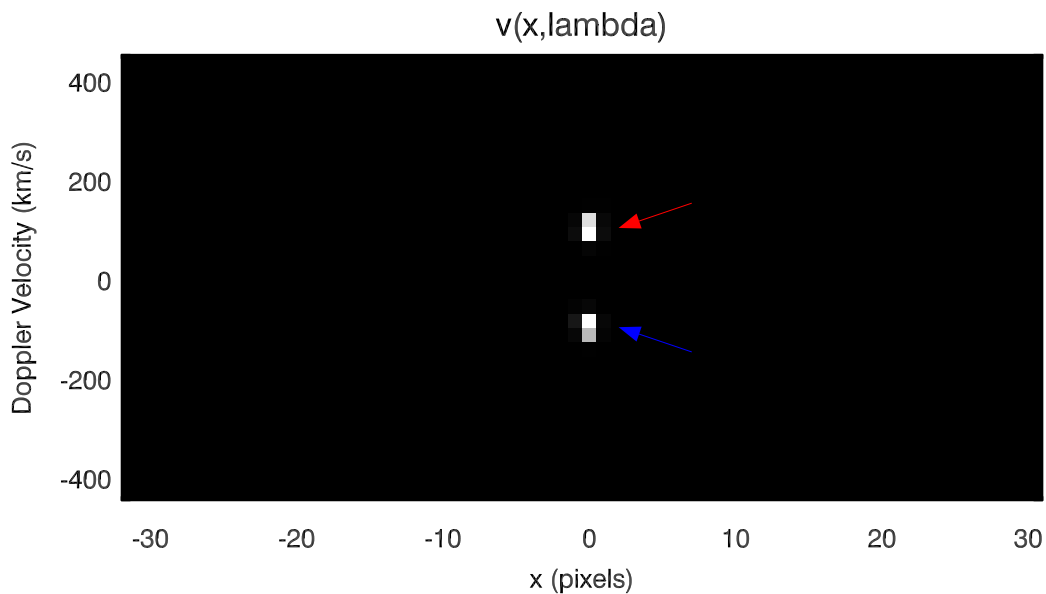


Figure 3.12: $x - \lambda$ slice through the jet center of $\nu(x, y, \lambda)$ recovered with the inversion method described in section 3.6.

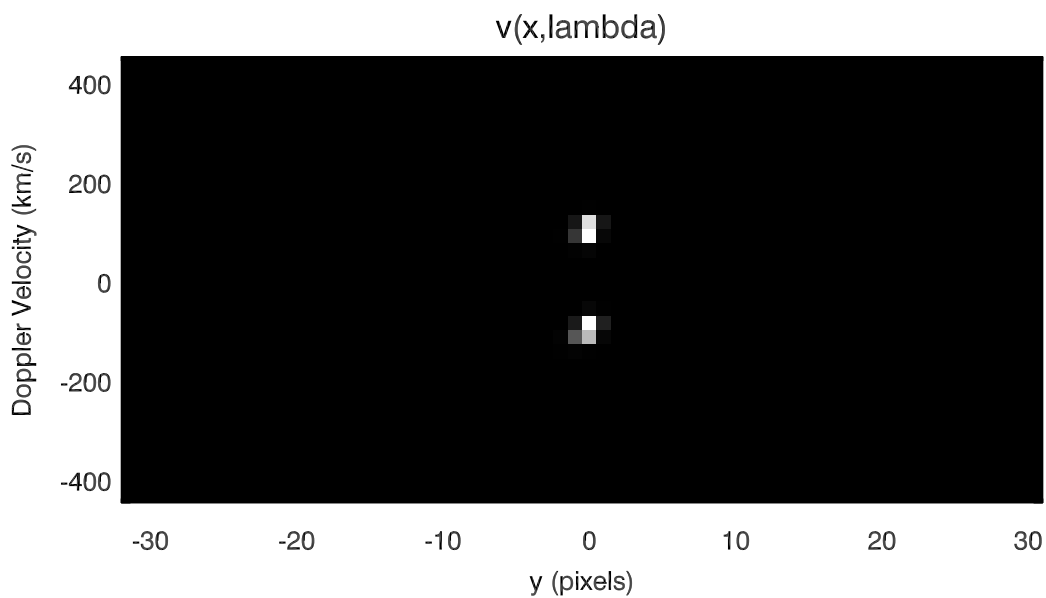


Figure 3.13: $y - \lambda$ slice through the jet center of $\nu(x, y, \lambda)$ recovered with the inversion method described in section 3.6.

Figure 3.14 shows profiles from the inversion results compared with the known profiles. As demonstrated in figure 3.10 the inverted \mathcal{I}_m have been deconvolved; so for comparison with the synthetic observations the inversion results must be convolved with the point spread functions. The purpose of figure 3.14 is to demonstrate that what is left behind after the inversion is mainly noise. There does not appear to be any signal left in the residuals and the detailed shape of the jet profile is well recovered. Also plotted in figure 3.14 are the profiles through the jet as recovered by partial reconstruction alone. The success of the methods presented in this section depend critically on the quality of the partial reconstruction results. This is because what is actually inverted with MART is the partial reconstruction results. As is clear from figure 3.14 the partial reconstruction results reproduce the known jet profiles and the inversion results reproduce the partial reconstruction results.

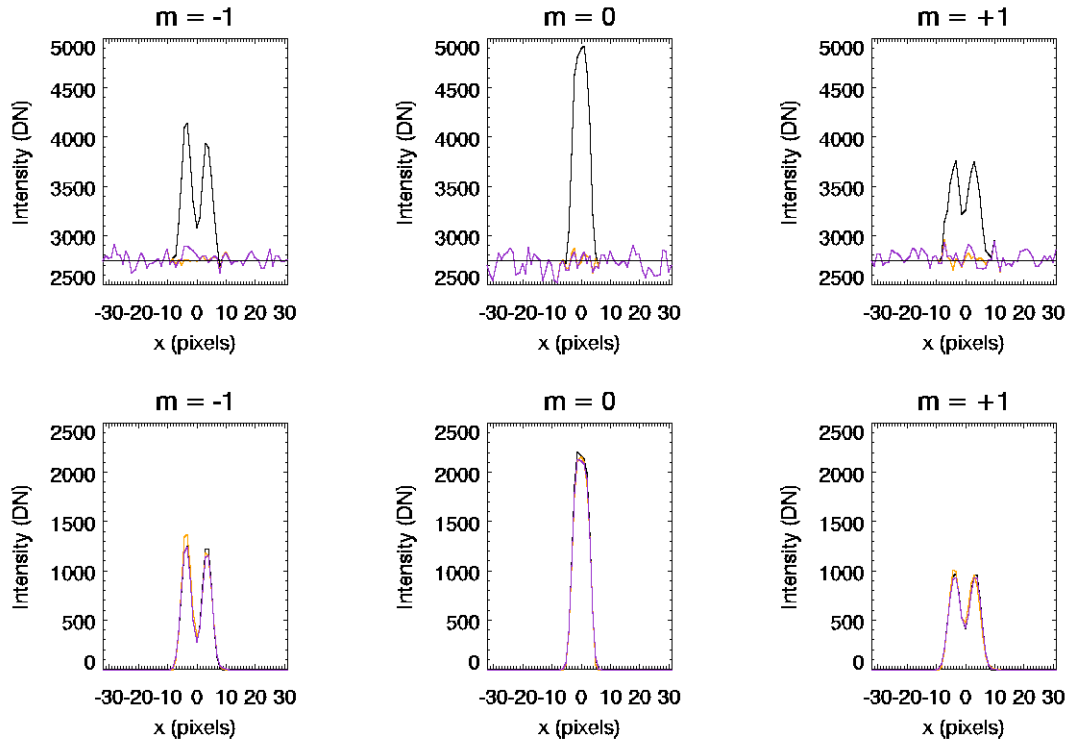


Figure 3.14: *Top row:* Profiles through the synthetic jet (black) plus background over-plotted with the residual after subtraction of the partial reconstruction results (orange) and the inversion results (purple). *Bottom row:* Profiles through the synthetic jet (black), the partial reconstruction results (orange) and inversion results (purple).

3.7 Conclusions

I have developed an inversion for the *MOSES-06* data and tested it on a synthetic observation of a bi-directional jet. The inversion is based on a multiplicative algebraic reconstruction technique. The inversion shows streak artifacts due to a limited number of projections in the *MOSES-06* data. When studying compact objects such as explosive events the streak artifacts can be removed by reconstructing the object from the background prior to inversion. This technique works well for isolated compact sources. Real data will have greater complexity than the synthetic observation used in this chapter, and difficulties are expected due to overlapping objects, extended objects, and sometimes low signal to noise ratios.

Artifacts also arise from different point spread functions in each of the *MOSES-06* channels. These different point spread functions result in differences in the intensity distributions of the \mathcal{I}_m that the inversion then interprets as spectral signatures. In particular, the classic astigmatic shapes of the \mathcal{I}_{-1} and \mathcal{I}_{+1} point spread functions leads to the appearance of a south to north trending red-wards shift in the inverted spectra. I have incorporated *MOSES-06* point spread functions into the inversion by combining MART with the Richardson-Lucy deconvolution algorithm. The inversion then consisted of using partial reconstruction to isolate the explosive event emission and then inverting the isolated event with MART plus deconvolution. This combined inversion is able to accurately reproduce the synthetic spectrum.

It should be pointed out that the inversion in this chapter was carried out under fairly ideal conditions. I assume an isolated emission source on a uniform background and perfect knowledge of the instrument point spread functions. It may not be surprising then that the inversion produces such excellent results. Random noise is present in the synthetic observation and the wavelet noise reduction technique has

acquitted itself well in separating out the noise during inversion. Increased data complexity and incomplete knowledge of the point spread functions are expected to present a greater challenges for the inversion. In the following chapter I apply the inversion to the *MOSES-06* data.

CHAPTER FOUR

INVERSION OF A BI-DIRECTIONAL JET IN *MOSES-06*

In this chapter I will invert the *MOSES-06* \mathcal{I}_m to obtain an estimate for the spectral radiance $\nu(x, y, z)$. In chapter 3 I developed an inversion method which successfully reproduced the known radiance of a synthetic bi-directional jet. The main steps of the inversion are described in sections 3.5 and 3.6. First an object for inversion is identified, e.g., any of the explosive events shown in figure 2.22. Next the intensity in the \mathcal{I}_m associated with the object is extracted from the background emission using the partial reconstruction from wavelet coefficients method. Finally the partial reconstruction results are inverted with the MART to yield an estimate for ν .

In order to illustrate the inversion method in the context of real data I have chosen to invert the bi-directional jet example discussed in chapter 2 (figure 2.11 bottom row). This event was selected because it was a well observed explosive event with an apparently simple structure. Furthermore the bi-directional jet structure is predicted by the model of Innes & Tóth (1999) and may be compared directly with the observations. In this model explosive events are the observable signature of Petschek reconnection in the transition region.

In section 4.1 I will describe the observations which are a time series of a *MOSES-06* bi-directional jet. For simplicity I will then detail the inversion of a single exposure. In section 4.2 I show the partial reconstruction of the jet. In section 4.3 I invert the partial reconstruction results with MART to obtain the radiance estimate ν . I analyze the inversion results with the main findings being that the bi-directional jet has negligible emission at low velocity and that the blue and red wings of the jet are

offset by approximately 500 km. A low velocity component exists which is spatially separate from the jet.

In section 4.4 I show the results of inverting the full time series. I show the time evolution of the jet speeds and light curves for all of the emission components. The blue jet shows a steady doppler speed of about 90 km s^{-1} while the red jet shows a curious variability. The light curves show the blue jet is consistently brighter than the red jet by a factor of two. I look at the time evolution of the spatial centroids of the emission components. The red and blue wings of the jet are spatially separate and move apart with time from 500 km at the beginning of the time series to 1500 km at the end, a total time lapse of approximately 60 s. The motion is most pronounced in the blue wing with an estimated average speed of 20 km s^{-1} . The centroid analysis confirms that the low velocity emission is spatially separate from the jet.

4.1 Data

The inversion target is the bi-directional jet from the bottom panel of figure 2.11. The inversion is applied to a sequence of 7 exposures covering the early phase to past the apparent peak brightness of the event. The exposure numbers are 12–18 (see table 2.2). The sequence begins at 18:48:10 UT and ends at 18:49:09 UT for a total of 59 s of observation. The exposure lengths are 3 s with about 6 s readout time giving a uniform 9 s cadence. The onset of the bi-directional occurs one or two exposures prior to the inverted sequence ($n = 10$ or $n = 11$). I did not invert these early exposures of the jet because of uncertainties due to low signal to noise. The rise phase of the jet in these early exposures is discussed qualitatively in section 2.4.2 and in the discussion of this chapter (section 4.5).

The event is located in quiet sun in the southeast quadrant of the disk centered at [-750", -130"] heliographic cartesian coordinates. The field of view for inversion is

64×64 pixels ($37.8''$ square). For convenience I work in pixel units in this chapter. The data were reduced as described in section 2.2. An example frame from the selected sequence ($n=15$ at 18:48:38 UT) is shown in figure 4.1. A movie of the bi-directional jet is shown in figure A.3.

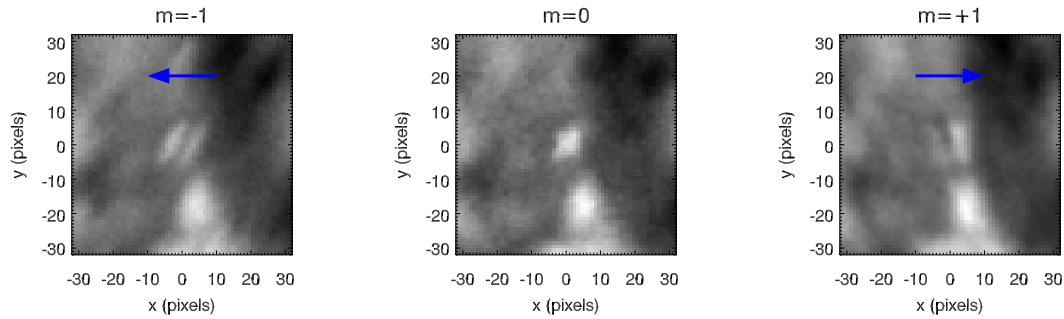


Figure 4.1: An example frame from a sequence of *MOSES-06* images of a bi-directional jet. Left to right: $m = -1$, $m = 0$, $m = +1$. Panels are 64×64 pixels, with angular sampling $0.59'' \text{ pixel}^{-1}$. Dispersion is $29 \text{ km s}^{-1} \text{ pixel}^{-1}$. Blue shift direction is indicated with arrows.

4.2 Partial Reconstruction of a Bi-directional Jet

In this section I apply the partial reconstruction method to the bi-directional jet images of figure 4.1. The images are from exposure number $n = 15$ taken between 18:48:38 and 18:48:41 UT. The partial reconstruction method is described in section 3.5. The goal is to separate the emission associated with the bi-directional jet from background emission. The jet as seen in the \mathcal{I}_m is a compact feature on a more slowly varying background. In wavelet space the jet coefficients are then distinct from the background coefficients. In the partial reconstruction method the wavelet coefficients belonging to the jet are first identified. An iterative method is then employed to generate an image whose wavelet coefficients are the same as those of the jet.

Recall that in section 3.5 I used a 3σ significance test (see section *B.2.1*) to find the synthetic jet coefficients. I use the same approach here but the data are more complex than the synthesized example. In some instances the jet coefficients blend with those of nearby image features. In these instances I used the **watershed** segmentation algorithm in *IDL* to separate the jet coefficients from adjacent objects. Figure 4.2 shows the wavelet transform of the \mathcal{I}_m up to scale $j = 3$. The coefficients used in the reconstruction are contained within the blue contours. From these wavelet images one can see that the bi-directional jet characteristics of this observation are most clearly seen in scale $j = 2$.

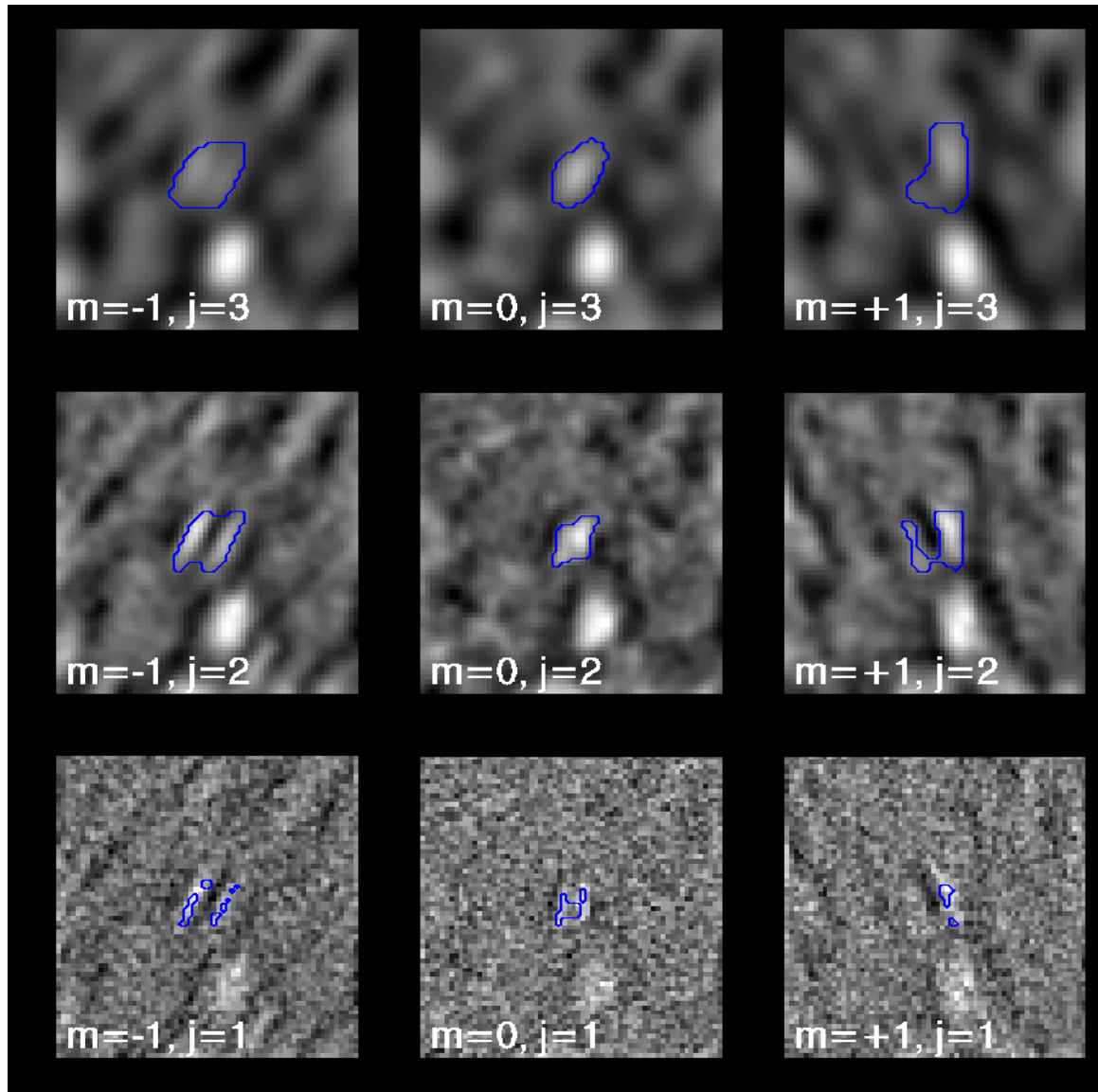


Figure 4.2: The wavelet coefficients of the \mathcal{I}_m from exposure $n = 15$. The figure shows coefficients up to scale $j = 3$. The over-plotted contours indicate the coefficients used in the partial reconstruction.

The panels of figure 4.3 show the partial reconstruction results. The total intensity of the reconstructed jet in each spectral order varies by less than 10% from the mean. The quality of the reconstructions can be seen in the residuals where no jet structure remains.

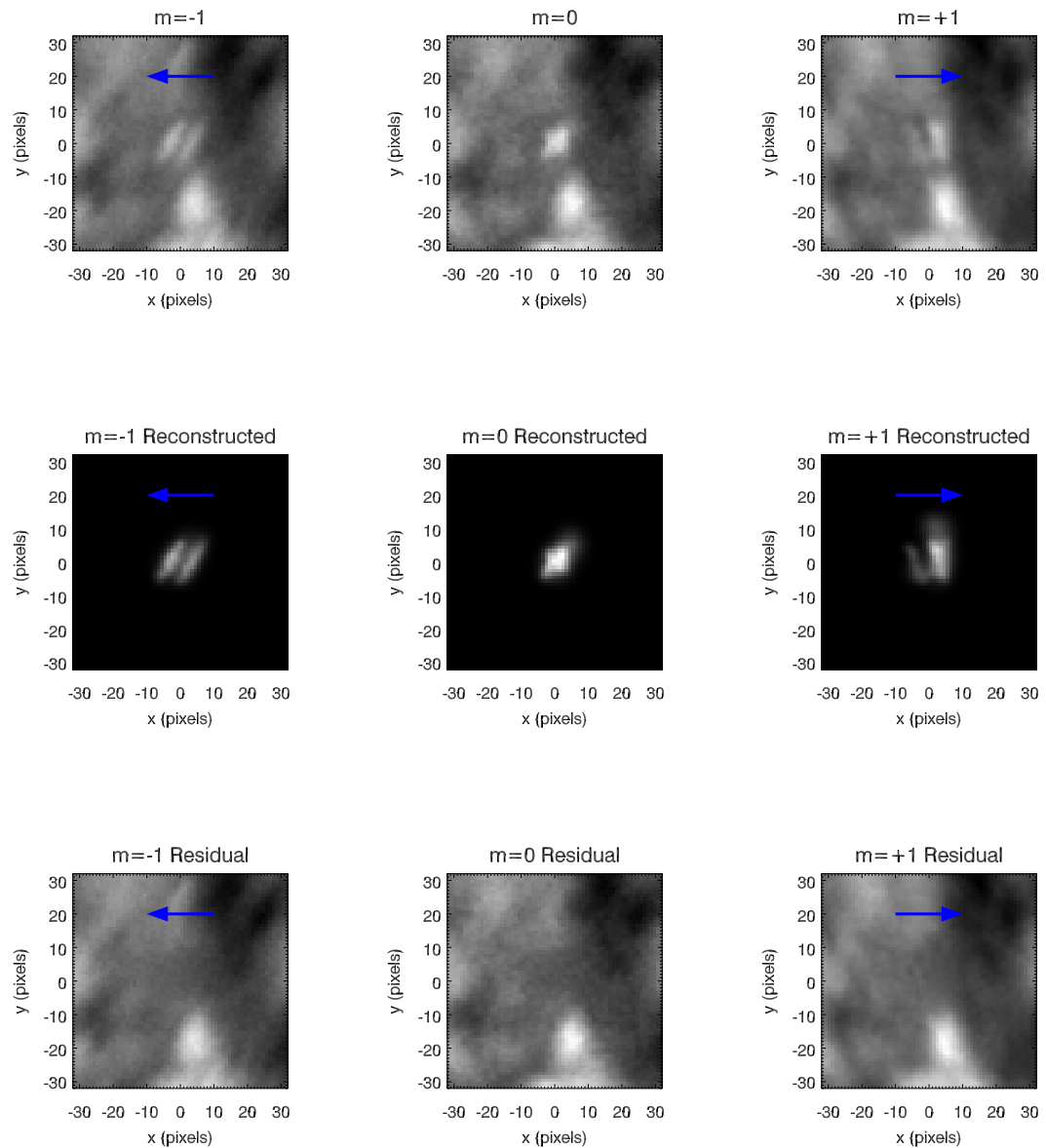


Figure 4.3: Partial reconstruction of a bi-directional jet observed with *MOSES-06*. From top to bottom the rows show the data, the reconstructions, and the residuals after subtracting the reconstructions from the data.

4.3 Inversion of a Single Frame

The three *MOSES-06* images (figure 4.1) were inverted with the methods described in section 3.6. The result of the inversion is a cube $\nu(x, y, \lambda)$ which approximates the spectral radiance of the jet in isolation. The inversion volume is 64×64 spatial pixels and 31λ pixels. The spatial sampling is $0.59''$ and the spectral sampling is $29 \text{ m}\text{\AA} \text{ pixel}^{-1}$ which corresponds to a doppler shift of 29 km s^{-1} per wavelength pixel.

The data cube ν can be visualized in many different ways. When ν is projected as in equation 1.3 the resulting images \mathcal{I}_m^ν are comparable to the \mathcal{I}_m (equation 1.2) but have been de-noised and de-convolved from the respective point spread functions (\mathcal{P}_m). For direct comparison with the observed \mathcal{I}_m the \mathcal{I}_m^ν have to be convolved with the \mathcal{P}_m .

The \mathcal{I}_0^ν image is displayed in the left panel of 4.4. Recall that as with \mathcal{I}_0 , the \mathcal{I}_0^ν image shows spatially where emission is present. The \mathcal{I}_0^ν image in figure 4.4 is shown in log scale in order to show the full spatial extent of the emission. In this example \mathcal{I}_0^ν is much more compact than the log scaled image suggests. The blue contour in the left panel of 4.4 indicates the 50% contour of peak \mathcal{I}_0^ν intensity. The green contour is a one pixel dilation of the blue contour. These contours enclose areas that account for most of the jet radiance. When viewed with linear scaling \mathcal{I}_0^ν appears very compact.

The inversion produces an estimate of the spectrum within each spatial pixel. This is the λ dimension of the radiance $\nu(x, y, \lambda)$. The right hand panel of 4.4 shows spectra obtained by spatially integrating ν . The black spectrum is integrated over the full spatial domain of the inversion. The blue and green spectra are integrated over the blue and green contours shown in the right hand panel. The black spectrum would under any circumstances be classified as an explosive event spectrum and consists of

fast ($\pm 90 \text{ km s}^{-1}$) jet components and a low velocity core that peaks at zero velocity. However the blue and green spectra clearly show the the fast jet components are confined to just a few pixels that corresponds to the brightest region in \mathcal{I}_0^ν . Within this jet region defined by the green contour there is almost no emission from low velocity plasma.

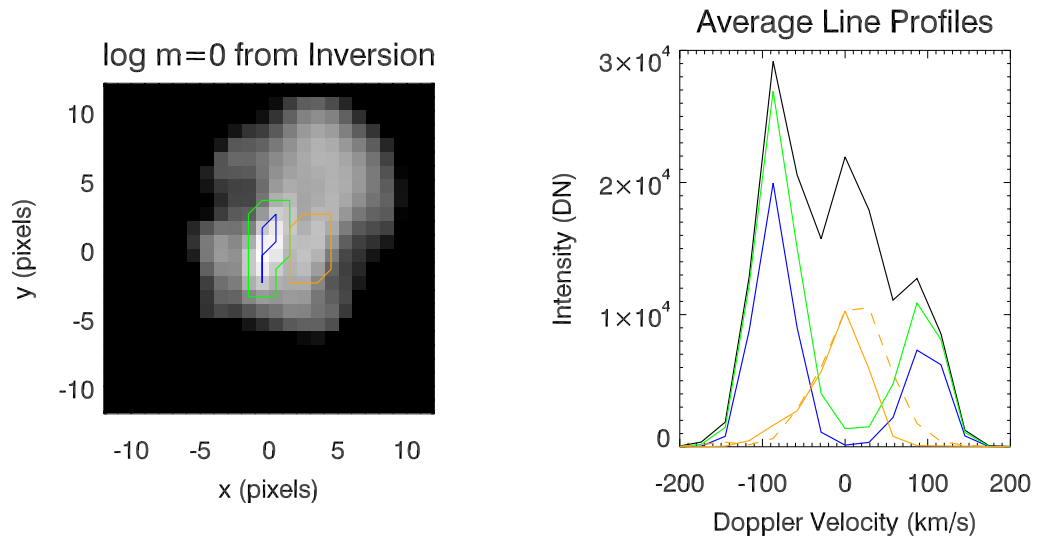


Figure 4.4: *Left:* Intensity image \mathcal{I}_0^ν obtained from inversion of the images in figure 4.1. The intensity image is over-plotted with contours showing the 50% peak intensity (blue), dilation of the 50% contour by one pixel (green), and the one pixel dilated 50% contour of $\nu(x, y, 0)$. *Right:* Plots of the spatial integral of the inverted ν over the contours shown in the left hand panel. The dotted orange line is the the balance of the total integrated emission after subtraction of the emission within the contours; it is low velocity and distributed faintly.

The low velocity plasma is spatially separated from the jet. The orange contour in the left hand panel of 4.4 is a one pixel dilation of the 50% intensity contour of $\nu(x, y, \lambda = 0)$. The integrated spectrum within the orange contour is shown as the solid orange curve in the right hand panel of 4.4. About half of the low velocity emission is contained within the orange contour. The remainder of the total integrated spectrum after subtraction of the emission within the orange and green contours is

also low velocity emission and is distributed more faintly over the remainder of the \mathcal{I}_0^ν image.

The spectra of the right hand panel of figure 4.4 show peaks at $\lambda = -3$, $\lambda = +3$ and $\lambda = 0$ in pixel units corresponding to doppler speeds of -87 , $+87$, and 0 km s^{-1} respectively. These wavelength bins will represent the blue wing, red wing, and low velocity components of the total emission. The spatial distribution of the emission in these wavelength bins is summarized in terms of the first two moments in table 4.1. The conversion from spatial pixels to horizontal distance on the solar surface is about $430 \text{ km pixel}^{-1}$.

Table 4.1: Moments of the spatial distribution of $\nu(x, y, -3)$ (blue wing), $\nu(x, y, +3)$ (red wing), and $\nu(x, y, 0)$ (low velocity component) of the inverted bi-directional jet (figure 4.1). Peak radiance is in relative units (DN). The spatial coordinates are given in km. The centroids denoted by $\langle * \rangle$ are given with respect to the center of the inversion spatial domain.

	Peak Radiance	$\langle x \rangle$	$\langle y \rangle$	RMS Radius
Blue Wing	4870	-104	140	615
Red Wing	3183	-197	-312	994
Low Velocity	1139	1055	647	1477

The spatial separation the blue and red wing emission relative to the low velocity emission is 1267 km and 1578 km respectively. These separations are in excess of the spatial (root mean square) widths of the blue and red wings (615 km and 994 km , respectively) and I conclude that the low velocity emission is spatially distinct from the bi-directional jet. There is also a separation of 462 km (about 1 pixel) between the blue and red components of the jet. This separation is smaller than the rms radius of either component so the wing separation is not well resolved spatially in the image data (i.e., \mathcal{I}_0^ν) .

I used gaussian fits to estimate the line shifts, widths, and total intensities of the

three emission components (red wing, blue wing, and low velocity emission). First the green spectrum (right hand panel figure 4.4) was fit with two gaussians to estimate the jet parameters. This fit was then subtracted off of the total spectrum (black) and this residual spectrum is fit with a single gaussian to estimate the low velocity parameters. The line shifts, widths, and relative integrated intensities are given in table 4.2.

Table 4.2: Line shifts, widths and percentage of the total intensity in each of the spectral components discussed in the text.

	Blue Wing	Red Wing	Low Velocity
Line Shift (km s^{-1})	-85	94	3
FWHM Line Width (km)	59	61	93
% of Integrated Intensity	36	16	44

For comparison the simple estimates for the line shifts obtained by fitting the \mathcal{I}_m intensity profiles (table 2.3 chapter 2) yielded average doppler shifts of -101 km s^{-1} and $+110 \text{ km s}^{-1}$ in the blue and red wings respectively. The % of integrated intensity indicates the total emission in each component relative to the total emission present in $\nu(x, y, \lambda)$. The jet is dominated by the blue component which has about twice the integrated intensity as the red component. Together, the jet components account for about half of the integrated intensity contained in ν , but they do so over an area that is only about 10% of the area where \mathcal{I}_0^ν is non-zero. The low velocity emission makes up a little less than half of the integrated intensity. As discussed above about half of the low velocity emission is contained in the orange contour (left hand panel figure 4.4).

In this section I have applied the inversion methods described in section 3.6 to reconstruct the radiance of an apparent bi-directional jet. The products of the inversion (the data cube $\nu(x, y, z)$) are exactly co-temporal spectra over a finite

field of view. Such a data product is not possible with slit spectroscopy and offers unprecedented opportunity for the study of dynamic events such as explosive events.

The inversion has confirmed the bi-directional jet nature of the observation in question (figure 4.1). The total inverted spectrum shows fast red and blue components and a low velocity component. The low velocity component is spatially separate from the jet. The blue and red components are not resolved in image data but moment analysis of the wings of the line profile show a spatial separation between the two jet components. In the following section I will revisit these findings in the context of the time evolution of the jet.

4.4 Time Evolution

I inverted the sequence of bi-directional jet observations from $n = 12$ to $n = 18$. All of the exposures had a similar character to the inversion described in section 4.3. Fast bi-directional jet emission is located within a small area enclosing the brightest emission in the inverted intensity image \mathcal{I}_0^ν (for example see the blue and green contours of figure 4.4). A low velocity component is spatially separate from the jet. I calculated the spatially integrated ν within the one pixel dilated 50% intensity contour for each exposure in the sequence. These spectra are the integrated spectral line profiles of the jet and are plotted in the left hand panel of figure 4.5. I then fit these spectra with two gaussian fits to find the mean doppler shift of each components. These shifts (magnitudes) are plotted in the right hand panel of 4.5 and are also indicated as red and blue curves in the left hand panel of the same figure.

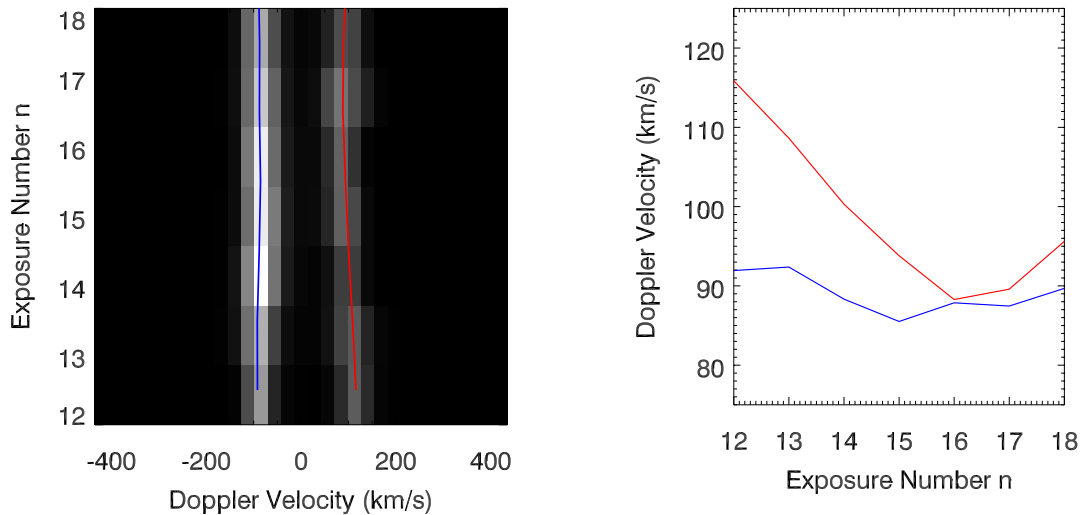


Figure 4.5: *Left:* Stack plot of the bi-directional jet spectra over-plotted with the centers of the blue and red components determined from gaussian fits. *Right:* Plots of the blue wing doppler speed (blue curve) and red wing doppler speed (red curve). Elapsed time between exposures is approximately 9 s.

The blue jet shows a steady velocity of approximately -90 km s^{-1} over the observation period. There is no indication of an early acceleration period that would indicate the jet accelerating up to the (presumed) Alfvén speed. The red jet shows a constant negative acceleration in the first 36 s of observation (first 5 exposures), reaching a minimum velocity of 90 km s^{-1} . In the final two exposures in the sequence the red jet shows positive acceleration.

The remainder of the emission contained in ν after subtraction of the jet components is peaked at $\lambda = 0$ and contains very little fast emission. I fit a gaussian to this low velocity component. Using the gaussian fits to all components I calculated the total intensity in each component and plotted the light curves in figure 4.6.

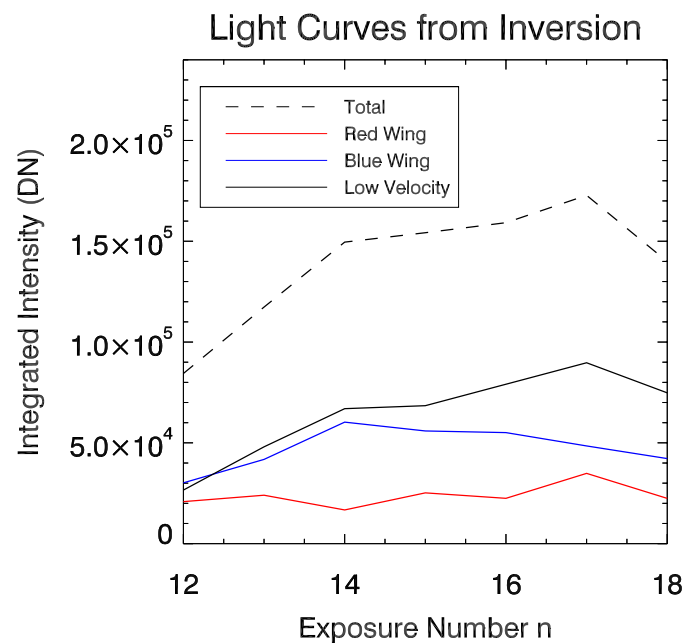


Figure 4.6: Light curves of the jet and low velocity emission components. The total line profile integrated over the whole spatial domain of the inversion is shown by the dotted line.

The blue to red ratio is about a factor of two on average but fluctuates over the observation period. The low velocity component contains more total intensity than either jet component but is much more diffuse. As seen in figure 4.5 the low velocity component does not influence the estimated jet spectrum because it is spatially separate from the jet.

To show the spatial relationship between the emitting components I calculated the centroids of $\nu(x, y, \lambda = -3)$, $\nu(x, y, \lambda = 0)$, and $\nu(x, y, \lambda = +3)$, with λ given in pixels. These are the centroids of the blue wing, low velocity component, and red wing, respectively. For comparison I also calculated the centroid of the \mathcal{I}_0^ν images. These centroids are plotted in figure 4.7.

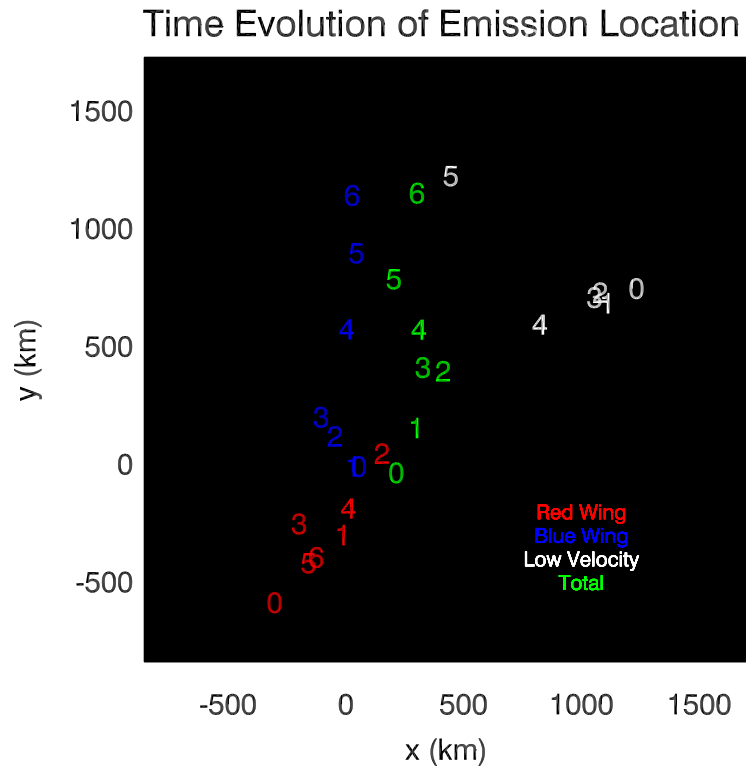


Figure 4.7: Time evolution of the spatial centroids of the emission in the blue wing (blue), red wing (red), line core (white) and \mathcal{I}_0^ν (green). The plotted numbers 0-6 correspond to exposure numbers $n = 12$ through $n = 18$. The numbers are plotted at the spatial coordinates of the respective centroid at the time of the exposure. Spatial coordinates are given in km with a conversion of about $425 \text{ km pixel}^{-1}$.

The most interesting aspect of this jet as seen in figure 4.7 is the northwards motion of the blue wing. This can be seen in the event movie (figure A.3) and is here quantified. The blue jet consistently moves north over the observation period, moving about 1200 km (3 pixels) north in 60 s for an average sky plane velocity of 20 km s^{-1} . The red component moves but does not clearly trend northwards. The net effect is that the jet components move apart, with maximal separation of about 1600 km. The \mathcal{I}_0^ν centroid (green) track with the blue jet component because it is stronger than the red component and the jet emission is located in the brightest region of \mathcal{I}_0^ν . The centroid plots show that the low velocity emission primarily exists well ($>1000 \text{ km}$) to the northwest of the jet emission.

4.5 Discussion

In this chapter I looked at the time evolution of an explosive event with bi-directional jet characteristics observed with the *MOSES-06*. The jet emission occurs in a small area ($1500 \times 3000 \text{ km}$) and contains no measurable low velocity emission. The blue wing is about twice as strong as the red wing. The wing velocities are approximately $\pm 90 \text{ km s}^{-1}$. Using the magnetic field strength from a photospheric field extrapolation and an assumed density the wing speeds are consistent with the expected Alfvén speed (see section 2.4.4). These characteristics are evidence in support of the Petschek magnetic reconnection model of Innes & Tóth (1999).

If the plasma traces reconnecting magnetic field lines then the expectation is that the wings should separate spatially (Dere et al., 1991). This separation was observed by Innes et al. (1997) in an explosive event observed with *SUMER* but has otherwise been unreported. The *MOSES-06* observations clearly show a separation of the blue and red wings of the jet with most of the systematic motion observed in the blue wing. The blue wing material moves up in the atmosphere into a less dense

environment while the red wing moves down into the denser lower atmosphere. This density differential may mean that the blue wing is more able to expand spatially.

Other aspects of the jet are either not predicted or in disagreement with existing reconnection models of explosive events. Innes et al. (2015) modeled tearing mode reconnection to explain low velocity emission often observed in explosive events. There is a low velocity component in the inverted *MOSES-06* line profiles but I have shown that they are spatially distinct from the jet; there is no line core emission in the jet. Ning et al. (2004) observed spatial offsets between the line core and (co-spatial) wings in explosive events observed in Si IV 1393 Å.

The nature of the low velocity emission is not clear at this point. Sometimes but not always explosive events have been associated with bright low velocity features known as blinkers (Bewsher et al., 2004). A blinker adjacent to the jet would explain the distinct low velocity component in the *MOSES-06* data. In any event the jet itself has no low velocity component and thus I conclude that the tearing mode instability does not occur in this event within the observation period.

Innes et al. (2015) show the time evolution of the tearing mode model. The onset of the event is characterized by an acceleration phase during which the wing emission accelerates to the Alfvén speed. This acceleration phase is followed by a phase that is like the steady state Petschek model of Innes & Tóth (1999) with fast jet components at the Alfvén speed and no core emission. I was unable to invert the data at the very first onset of the bi-directional jet described in this chapter due to low signal to noise. However the rise phase of the jet was discussed in section 2.4.2 and I was unable to find any evidence of this initial acceleration phase in the data. The time evolution of the blue jet speed shows no significant acceleration, an observation which supports the steady state Petschek model. The red component however shows a velocity change of about 25% of the mean speed in that wing (94 km s^{-1}) over the observation period.

This behavior is not predicted by either of the reconnection models cited above.

CHAPTER FIVE

OPTICAL TESTING AND INTEGRATION OF *MOSES-15*5.1 Optical Design

The *MOSES-15* spectrograph employs an off axis spherical grating (primary mirror) to form solar images in the $m = -1$, $m = 0$, and $m = +1$ spectral orders. These images are recorded on charge coupled devices (CCD) located at prime focus in each order. The optical path is split approximately in half by a flat secondary mirror. The off axis configuration is used so the secondary does not obscure the primary mirror. The *MOSES* instrument design is shown semi-schematically in figure 5.1.

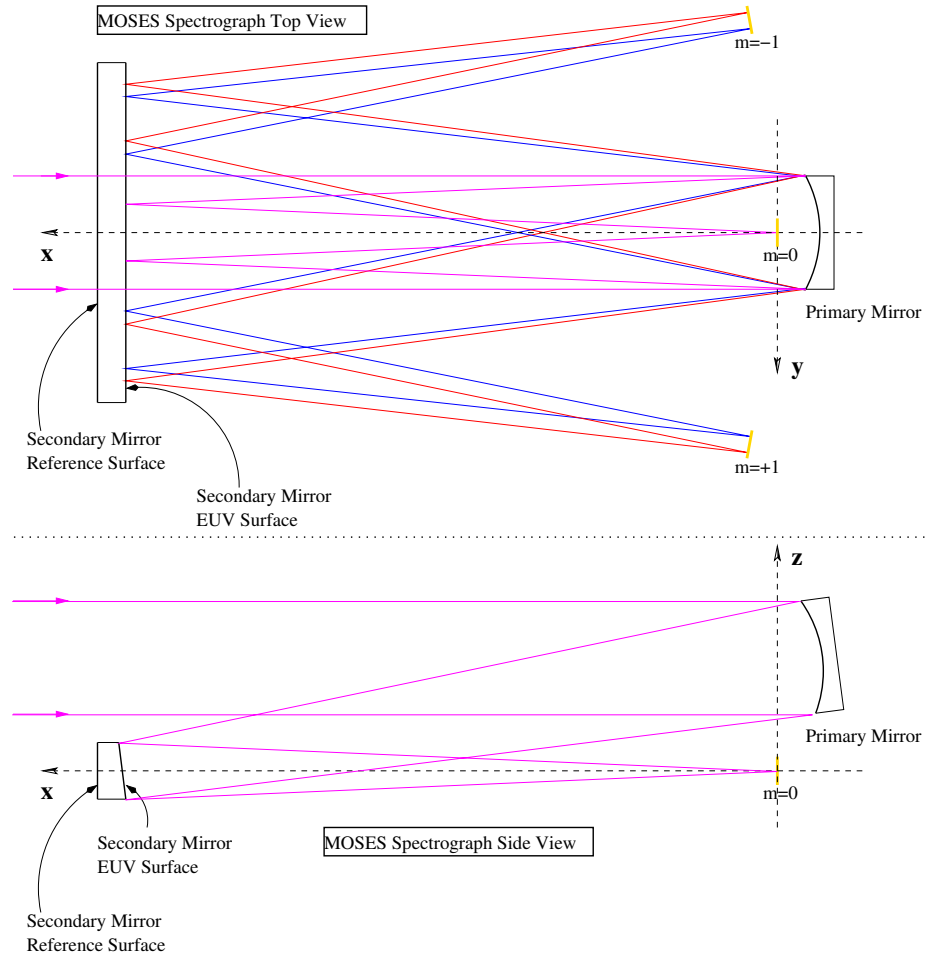


Figure 5.1: Schematic of the *MOSES* spectrograph and coordinate system.

MOSES-15 optical prescription is shown in table 5.1.

Item	X	Y	Z	Pitch	Yaw
Grating	118.7	0.0	78.5	-0.993	0.0
Secondary	2382.5	0.0	0.0	+0.993	0.0
Det(+1)	3.0	-136.7	0.0	-.011	-2.463
Det(0)	0.0	0.0	0.0	-.004	0.000
Det(-1)	3.0	+136.7	0.0	-.011	+2.463

Table 5.1: Optical prescription for the *MOSES-15* spectrograph. X, Y, and Z are in units of *mm*. The coordinate axes are depicted in figure 5.1. Pitch and yaw are right hand rotations about the *y* and *z* axes, respectively, and are given in degrees.

MOSES-15 primary mirror is a concave sphere with specified radius of curvature of 9295mm and is ruled (621 l/mm) only within a 60mm diameter circular area centered on the primary clear aperture. The profiles are optimized with intent to distribute incident light in *MOSES-15* passband equally to the $m = -1$ and $m = +1$ orders and nowhere else. The primary mirror clear aperture is an 80mm square, and balance of the aperture is not ruled, and thus puts light only in the $m = 0$ spectral order. The result is an approximately 25%, 50%, 25% distribution of intensity between the $m = -1$, $m = 0$, $m = +1$ orders respectively.

MOSES-15 secondary mirror is a monolithic flat mirror with clear aperture 189.8 mm \times 48.8 mm, wide enough in the dispersion direction to fold the optical path in all three spectral orders. The mirror substrate is wedge shaped when viewed from the side as in the lower panel of figure 5.1. The angled (right) facet is the multilayer coated surface. The vertical (left) hand facet of the wedge is coated for visible light reflection and is used as an alignment reference surface; therefore the wedge angle between the two surfaces must be accurately known. The specified wedge angle is

0.973 degrees.

The primary mirror surface and the EUV surface of the secondary mirror are coated with Si/Cr/Sc/Cr multilayers for 50 Åfwhm reflectance centered at 470 Å, peaking at about 0.3 (David Windt, priv. comm.).

5.1.1 Changes from *MOSES-06*

It was originally intended that changing *MOSES* observation wavelength would amount to changing coatings; the optical design would remain the same. Due to manufacturing limitations, however, the primary mirror design was changed significantly from the prior flight. The focal length was reduced by almost 100mm and the secondary mirror was moved closer to the primary to accommodate. A new secondary mirror mount had to be designed and fabricated for this purpose.

The specified grating pitch was not updated to reflect the change in focal length. The CCD positions in the y direction are effectively fixed. Moving the secondary towards the focal plane while keeping the diffraction angle fixed introduces an alignment offset of approximately 2.5mm, or about 10% of CCD width, between the dispersed orders and $m = 0$. This misalignment is corrected in software at a reasonable cost in reduced field of view.

Reducing the focal length calls for a change in pitch angle on the primary, or secondary, or both to maintain alignment. I chose to split the pitch change between the mirrors, reflected in the design table as an increase in grating and secondary pitch angle magnitude to 0.993 degrees from 0.973 degrees. The practical result is that there is a 0.02 degree offset in pitch between the secondary reference surface and the x axis that has to be accounted for in subsequent alignment (e.g. at the range).

5.2 Mirror Mounts

MOSES mirror mounts are mounted to a carbon fiber I-beam by way of threaded inserts embedded in the carbon fiber. The I-beam/insert structure is the Lockheed Optical Table System (LOTS). The threaded inserts are precisely located on a 4 inch grid with the mounting surfaces machined to be coplanar. Precision counterbores in the inserts accept shoulder screws for repeatable mount positioning. The I-beam and inserts thus form a precision optical bench, one capable of rocket flight. The grid axes and the normal to the mounting surfaces define *MOSES* coordinate axes. $+\hat{z}$ is normal to the insert mounting surfaces and $+\hat{x}$ points towards the sun. Angular coordinates of tip, tilt and roll are rotations about the y , z , and x axis, respectively.

MOSES alignment strategy relies on LOTS grid and precision machined mounts to position the spectrograph components within mechanical tolerance. Fine alignment and focus is completed with kinematic adjustments build into the mirror mounts. The mirrors are mounted such that each is constrained in six places, to exactly constrain the six positioning degrees of freedom: the three spatial coordinates plus tip, tilt, and roll.

The constraint is made by a hemispherical ball bearing magnetically connected to the end of a bolt which is threaded into the mirror mount. A hollow cone is machined into the bolt end to allow the spherical surface to seat; the flat surface of the hemisphere is in contact with the mirror. Magnetic connection allows the hemisphere to readily pivot on the bolt end in order to seat flush with the mirror. The mirror is pressed against each constraint with an opposing vlier screw threaded into the mount on the opposite side of the mirror.

The position of the mirror in the mount can be adjusted by changing the depth to which the constraint bolt is threaded into the mount. The depth of these bolts

are set by precision shims which sit between the mount and bolt head. Three constraints contact the face of each mirror in a tripod arrangement; these constrain the telescope angular alignment and focus. I had to make new shims for these constraint screws to optimize *MOSES-15* alignment and focus (chapter 7). The remaining three constraints – two on the bottom face and one on the side face of each mirror – control mirror position transverse to the optic axis, as well as the roll. I was able to reuse the *MOSES-06* shims on these constraint screws.

5.3 Testing Tools

A brief description of my two principal optical testing tools.

5.3.1 Theodolite

A theodolite is an imaging telescope with reticle eyepiece mounted for rotation in altitude and azimuth. The angular coordinates are precisely measured; angular measurements approach 1" accuracy. The theodolite is often used in autocollimation mode, with an illuminated reticle projected from the telescope, retroreflected from a flat mirror, and received again by the telescope, forming a reverse image of the reticle. When the two reticle images are aligned the theodolite is aligned to the mirror. I used a Leica Wild T-3000 theodolite for angular alignment measurements for *MOSES-15* optical testing.

5.3.2 Interferometer

I used a PhaseCam 6000 pixellated phase mask interferometer for nanometer precision measurements of optical surface figures in a poor vibration environment (second floor, clean room fans). The measurements are proportional to optical path differences between test and reference arms of the interferometer, caused by optical

surface imperfections or alignment issues. Interferometry data is often analyzed by fitting the data to sets of orthogonal polynomials. In the following I use and make reference to the Zernike polynomials (von F. Zernike, 1934).

CHAPTER SIX

MOSES-15 OPTICAL TESTING

This chapter describes optical testing of the *MOSES-15* primary and secondary mirrors.

6.1 *MOSES-15* Primary Mirror6.1.1 Radius of Curvature

The primary mirror radius of curvature determines the spectrograph focal length. The mirror mounts have limited focus adjustment, so it is important to accurately measure the radius of curvature. Nominal radius is 9.295 m. I used a tape measure, supported along its length, to measure the distance between primary mirror surface and center of curvature. The testing setup is shown in figure 6.1.



Figure 6.1: Test setup for measuring primary mirror radius of curvature.

I locate the center of curvature using an interferometer mounted with a diverging lens. The focal point of the diverging lens is coincident with the center of curvature of the primary when the Zernike defocus of the reflected wavefront is zero. I locate the diverger focal plane by translating a flat mirror along the optic axis near the focal plane until the Zernike defocus of the reflected wavefront is zeroed. The tape measure was run a few inches below the optical axis to avoid obscuration, and I use a height gage to vertically translate the "plane" of the primary mirror surface and diverger focal plane down to the tape, the difference in these measurements being the radius of curvature. The Zernike defocus between primary and interferometer suffered from noise probably due do vibration over the long measurement path. I improved the accuracy of the radius measurement by making several measurements in the neighborhood of correct radius, and fitting a line to the results. Measured radius is 9285 mm. Repeat radius suggest the error in this measurement is less than 5 mm.

6.1.2 Figure

Primary mirror figure measurement was done with a PhaseCam 6000 phase shifting interferometer. In principle the measurements obtained in section 6.1.1 are measurements of the grating figure, but they are low resolution due to $f/\#$ mismatch between the interferometer diverging lens and primary mirror operated at its center of curvature ($f/22$ and $f/120$, respectively), so I used the testing arrangement shown schematically in figure 6.2.

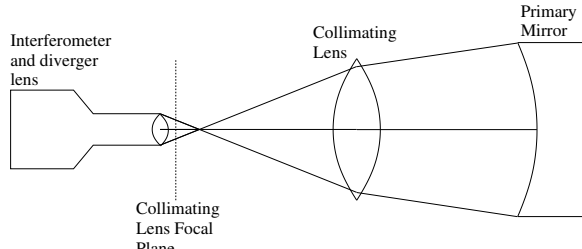


Figure 6.2: Test setup for measuring primary mirror surface figure.

The primary mirror figure measurements are corrupted by optical path length variation in the test setup. I contrived a reference measurement using the *MOSES-06* spare flight mirror. The *MOSES-15* mirror figure was out of specification, suffering from about 1.5 (46.5 nm) waves of astigmatism. The measured figure and Zernike fit is shown in the top row of figure 6.4.

6.1.3 Grating Figure Correction

The imaging characteristics of the primary mirror were expected to be poor, so we modified the primary mirror mount to accept vlier screws (spring loaded plungers, figure 6.3) and attempted to mechanically force the mirror to a better shape. With the primary mounted in the figure test configuration I experimented with different vlier screw positions and forces. I obtained significant reduction in the figure error using two screws. The measured primary mirror figure and Zernike fit following correction are shown in the bottom row of figure 6.4. The grating figure is analyzed in terms of expected instrument point spread functions in chapter 8.



Figure 6.3: Back plate of the primary mirror mount. The three threaded shafts are the vlier screws that push the primary against the tip/tilt/focus constraints. The grid of threaded holes accepts vlier screws to apply controlled forces to the back of the mirror in an effort to correct the distorted figure.

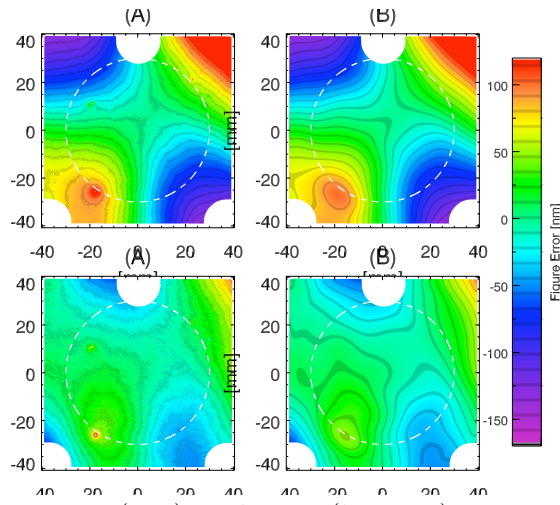


Figure 6.4: Left column: Pre (top) and post (bottom) correction measured primary figure error. Right column: 120 term Zernike polynomial fits, used to obtain a smooth representation of the data. The circular indents are obscuration by the tip/tilt/focus constraint screws. The central diffracting region of the mirror is visible in the measured figure as a 5 nm deep indent relative to the surrounding surface. The white dashed circle is a circular fit to points resulting from an edge finding exercise.

6.2 MOSES-15 Secondary Mirror

6.2.1 Wedge Angle

I did the wedge angle measurement using a single theodolite and a precision corner cube. The testing setup is shown in figure 6.5. A theodolite in autocollimation mode is alternately aligned to the multilayer surface, then the reference surface by way of the corner cube. The wedge angle is the difference between these measurements. The secondary was mounted to permit translation into and out of the page, which I used to measure wedge angle variation at different locations along the mirror. Measured average wedge angle is 0.9738 degrees (0.973 degrees specified). Eight measurements at different locations along the y (dispersion) dimension of the mirror yields standard deviation about this value of 0.0002 degrees.

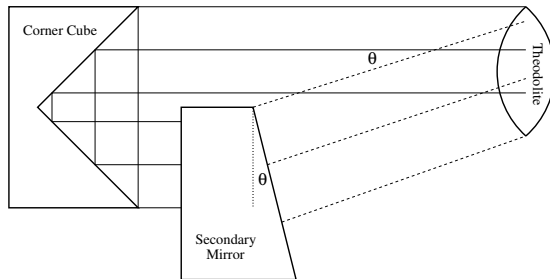


Figure 6.5: Test setup for measuring secondary wedge angle.

6.2.2 Figure

I measured the surface figure error of *MOSES-15* secondary mirror verified specification on aperture alignment, slope error and mid-scale roughness. The surface normals of the left and right sub-apertures are parallel with that of the center sub-aperture to within a fraction of an arc second, well within the specified 5 arc seconds. Measured slope error is $1.38 \mu\text{rad}$ RMS, less than the specified $1.9 \mu\text{rad}$

RMS. Midscale roughness measures 0.71 nm RMS, less than the specification of 1.1 nm RMS.

Given the size of the secondary mirror I used a beam expander that allowed me to get the short dimension of the secondary within the interferometer field of view. The raw measurements of the secondary are dominated by systematic errors in the interferometer/beam expander system, and a reference image was required to see the true surface. I have a $\lambda/100$ flat mirror F_R of sufficient reference quality, but its diameter is smaller than the smallest dimension of the secondary.

I made a reference image by translating F_R and making overlapping measurements of the reference surface across the interferometer field of view. I stitched the measurements together by optimizing the tip, tilt, and defocus of the reference measurements to minimize the mean absolute deviation in the overlap regions. Figure 6.6 shows the reference image measured thus, which is stitched together from 6 separate measurements.

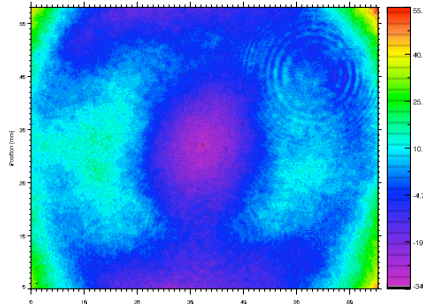


Figure 6.6: Measured interferometer reference, stitched together from 6 partial measurements of the beam. Area is 65.3 mm \times 53.0 mm. WFE is 10.7 nm RMS and 89.7 nm PV.

I measured the secondary in segments by translating the mirror across the interferometer beam. Each segment was reference subtracted and then stitched

together like the reference image. The measured surface figure error of the secondary mirror is shown in figure 6.7.

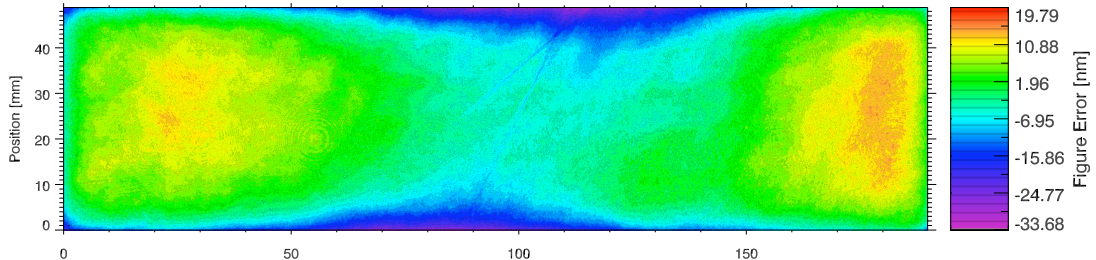


Figure 6.7: Measured secondary mirror figure error composed of 7 measurements of overlapping segments of the mirror. Total area is 189.8 mm × 48.8 mm with image pixel resolution 73 μm . An imperfection in the stitching process can be seen around $x = 22$ mm. Tip and tilt have been subtracted.

Secondary mirror figure results are summarized in table 6.1.

MOSES-15 Secondary Mirror Test Results		
Spec Description	Specification	Measured
Left Aperture Alignment	< 5"	.03"
Right Aperture Alignment	< 5"	.07"
Slope Error	< 1.9 μrad RMS	1.38 μrad
Midscale Roughness	< 1.1 nm RMS	0.71 nm

Table 6.1: Summary of test results for *MOSES-15* secondary mirror.

CHAPTER SEVEN

MOSES-15 ALIGNMENT AND FOCUS

The critical mirror angular alignments, focus, and grating roll are described in this chapter. The optical prescription for *MOSES-15* is given in table 5.1. Alignment and focus were done without working CCDs due to failure of the *MOSES-15* command and data handling system, which was not repaired until after alignment was complete. The focus method described here is expected to be significantly more accurate than the method used prior. Improvement of spectrograph focus was noted as a major goal for the second flight in the *MOSES-06* final report.

Spectrograph alignment in the dispersed orders depends on wavelength. The available alignment tools use visible wavelengths, so it is not possible to directly align the instrument in these orders. For the first flight, the system was aligned in the $m = 0$ order, and the $m = -1$ and $m = +1$ CCDs were then positioned relative to the $m = 0$ CCD according to the optical design, and the flight data show good relative focus (see appendix D). Reducing the primary mirror focal length does not significantly change the relative focal lengths (chapter 8), so I leave the CCDs fixed and optimize focus in $m = 0$ by changing the mirror separation.

Conceptually, alignment and focus is achieved in three steps:

1. Measure the alignment and focus state of the system from a known baseline (*MOSES-15* mirrors mounted with *MOSES-06* shims).
2. Measure the change in alignment with change in shim length.
3. Calculate new shim lengths, fabricate and install new shims, verify alignment and focus.

Alignment measurements are described in section §7.1. Focus measurement is described in §7.2.

7.1 Alignment

The coordinates in table 5.1 are referenced to LOTS axes. Two main alignment steps are required:

1. Align secondary mirror to LOTS
2. Align primary so rays parallel to \hat{x} pass through the center of the $m = 0$ CCD.

7.1.1 Secondary to LOTS

The *MOSES-15* spectrograph alignment is referenced to the secondary mirror alignment surface. The mount design is referenced to LOTS inserts. Therefore the secondary alignment surface has to be aligned to LOTS.

LOTS axes are measured with the tool shown in figure 7.1. The tool consists of a $2'' \times 4'' \times 6''$ setup block with $0.2''$ gage blocks epoxied onto three of the $2''$ tall sides. Setup blocks are manufactured for precise squareness and parallelism of adjacent and opposite faces, respectively. Gage blocks have highly parallel faces. Parallelism of the gage block faces with the setup block face is maintained by interposing three $3/16''$ gage balls between gage block face and setup block face. Epoxy fastens gage block to gage ball and gage ball to setup block.

Recall from section 5.2 that the LOTS has a grid ($4''$ center to center spacing) of threaded inserts with precision counterbores. The faces of the inserts are machined to be co-planar with normal vectors parallel to \hat{z} . Plug gages¹ are inserted into adjacent (along \hat{x}) inserts. The setup block is pressed against the plugs which aligns the block

¹Class Zz Plus 0.281"

in the $x - y$ plane (yaw). The setup block rests on four inserts which constrains the block pitch and roll angles (see figure 7.1). Once the setup block is placed as just described the setup block faces are normal to the LOTS axes. The gage blocks affixed to the setup block provide theodolite alignment surfaces. A theodolite aligned to the foremost gage block in figure 7.1 is looking parallel to $-\hat{x}$. Aligning a temporary reference mirror (e.g. upper left) then frees up the theodolite.

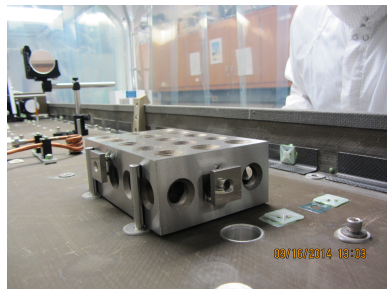


Figure 7.1: Alignment tool used to reference LOTS axes.

Once \hat{x} is established I install the secondary mirror and measure the angular misalignment. Secondary mirror alignment is controlled by the tripod of constraint screws on the EUV surface. I had to calibrate the change in alignment to the change in shim length. I did this by using gage blocks as shims on each constraint screw in turn, measuring alignment change as I varied the gage block thickness in 0.001" increments. Now I can calculate the *relative* change in shim length required to align the secondary, but I can't calculate the absolute shim length until after I measure system focus. To proceed with alignment I temporarily align the secondary by slightly loosening one or more of the constraint screws.

7.1.2 Primary to Filter Tube Target

With the secondary aligned, the primary mirror must be aligned so that rays parallel to \hat{x} are focused to the center of the $m = 0$ CCD. With the cameras inoperable

I used a proxy for this alignment: a target engraved in an aluminum disc mounted to the end of the $m = 0$ order filter tube, shown in figure 7.2.

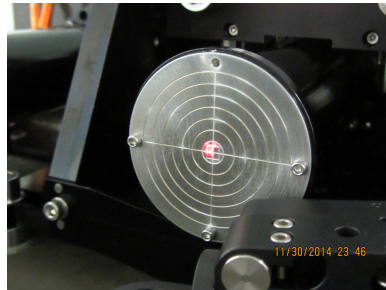


Figure 7.2: Filter tube alignment target. The central square is 3.63 mm on a side which corresponds to the width of the converging (square) beam at $x=211.01$ mm (the target x location). The crosshairs are parallel to y and z . The circles have radii of integer multiples of 3 mm, corresponding to about 2.3' of misalignment, or a little under 10% of the field of view in the long y direction.

I set up the theodolite so it is aligned along $-\hat{x}$ looking into the primary mirror and adjust the theodolite focus until the filter tube target is sharp. Angular misalignment of the primary is the angular difference relative to the target center, measured with the theodolite. As with the secondary mirror, the primary mirror pointing is controlled by the tripod of constraint screws on the EUV surface, and again I had to calibrate the change in shim length to the change in angular alignment. I did this in a similar fashion to the secondary angular alignment calibration, this time using 0.001" shim washers, as the 0.5" constraint screws do not accept gage blocks. This completes the required angular alignment measurements.

7.2 Focus

The shims which control angular alignment also determine the \mathbf{x} location of the mirrors and thus spectrograph focus. Therefore system focus state must be known before the shim lengths can be adjusted properly.

Proper focus results in the smallest size spot on the CCD. Traditional focus methods rely on through focus spot size measurements where the optical path is changed and the resulting spot size is measured. The cameras were not operable so I came up with a different focus method shown in figure 7.3.

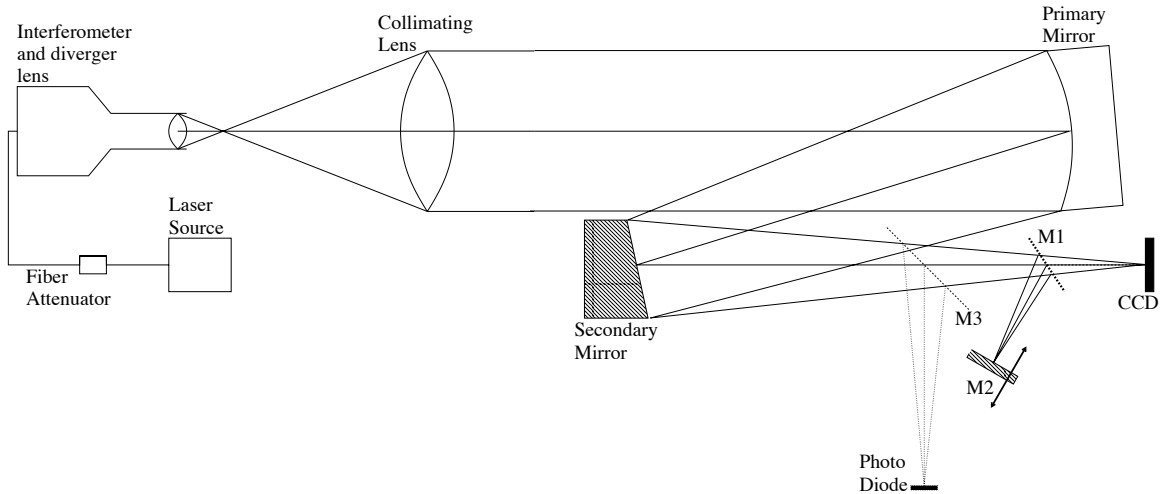


Figure 7.3: Test setup for focus. The initial wavefront defocus is precisely zeroed using a high quality flat mirror.

I use an interferometer to measure the curvature in an initially flat wavefront passed through the spectrograph and retro reflected by the CCD back to the interferometer. The Zernike defocus of the reflected wavefront is directly proportional to required change in shim length to achieve best focus. I calibrated the measurements by redirecting (with flat mirror M1) the converging beam to a flat mirror (M2) which is used to measure the wavefront Zernike defocus as M2 is precisely translated through the focus of the converging beam. This serves the same function as translating the CCD but is significantly easier and carries less risk for the sensitive camera system. The location of the measured spectrograph defocus on the calibration curve determines the required change in shim length to achieve focus. Figure 7.4 shows the results of the focus measurement, using the *MOSES-06* shims as a baseline to focus

the *MOSES-15* optics.

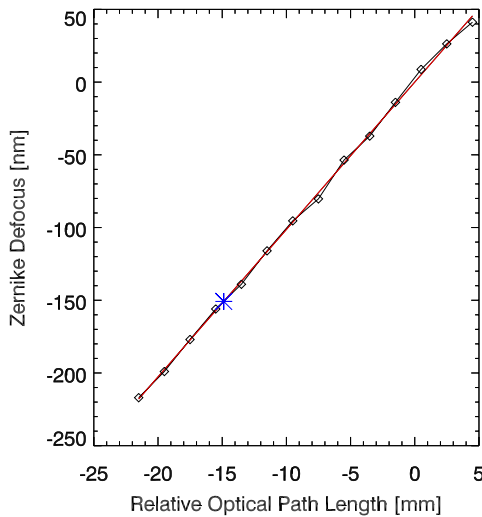


Figure 7.4: Points show measured Zernike defocus as mirror M2 is translated perpendicular to the optic axis (redirected by M1). Over-plotted red line is a linear fit. Asterisk at $x=-15$ shows the measured value of the Zernike defocus in the actual spectrograph. This result shows that the optical path length has to be increased by 15 mm. This focus curve is far more sensitive than, e.g. measuring visible light root mean square spot size for focus determination.

7.3 Image Quality Results

Alignment and focus were completed prior to repairs to *MOSES-15* flight computer, hence the cameras were inoperable. The first true images taken with the *MOSES-15* spectrograph were taken using the big collimator at White Sands Missile Range during our launch campaign. A sample image of a resolution test target is shown in figure 7.5. Pre and post flight visible light point spread functions were also measured at MSU, these are shown in the following chapter.

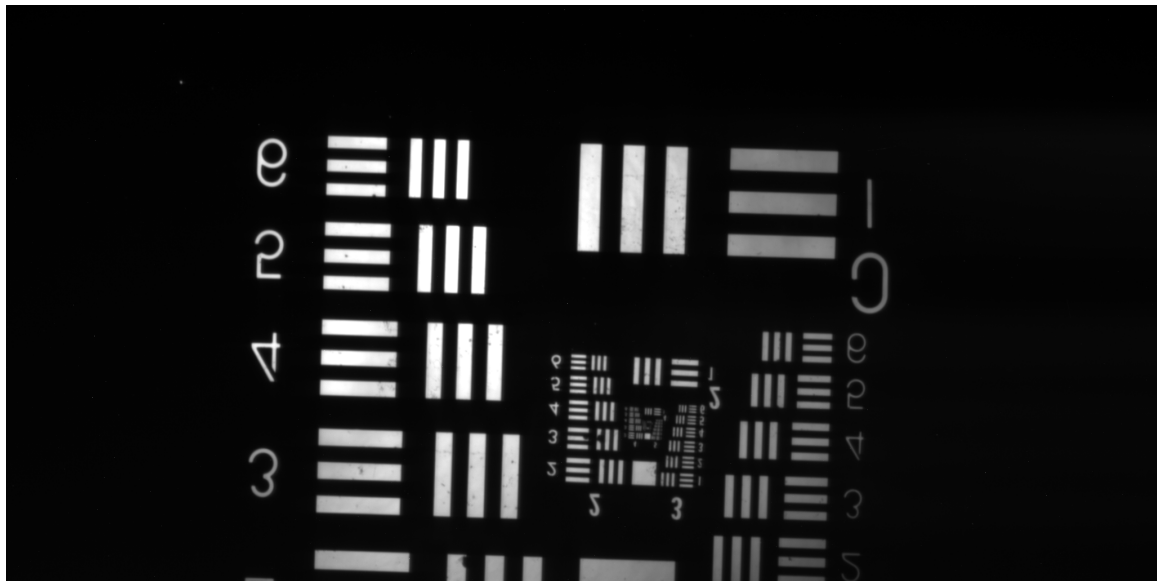


Figure 7.5: Air force resolution target of the aligned and focused *MOSES-15* spectrograph. Visible light, $m = 0$ spectral order.

7.4 Grating Roll Measurement

I verified that the grating roll angle put the dispersion in the $x - y$ plane by direct measurement. With a laser beam aligned to the optic axis, I used the LOTS alignment tool to align a stage (figure 7.6) to translate a CMOS camera parallel to the y axis and precisely measured the height (z) of the diffracted beam in the $m = -1$ and $m = +1$ orders. The results (figure 7.7) show the dispersion plane is effectively parallel to the $x - y$ plane, as intended.

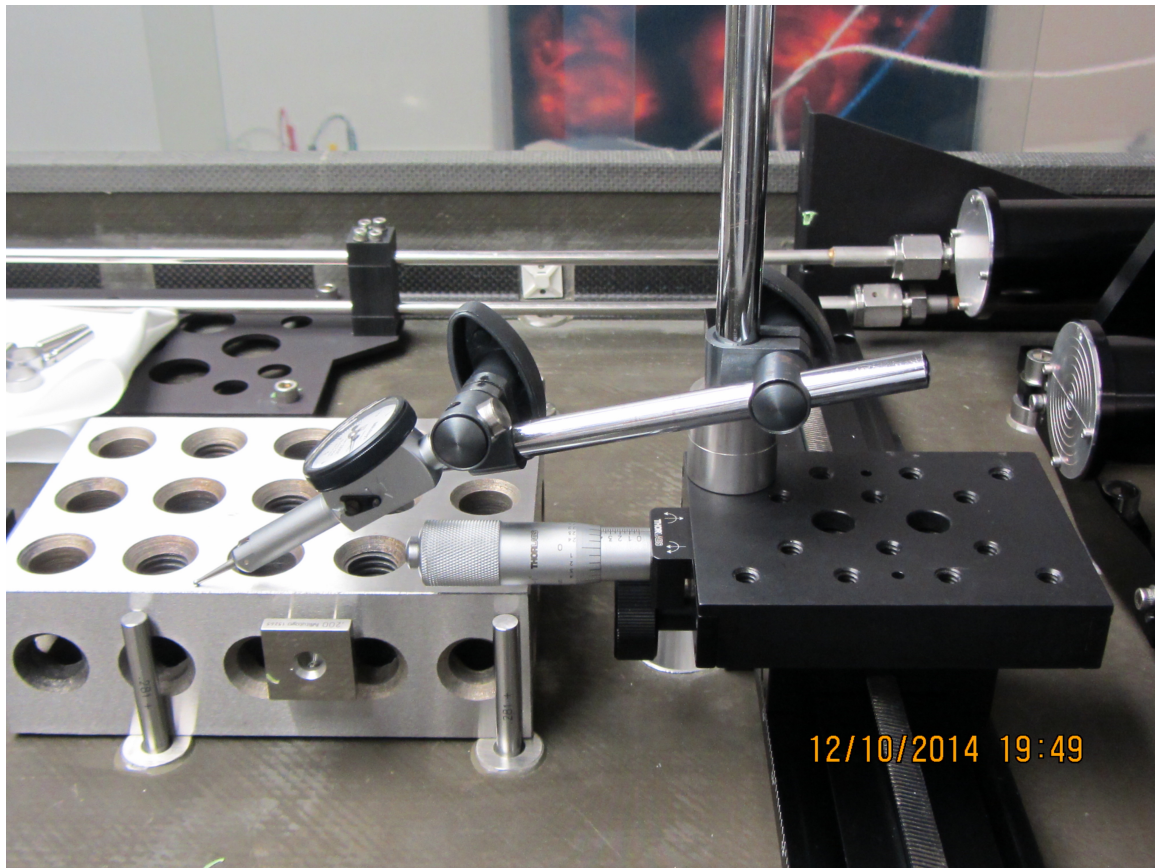


Figure 7.6: Alignment of translation stage for grating roll measurement.

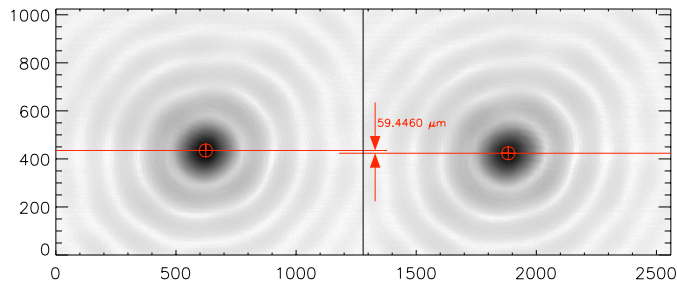


Figure 7.7: The figure shows images of a laser beam after diffraction from the grating in the $m = -1$ and $m = +1$ spectral orders. The camera was mounted to translate parallel to the y axis. The vertical difference in the spot image centroid in the two orders is practically zero, indicating good roll alignment of the primary mirror.

CHAPTER EIGHT

OPTICAL MODELING

In this chapter I use a use a Fourier optics model to estimate optical performance of the *MOSES* spectrograph.

8.1 Fourier Optics Model

The electric field distribution near *MOSES* ideal focal plane due to a distant source of illumination is modeled as

$$E(\vec{f} + \vec{\delta}) = \iint E_0(y', z') e^{ik(|\vec{f} - \vec{r}| - \frac{m\lambda y'}{d})} e^{-i2\pi(\frac{\delta_y}{\lambda_f} y' + \frac{\delta_z}{\lambda_f} z')} dy' dz' \quad (8.1)$$

Here, $\vec{f} = (y, z, x)$ is the nominal focal point, $\vec{\delta} = (\delta_y, \delta_z, \delta_x)$ is a small displacement perpendicular to \vec{f} , $\vec{r} = (y', z', x'(y', z'))$ is the position vector on the surface of the grating, m is the diffraction order, and d is the grating pitch. The constraint $\vec{f} \cdot \vec{\delta} = 0$ confines the solution to a plane perpendicular to the axis of the rays converging on the focal point. Physically this constraint models a planar detector (e.g., a CCD). The grating rulings are modeled a phase contribution which is linear along the dispersion direction. $E_0(y', z')$ is the incident electric field evaluated on the mirror surface, which for a unit amplitude plane wave is given by

$$E_0 = e^{i\vec{k} \cdot \vec{r}} \quad (8.2)$$

where \vec{k} is the incident wave vector.

The integral on the right of 8.1 is a function of spatial frequencies $(v, w) = \left(\frac{\delta_y}{\lambda_f}, \frac{\delta_z}{\lambda_f}\right)$ whose sampling interval and range are given by the usual sampling

considerations, i.e.,

$$\delta v = \frac{1}{\Delta y'} , \quad \Delta v = \frac{1}{\delta y'} \quad (8.3)$$

Given $\delta y', \Delta y', \delta z', \Delta z'$ as the sampling interval and range in the aperture plane the sampling interval and range in the focal plane are therefore given by

$$\delta \delta_y = \frac{\lambda f}{\Delta y'} , \quad \Delta \delta_y = \frac{\lambda f}{\delta y'} \quad (8.4)$$

$$\delta \delta_z = \frac{\lambda f}{\Delta z'} , \quad \Delta \delta_z = \frac{\lambda f}{\delta z'} \quad (8.5)$$

δ_x is given by the condition that $\vec{\delta} \cdot \vec{f} = 0$.

The diffraction code consists of the following steps:

- Define grating parameters, and grating and secondary positions and orientations.
- Define incident light wavevector based on input incidence angles (altitude and azimuth).
- Define grid of grating coordinates based on input desired number of points and maximum range of aperture coordinates.
- Estimate nominal focus position \vec{f} .
- Use optimization procedure to minimize the phase term under the integral in the diffraction formula as a function of \vec{f} , using the guess from the previous step as a starting point.
- Repeat steps 2-5 for several incident light directions spanning a 20' (azimuth) by 10' (altitude) field of view, and for each of the three spectral orders $m = -1, 0, 1$.

- Fold the calculated \vec{f} vectors via the secondary mirror.
- Subtract off the vector \vec{f}_0 , the (folded) position vector of the best focus for on axis illumination in the zero order. This step shifts the coordinate system origin to the center of the m=0 order detector.
- For each of the three spectral orders, fit a plane to the best focus positions. These planes give the detector positions and orientations.

8.2 Results – Optical Prescriptions

I tested the code by first modeling the *MOSES-06* spectrograph and comparing the results (table 8.1) with the *MOSES-06* optical prescription (Fox, 2011). The Fourier model results are almost identical.

<i>MOSES-06</i> Design Table from Fourier Optics Model					
Item	X	Y	Z	Pitch	Yaw
Grating	118.8	0.0	78.5	-0.973	0.0
Secondary	2428.7	0.0	0.0	+0.973	0.0
Det(+1)	3.0	-136.9	0.0	-.003	-2.480
Det(0)	0.0	0.0	0.0	-.001	0.000
Det(-1)	3.0	+136.9	0.0	-.003	+2.478

Table 8.1: *MOSES-06* design table from Fourier optics model, using grating and secondary position and orientation from Fox (2011). Grating radius of curvature is 9.48 m and grating pitch is 950 l/mm. Angles given are in degrees, and positions in mm.

I modeled *MOSES-15* with the secondary moved towards the detectors to accommodate the reduced focal length of the grating, and the grating and secondary

tips optimized to center the detectors at $z=0$. Table 8.2 shows the resulting optical design table. The outboard detectors are required to move in (towards $m = 0$) by about 2.7 mm or a loss of 10% of the usable field of view will result. The tip of the secondary should not present any extra difficulty in the optical alignment.

MOSES-15 Design Table

Item	X	Y	Z	Pitch	Yaw
Grating	118.8	0.0	78.5	-0.993	0.0
Secondary	2382.5	0.0	0.0	+0.993	0.0
Det(+1)	2.9	-134.2	0.0	.005	-2.478
Det(0)	0.0	0.0	0.0	-.001	0.000
Det(-1)	2.9	+134.2	0.0	.000	+2.477

Table 8.2: *MOSES-15* design table from Fourier optics model after moving secondary towards detectors to compensate for change in grating focal length, and adjusting the tip of the grating and secondary equally to center the detectors at $z=0$. Grating radius of curvature is 9.295 m and grating pitch is 621 1/mm. Angles given are in degrees, and positions in mm.

8.3 Point Spread Functions

8.3.1 EUV, Modeled

I used the model to estimate point spread functions at operating wavelength across the field of view in each spectral order. I have shown the model results from *MOSES-06* (figure 8.1) and *MOSES-15* (figure 8.2) to show how the change the grating changes the expected instrument point spread functions. Limiting the aperture in the dispersed orders tightens up the point spread functions; conversely, the central order point spread function is expected to get a little worse as the aperture in that order is limited.

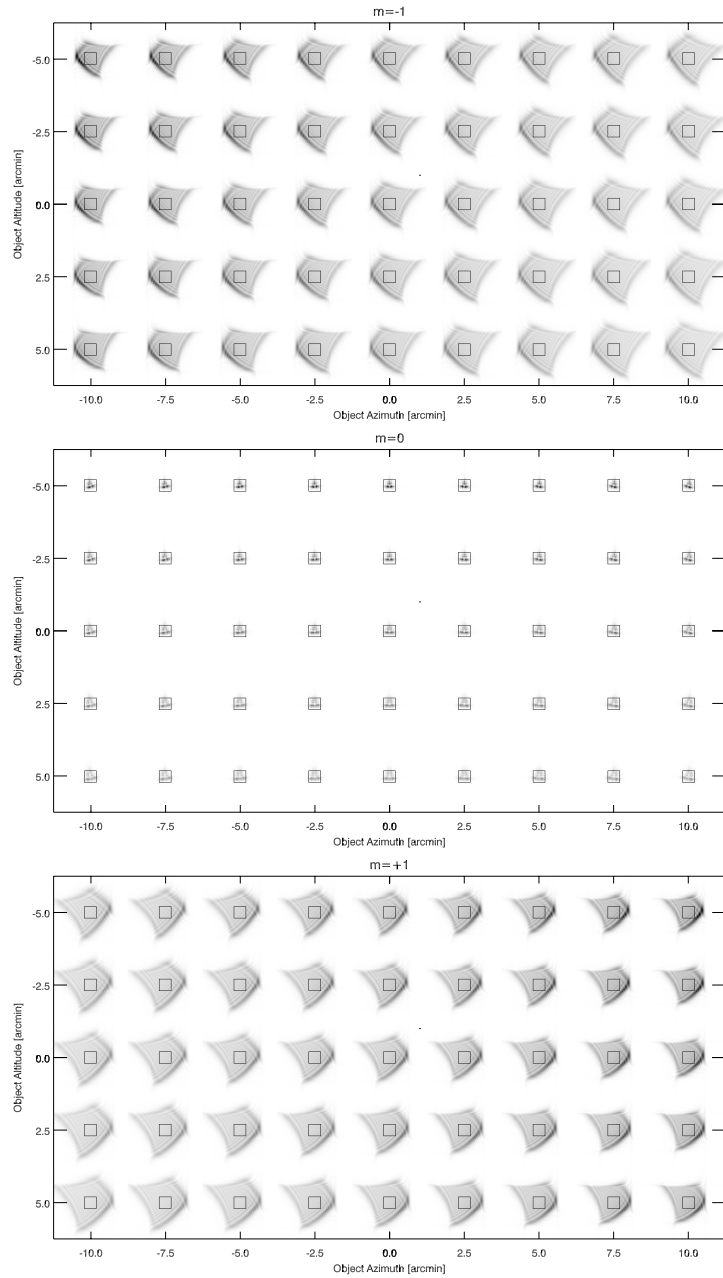


Figure 8.1: Point spread functions in *MOSES-06* three orders for varying field angle. Viewpoint is facing detectors, sun at your back, with positive z towards the top of the page. Superimposed squares represent 13.5 micron pixels.

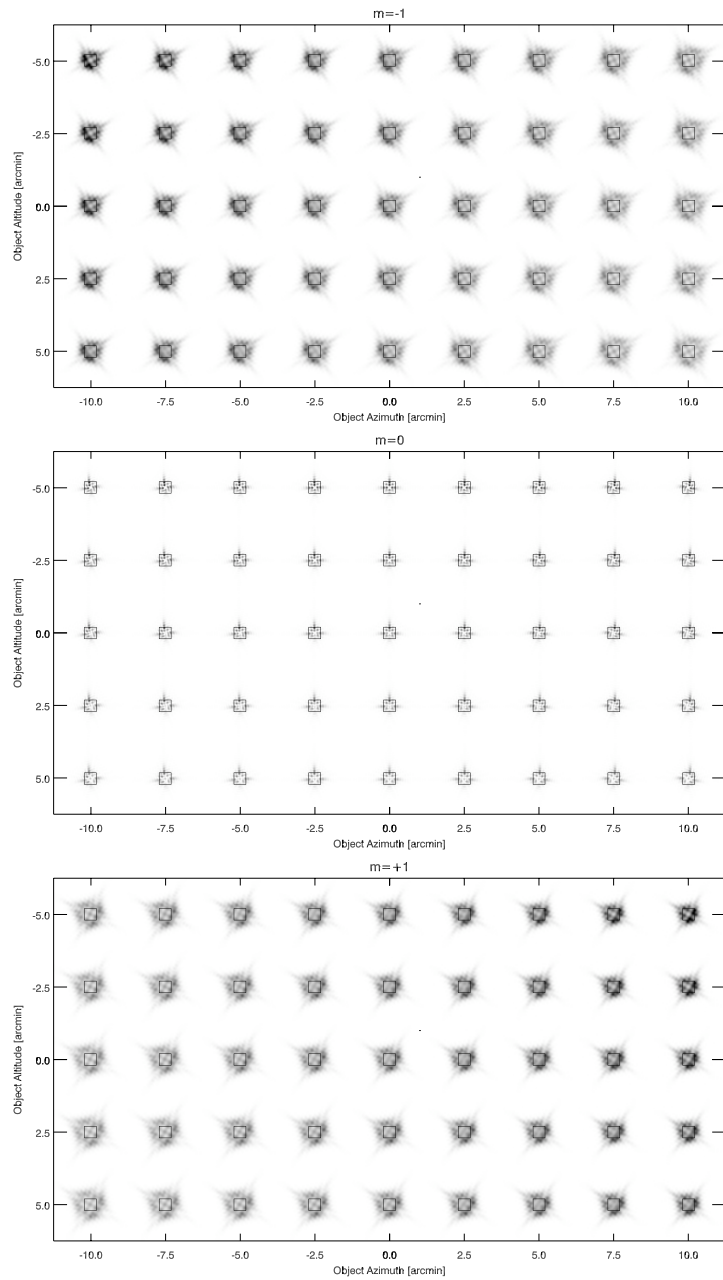


Figure 8.2: Point spread functions in *MOSES-15* three orders for varying field angle using the optical design from table 8.2. Viewpoint is facing detectors, sun at your back, with positive z towards the top of the page. Superimposed squares represent 13.5 micron *MOSES* pixels.

I incorporated the measured figure error of the primary mirror (shown in figure 6.4) into the model as added path difference, and estimated point spread functions pre and post correction. These results are shown in figure 8.3 with spatial sampling of $13.5 \mu m$ (*MOSES-06* CCD sampling).

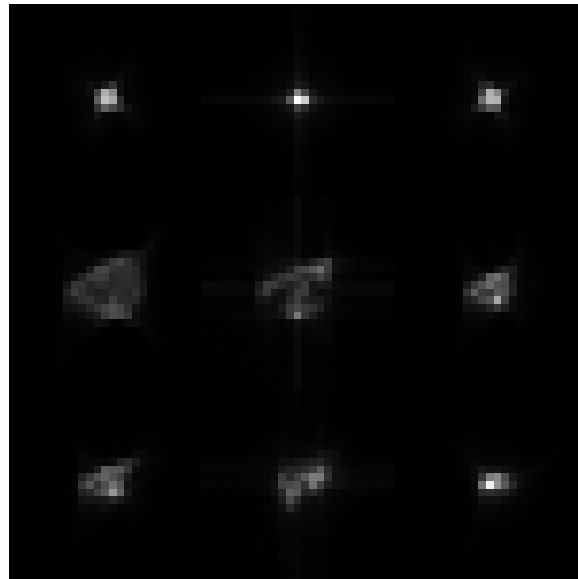


Figure 8.3: Modeled EUV point spread functions. Top Row: point spread functions from perfect primary mirror. Center Row: point spread functions using measured primary mirror figure (§6.1.2). Bottom Row: point spread functions using corrected primary mirror figure (§6.1.3). Left to right column: $m = -1$, $m = 0$, $m = +1$. All point spread functions are normalized to total of one and displayed on the same scale.

The correction shows great promise for improving *MOSES-15* image quality.

8.3.2 Visible Light, Measured and Modeled

Subsequent to alignment, and prior to going to the range, undergraduate student Roy Smart and I measured the $m = 0$ point spread function in visible ($\lambda = 635nm$) light. An interferometer and beam expander arrangement was used, so precise collimation was achieved by adjusting the system until the measured Zernike defocus of a high quality flat mirror interposed into the beam was zero. We repeated the

measurement post flight, and also thought to obscure the central diffracting region of the primary mirror, so the $m = 0$ aperture was approximately as it is at operational wavelength. The results are shown in figure 8.4.

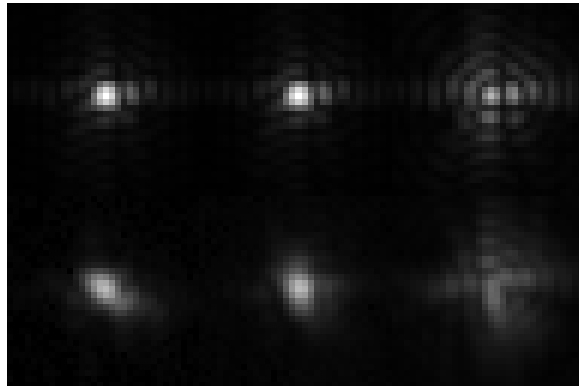


Figure 8.4: Top Row from model: Full aperture, full aperture, central obscuration. Bottom Row measured: Full aperture pre flight, full aperture post flight, central obscuration post flight. Left to right column: $m = -1$, $m = 0$, $m = +1$. All point spread functions are normalized to total of one and displayed on the same scale.

8.4 Distortion Modeling

Optical distortion could be an issue with the *MOSES* spectrograph which is sensitive to alignment between spectral orders. I modeled the optical distortion in *MOSES-06* by comparing focus spot centroids in the detector planes as a function of field angle – $m = -1$ relative to $m = 0$ (figure 8.5), and $m = +1$ relative to $m = 0$ (figure 8.5). The model shows a ramp in distortion which reaches a magnitude of approximately 1 pixel towards the corners of the field of view. The *MOSES-06* digital co-alignment routine employs a linear warping of the images to minimize the impact of distortion. This type of model could be useful to constrain the co-alignment.

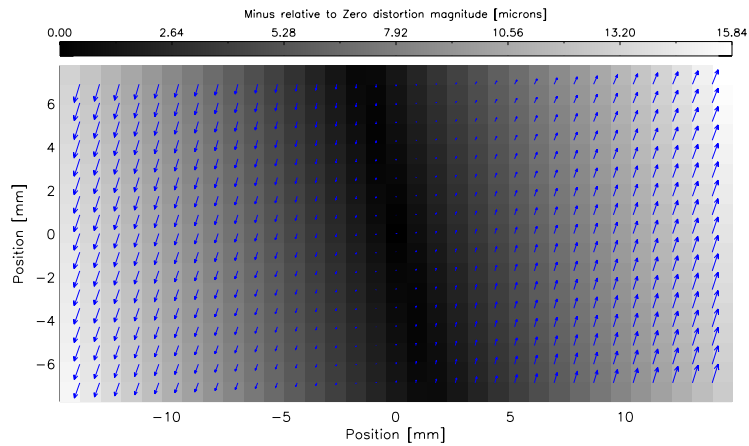


Figure 8.5: Modeled optical distortion in *MOSES-06* $m = -1$ relative to $m = 0$

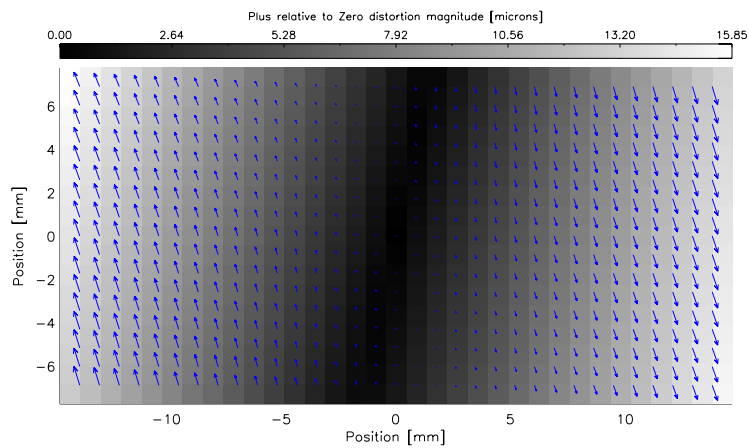


Figure 8.6: Modeled optical distortion in *MOSES-06* $m = +1$ relative to $m = 0$.

8.5 Acknowledgements

I would like to thank Dr. Charles Kankelborg for many helpful discussions about diffraction modeling.

REFERENCES CITED

- Abhyankar, K. D. 1977, Bulletin of the Astronomical Society of India, 5, 40
- Agafonov, M. 2004, Radiophysics and quantum electronics, 47, 85
- Andretta, V., Jordan, S. D., Brosius, J. W., et al. 2000, ApJ, 535, 438
- Anscombe, F. J. 1948, Biometrika, 35, 246. [+http://dx.doi.org/10.1093/biomet/35.3-4.246](http://dx.doi.org/10.1093/biomet/35.3-4.246)
- Arnaud, M., & Rothenflug, R. 1985, A&AS, 60, 425
- Athay, R. G., ed. 1976, Astrophysics and Space Science Library, Vol. 53, The solar chromosphere and corona: Quiet sun
- Athay, R. G. 1984, ApJ, 287, 412
- Bahng, J., & Schwarzschild, M. 1961, ApJ, 134, 312
- Bewsher, D., Brown, D., Innes, D., & Parnell, C. 2004, in ESA Special Publication, Vol. 575, SOHO 15 Coronal Heating, ed. R. W. Walsh, J. Ireland, D. Danesy, & B. Fleck, 465
- Bijaoui, A., & Rué, F. 1995, Signal processing, 46, 345
- Bijaoui, A., & Ru, F. 1995, Signal Processing, 46, 345 . <http://www.sciencedirect.com/science/article/pii/0165168495000934>
- Bracewell, R. N., & Riddle, A. C. 1967, ApJ, 150, 427
- Bray, R. J., & Loughhead, R. E. 1974, The solar chromosphere
- Brosius, J. W., Davila, J. M., & Thomas, R. J. 1998, ApJS, 119, 255
- Brueckner, G. E., & Bartoe, J.-D. F. 1983, ApJ, 272, 329
- Brueckner, G. E., & Nicolas, K. R. 1973, SoPh, 29, 301
- Buehler, D., Lagg, A., van Noort, M., & Solanki, S. K. 2016, A&A, 589, A31
- Cargill, P. 2013, Astronomy and Geophysics, 54, 3.16
- Chae, J., Wang, H., Lee, C.-Y., Goode, P. R., & Schühle, U. 1998, ApJL, 497, L109
- Cranmer, S. R. 2009, Living Reviews in Solar Physics, 6, 3. <http://dx.doi.org/10.12942/lrsp-2009-3>
- Delaboudinière, J. P., Artzner, G. E., Brunaud, J., et al. 1995, Solar Physics, 162, 291. <http://dx.doi.org/10.1007/BF00733432>
- Dere, K. P. 1994, Advances in Space Research, 14, doi:10.1016/0273-1177(94)90154-6

- Dere, K. P., Bartoe, J.-D. F., & Brueckner, G. E. 1984, ApJ, 281, 870
- . 1989, SoPh, 123, 41
- Dere, K. P., Bartoe, J.-D. F., Brueckner, G. E., Cook, J. W., & Socker, D. G. 1987, SoPh, 114, 223
- Dere, K. P., Bartoe, J.-D. F., Brueckner, G. E., Ewing, J., & Lund, P. 1991, J. Geophys. Res., 96, 9399
- DePontieu, B., Title, A. M., Lemen, J. R., et al. 2014, Solar Physics, 289, 2733. <http://dx.doi.org/10.1007/s11207-014-0485-y>
- Dowdy, Jr., J. F., Rabin, D., & Moore, R. L. 1986, SoPh, 105, 35
- Feldman, U. 1983, ApJ, 275, 367
- . 1987, ApJ, 320, 426
- Fox, J. L. 2011, PhD thesis, Citeseer
- Fox, J. L., Kankelborg, C. C., & Thomas, R. J. 2010, ApJ, 719, 1132
- Freeland, S., & Handy, B. 1998, Solar Physics, 182, 497. <http://dx.doi.org/10.1023/A:1005038224881>
- Gabriel, A. H. 1976, Philosophical Transactions of the Royal Society of London Series A, 281, 339
- Gary, G. A. 2001, SoPh, 203, 71
- Gordon, R., Bender, R., & Herman, G. T. 1970, Journal of theoretical Biology, 29, 471IN1477
- Grossmann, A., & Morlet, J. 1984, SIAM Journal on Mathematical Analysis, 15, 723. <http://dx.doi.org/10.1137/0515056>
- Hale, G. E. 1908, ApJ, 28, 315
- Harra, L. K., Gallagher, P. T., & Phillips, K. J. H. 2000, A&A, 362, 371
- Harrison, R. A. 1997, SoPh, 175, 467
- Harvey, K. L., & Martin, S. F. 1973, SoPh, 32, 389
- Hassler, D. M., Dammasch, I. E., Lemaire, P., et al. 1999, Science, 283, 810. <http://science.sciencemag.org/content/283/5403/810>
- Holschneider, M., Kronland-Martinet, R., Morlet, J., & Tchamitchian, P. 1990, in Wavelets (Springer Berlin Heidelberg), 286–297

- Innes, D. E. 2001, A&A, 378, 1067
- Innes, D. E. 2004, in ESA Special Publication, Vol. 547, SOHO 13 Waves, Oscillations and Small-Scale Transients Events in the Solar Atmosphere: Joint View from SOHO and TRACE, ed. H. Lacoste, 215
- Innes, D. E., Guo, L.-J., Huang, Y.-M., & Bhattacharjee, A. 2015, ApJ, 813, 86
- Innes, D. E., Inhester, B., Axford, W. I., & Wilhelm, K. 1997, Nature, 386, 811
- Innes, D. E., & Tóth, G. 1999, SoPh, 185, 127
- Janesick, J. 2001, Scientific Charge-coupled Devices, Press Monograph Series (Society of Photo Optical). <https://books.google.com/books?id=rkgBkbDie7kC>
- Ji, H., & Daughton, W. 2011, Physics of Plasmas, 18, 111207
- Jordan, C. 1975, MNRAS, 170, 429
- Kaczmarz, S. 1937, Bulletin International de l'Academie Polonaise des Sciences, 355
- Kak, A. C., & Slaney, M. 1988, Principles of Computerized Tomographic Imaging (IEEE Press)
- Kankelborg, C., Atwood, S., Courier, H., Plovanic, J., & Rust, T. 2012, in American Astronomical Society Meeting Abstracts, Vol. 220, American Astronomical Society Meeting Abstracts #220, 124.01
- Kankelborg, C. C., & Thomas, R. J. 2001, Simultaneous imaging and spectroscopy of the solar atmosphere: advantages and challenges of a 3-order slitless spectrograph, , doi:10.1117/12.450074. <http://dx.doi.org/10.1117/12.450074>
- Klimchuk, J. A. 1992, in ESA Special Publication, Vol. 348, Coronal Streamers, Coronal Loops, and Coronal and Solar Wind Composition, ed. C. Mattok
- Leighton, R. B., Noyes, R. W., & Simon, G. W. 1962, ApJ, 135, 474
- Lucy, L. B. 1974, AJ, 79, 745
- MacPherson, K. P., & Jordan, C. 1999, MNRAS, 308, 510
- Mariska, J. T. 1986, Annual Review of Astronomy and Astrophysics, 24, 23. <https://doi.org/10.1146/annurev.aa.24.090186.000323>
- Mishra, D., Muralidhar, K., & Munshi, P. 1999, Numerical Heat Transfer Part B - Fundamentals, 35, 485
- Ning, Z., Innes, D. E., & Solanki, S. K. 2004, A&A, 419, 1141. <https://doi.org/10.1051/0004-6361:20034499>

- Owens, S. M., Gum, J. S., Tarrio, C., et al. 2005, Narrow-band EUV multilayer coating for the MOSES sounding rocket, , , doi:10.1117/12.617520. <http://dx.doi.org/10.1117/12.617520>
- Parker, E. N. 1988, ApJ, 330, 474
- Parnell, C. E. 2001, SoPh, 200, 23
- Peter, H. 2001, A&A, 374, 1108
- Petschek, H. E. 1964, NASA Special Publication, 50, 425
- Porter, J. G., & Dere, K. P. 1991, ApJ, 370, 775
- Porter, J. G., Moore, R. L., Reichmann, E. J., Engvold, O., & Harvey, K. L. 1987, ApJ, 323, 380
- Priest, E., & Forbes, T. 2007, Magnetic Reconnection
- Reeves, E. M., Foukal, P. V., Huber, M. C. E., et al. 1974, ApJL, 188, L27
- Richardson, W. H. 1972, J. Opt. Soc. Am., 62, 55. <http://www.osapublishing.org/abstract.cfm?URI=josa-62-1-55>
- Rieutord, M., & Rincon, F. 2010, Living Reviews in Solar Physics, 7, 2
- Rosner, R., Tucker, W. H., & Vaiana, G. S. 1978, ApJ, 220, 643
- Roudier, T., Rieutord, M., Brito, D., et al. 2009, A&A, 495, 945
- Savage, S. L., McKenzie, D. E., & Reeves, K. K. 2012, ApJL, 747, L40
- Scherrer, P. H., Bogart, R. S., Bush, R. I., et al. 1995, SoPh, 162, 129
- Shensa, M. J. 1992, IEEE Transactions on signal processing, 40, 2464
- Starck, J.-L., Murtagh, F., & Bijaoui, A. 1998, Image Processing and Data Analysis: The Multiscale Approach (New York, NY, USA: Cambridge University Press)
- Teriaca, L., Banerjee, D., Falchi, A., Doyle, J. G., & Madjarska, M. S. 2004, A&A, 427, 1065
- Tousey, R., Bartoe, J. D. F., Bohlin, J. D., et al. 1973, SoPh, 33, 265
- van Driel-Gesztelyi, L., & Green, L. M. 2015, Living Reviews in Solar Physics, 12, 1. <http://dx.doi.org/10.1007/lrsp-2015-1>
- Vernazza, J. E., Avrett, E. H., & Loeser, R. 1981, ApJS, 45, 635
- Vernazza, J. E., & Reeves, E. M. 1978, ApJS, 37, doi:10.1086/190539

- von F. Zernike. 1934, *Physica*, 1, 689 . <http://www.sciencedirect.com/science/article/pii/S0031891434802595>
- Wilhelm, K., Marsch, E., Dwivedi, B. N., & Feldman, U. 2007, *SSRv*, 133, 103
- Wilhelm, K., Curdt, W., Marsch, E., et al. 1995, *Solar Physics*, 162, 189. <http://dx.doi.org/10.1007/BF00733430>
- Winebarger, A. R., Emslie, A. G., Mariska, J. T., & Warren, H. P. 2002, *ApJ*, 565, 1298
- Withbroe, G. L., & Mariska, J. T. 1976, *SoPh*, 48, 21
- Withbroe, G. L., & Noyes, R. W. 1977, *ARA&A*, 15, 363

APPENDICES

APPENDIX A

MOVIES

Figure A.1: A movie of a point-like object observed in the *MOSES-06* data. The panels from left to right show \mathcal{I}_{-1} , \mathcal{I}_0 , and \mathcal{I}_{+1} . The morphology of the brightening is dominated by the instrument point spread functions.

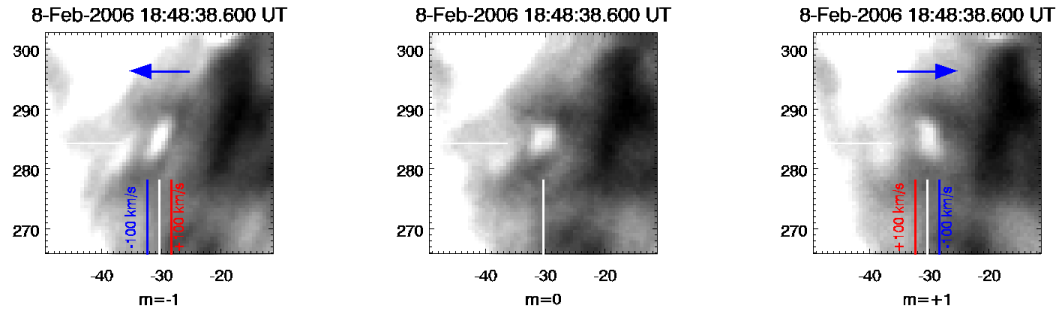


Figure A.2: A movie of a blue shifted jet observed in the *MOSES-06* data. The panels from left to right show \mathcal{I}_{-1} , \mathcal{I}_0 , and \mathcal{I}_{+1} . The brightening is point-like but shifted left in \mathcal{I}_{-1} and right in \mathcal{I}_{+1} indicating a blueshift.

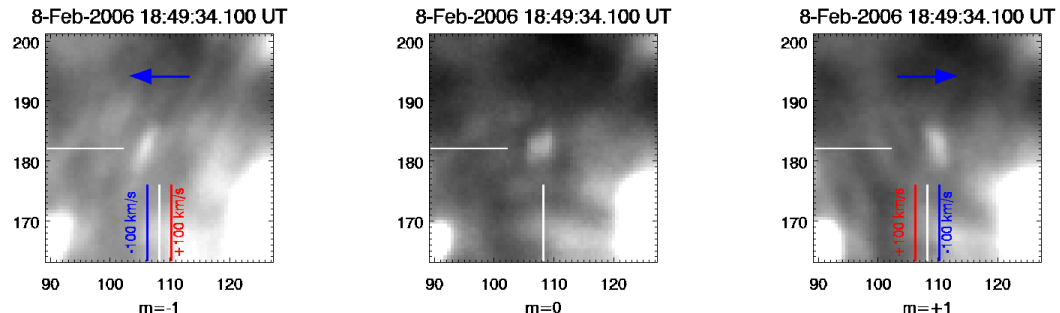
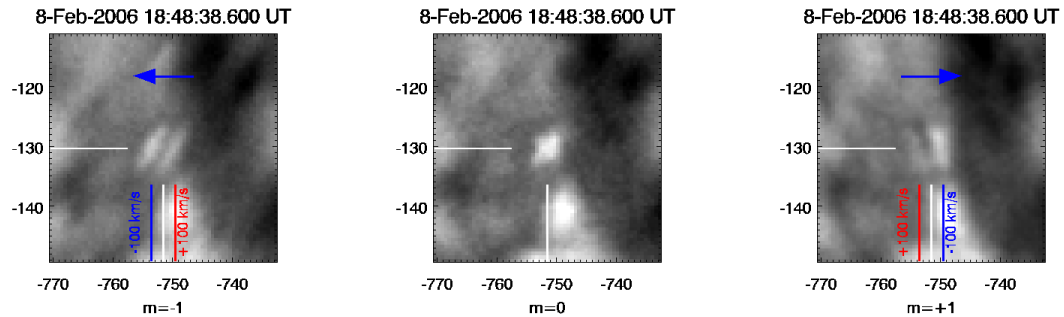


Figure A.3: A movie of a bi-directional jet observed in the *MOSES-06* data. The panels from left to right show \mathcal{I}_{-1} , \mathcal{I}_0 , and \mathcal{I}_{+1} . The brightening has two components in \mathcal{I}_{-1} and \mathcal{I}_{+1} , one shifted right and one shifted left relative to the brightening in \mathcal{I}_0 . The two shifted components indicate a bi-directional jet. A gap between the shifted components shows that very little emission is present from low velocity plasma.



APPENDIX B

THE WAVELET TRANSFORM

The *MOSES-06* observations of the solar transition region exhibit emission at a wide range of intensity and size scales. Using the particular example of explosive events, emission at small size scales (<2'') may be superimposed upon more slowly spatially variable emission. The wavelet transform is a tool for viewing and manipulating image data at different levels of spatial detail (Starck et al., 1998). The wavelet transform has proven invaluable for both qualitative (i.e. visual) and quantitative study of the *MOSES-06* data. As I use the wavelet transform extensively in this dissertation I will explain it in some detail. I begin with a description of the continuous wavelet transform, and then proceed to describe a method to compute the wavelet transform of two dimensional sampled data. The wavelet transform applied to sampled data is referred to as the discrete wavelet transform.

B.1 The Continuous Wavelet Transform

In one dimension the continuous wavelet transform of a function $f(x)$ is defined (Grossmann & Morlet, 1984) as

$$W(a, b) = \frac{1}{\sqrt{a}} \int_{-\infty}^{\infty} f(x) \psi^* \left(\frac{x-b}{a} \right) dx \quad (\text{B.1})$$

where the wavelet function $\psi(x)$ is known.

An inverse transformation exists provided that $\psi(x)$ satisfies an admissibility condition that

$$C_\psi = \int_0^\infty \frac{|\hat{\psi}(\nu)|^2}{\nu} d\nu < \infty \quad (\text{B.2})$$

where $\hat{\psi}(\nu)$ is the Fourier transform of $\psi(x)$:

$$\hat{\psi}(\nu) = \int_{-\infty}^{\infty} \psi(x) e^{-i2\pi\nu x} dx \quad (\text{B.3})$$

The admissibility condition requires that $\hat{\psi}(\nu) \rightarrow 0$ as $\nu \rightarrow 0$; thus the function $\psi(x)$ has mean zero and corresponds to a bandpass filter. If the wavelet admissibility condition is satisfied then the inverse transformation exists and is defined (Grossmann & Morlet, 1984) as

$$f(x) = \frac{1}{C_\psi} \int_0^\infty \int_{-\infty}^\infty \frac{1}{\sqrt{a}} W(a, b) \psi\left(\frac{x-b}{a}\right) \frac{da db}{a^2} \quad (\text{B.4})$$

B.2 The À Trou Discrete Wavelet Transform

Measured data are discrete approximations to continuous functions. A uniformly sampled approximation to the function $f(x)$, $x \in \mathbb{R}$ is the sequence f_k , $k \in \mathbb{Z}$. The à trous algorithm (Holschneider et al., 1990; Shensa, 1992) is a method for computing the wavelet transform of discretely sampled data.

In the à trous algorithm one specifies a smoothing kernel h_k^0 rather than a wavelet function ψ . h_k^0 corresponds to a low pass filter and is normalized to unity total. The sequence f_k is sequentially smoothed by dilations of h_k^0 to produce a set of sequences c_k^j , beginning with $c_k^0 \equiv f_k$. The index j will be referred to as the *scale* of the transform. The inner product of two sequences p_k and q_k is defined as

$$\{p * q\}_k = \sum_{k'} p_{k'} q_{k'-k} \quad (\text{B.5})$$

The c_k^j are generated iteratively for $j \geq 0$ as

$$c_k^{j+1} = c_k^j * h^j \quad (\text{B.6})$$

where the dilations of the smoothing kernel are defined as

$$h_k^{j+1} = \begin{cases} h_{k/2}^j & \text{if } k/2 \in \mathbb{Z} \\ 0 & \text{otherwise} \end{cases} \quad (\text{B.7})$$

The dilations are made by inserting zeroes between the elements of the filter h_k^0 , hence the name à trous, which means *with holes*.

The c_k^j are progressively smoother approximations to the sequence f_k . In the passage from $c^j \rightarrow c^{j+1}$ detail present at scale j is lost due to the smoothing in B.6. This lost detail defines a set of *wavelet coefficients*:

$$w_k^{j+1} = c_k^j - c_k^{j+1}, \quad j > 0 \quad (\text{B.8})$$

In order to understand the significance of the wavelet coefficients consider that w^{j+1} can be calculated directly from f_k via

$$w^{j+1} = f_k * \psi_k^j \quad (\text{B.9})$$

Using equations B.6 and B.8 the kernel ψ_k^j is evidently

$$\psi_k^j = h_0 * h_1 * \dots * h_{j-2} * (\delta_k - h_k^{j-1}) \quad (\text{B.10})$$

The kernel δ_k is the identity operator. From equation B.10, it is apparent that ψ_k^j has mean zero, and thus satisfies the wavelet admissibility condition (equation B.2). Equation B.9 is therefore a discrete wavelet transform.

Following Starck et al. (1998), I will use the following kernel to compute the à

trous discrete wavelet transform (DWT) throughout this work:

$$h_k^0 = \begin{cases} 3/8, & k = 0 \\ 1/4, & |k| = 1 \\ 1/16, & |k| = 2 \\ 0, & \text{otherwise} \end{cases} \quad (\text{B.11})$$

Figure *B.1* shows the filters that produce the first few scales of the wavelet transform, along with the low pass filter that produces the smoothed residual image. The passage from wavelet space back into real space is simple: one sums all wavelet scales and the smoothed residual image. This is seen in the sum of the filters in figure *B.1*. The filters sum to one at all frequencies. The à trous filters are seen to be a series of bandpass filters. This is how the discrete wavelet transform achieves resolution in both space and frequency.

The two dimensional à trous discrete wavelet transform is calculated simply by extending the convolutions into two dimensions and using a new convolution kernel $h_{kq}^0 = h_k^0 h_q^0$. A tilde over an image will be used to denote the à trous transform of that image.

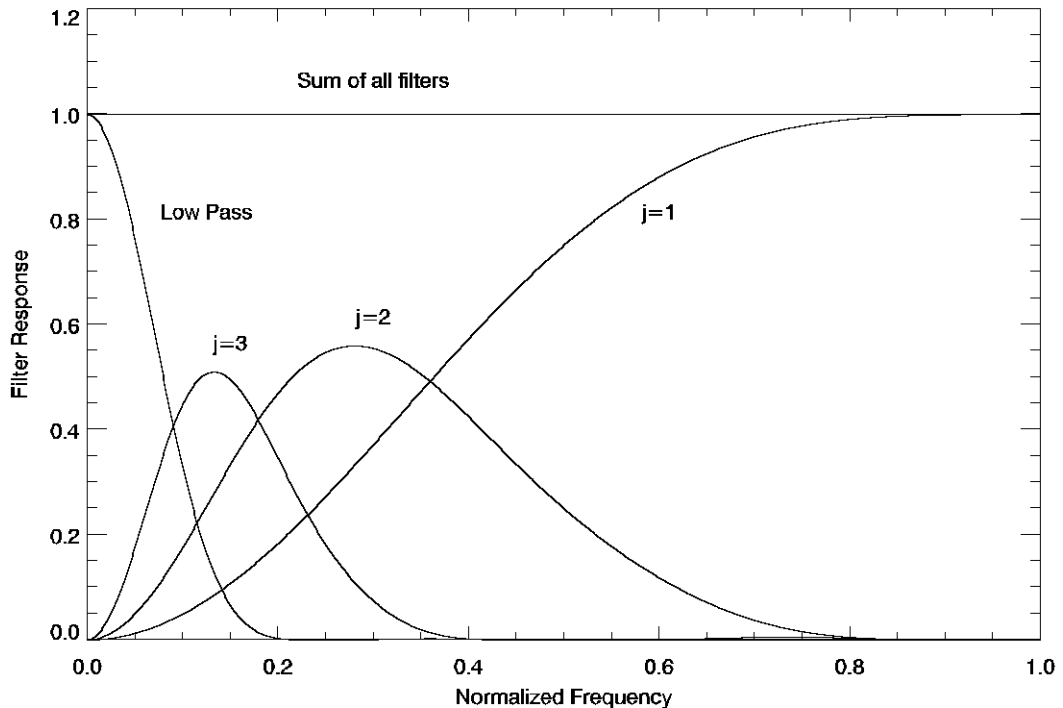


Figure B.1: Frequency response of à trous wavelet filters up to scale $j = 3$, and the low pass filter which gives the smooth residual image. The sum of all filters is equal to one.

B.2.1 Significance Testing of Discrete Wavelet Coefficients

The wavelet coefficients of a noisy image are noisy. When working with noisy images, statistical significance testing can be done on the w^j to differentiate signal from noise (Starck et al., 1998). The utility of this resides the fact that noise typically exists at all image scales, whereas an image feature often occupies only a small range of scales. Whether a coefficient is determined to be significant depends on the amplitude of the coefficient relative to possible values given the image noise distribution.

The *MOSES-06* images show Poisson distributed photon shot noise plus gaussian distributed read out noise (appendix C). Signal independent wavelet significance

testing of images with this signal dependent noise model is facilitated with the Anscombe transformation (Anscombe, 1948) $\mathcal{I} \rightarrow \hat{\mathcal{I}}$. Similar to square root scaling, with the detector gain accounted for, application of the Anscombe transformation to an image results in a new image whose noise is uniform additive gaussian distributed. The distribution of the wavelet coefficients of gaussian noise is gaussian (Starck et al., 1998), with standard deviation σ_j at the j th scale.

Significant wavelet coefficients of an image \mathcal{I} are determined from $\hat{\mathcal{I}}$. I adopt the hard threshold of $3\sigma_j$. If $|\tilde{\mathcal{I}}(x, y, j)| > 3\sigma_j$ then $\tilde{\mathcal{I}}(x, y, j)$ is significant, and assumed to indicate real signal in the data. If $|\tilde{\mathcal{I}}(x, y, j)| < 3\sigma_j$ then $\tilde{\mathcal{I}}(x, y, j)$ may have arisen from the noise and is considered to be noise.

APPENDIX C

NOISE MODELING

C.1 Introduction

I develop an image noise model for the *Multi Order Solar EUV Spectrograph* (*MOSES*) instrument. *MOSES* records images using 3 2048x1024 rear illuminated CCDs. Analog to digital conversion is 14 bit. I use the photon transfer curve method (Janesick, 2001). Each CCD was exposed to varying levels of visible light, and the noise characteristics were analyzed. Excellent agreement was found with a model that includes only Poisson distributed photon shot noise and gaussian distributed read out noise. This model is described by two parameters - the read out noise variance and the gain. The read noise variance is directly measured, and the gain is deduced from the noise statistics. Analysis is also made of the noise in image data obtained by Fox (2011) for estimation of the CCD flatfield variation. Nominal illumination wavelength for these images is 30.4 nm - *MOSES* operating wavelength. The noise in these appears smooth relative to the noise in the visible light images. This is characteristic of charge diffusion which is well known to occur in CCDs operating at UV to X ray wavelengths (Janesick, 2001). Using power spectral densities, I derive a kernel that describes the probability of the diffusion of photoelectrons to neighboring pixels. I conclude with a discussion of *MOSES* noise in wavelet transform space.

C.2 Theory

CCD operation relies on the photoelectric effect, where incident photons interact with lattice electrons to generate free electrons in the material. Electronic circuitry on the chip is used to produce a grid of potential wells, known as pixels, which trap the free electron at or near the location it was generated. The total charge collected in each pixel is then measured and converted to a digital number [DN]. The image produced by a CCD is an array of numbers, one for each pixel, whose values are

proportional to the amount of charge collected in each pixel.

The idealized CCD is a linear system which converts some number of interacting photons P into a digital number S [DN], and is described by

$$S = G * \eta * P \quad (\text{C.1})$$

The quantum yield η (e^- photon $^{-1}$) is the number of free electrons generated as the result of a single photon/lattice interaction. For photons with wavelengths longer than 400 nm the quantum yield is unity. For shorter wavelengths, free electrons may be produced with sufficient kinetic energy to free other lattice electrons, and $\eta > 1$. For extreme ultraviolet 30.4 nm photons interacting with silicon, $\eta = 11.12 e^-$ photon $^{-1}$. The constant G (DN e^-) is the CCD gain, the analog to digital conversion constant from a number of electrons to DN. In the following the constant η will be subsumed into G for notational simplicity. At visible and longer wavelengths $G = G\eta$ because $\eta = 1$. At wavelengths less than 400 nm the constant $G\eta$ represents an effective gain; see section C.6.

Repeated measurements of S under identical exposure conditions will result in variation about a mean value \bar{S} . This variation is called noise. Under dark conditions, when the illuminating photon flux is zero, noise in the analog to digital (A/D) conversion process results in a fluctuation of S about zero (or more typically, a pedestal value greater than zero). This type of noise is called read out noise and is well described by a gaussian distribution with variance σ_R^2 (DN). In addition, free electrons are generated from thermal fluctuations in the CCD material, which produce measurable signal and consequently noise. This is called dark current, as signal is produced even under dark conditions, and the associated noise is Poisson distributed. At the operating temperature of *MOSES* CCDs dark current is effectively

non existent, but is present in room temperature measurements.

Read out noise is the same for each pixel in the CCD, as the charge in each pixel is measured by a single A/D converter. In principle, the quantity σ_R^2 is determined by calculating the variance of a single short exposure, known as a bias exposure. In practice, bias frames taken at room temperature will be corrupted by dark current, whose associated noise will exceed the read noise component. An upper bound to the read noise is obtained from a room temperature bias frame, by calculating the variance of the first few rows of the image, which are read out first and thus have the least amount of time to accumulate dark current. The resulting estimate differs little from a similar value estimated from bias frames taken with a cooled CCD.

When exposed to light S also exhibits noise due to variation σ_P^2 in the number of photons which interact with the CCD in a particular exposure. The number of interacting photons, or counts, is described by a Poisson distribution. If the average number of interacting photons \bar{P} is sufficiently great ($\bar{P} > 10$), the Poisson distribution is approximately gaussian with variance $\sigma_P^2 = \bar{P}$. This approximation becomes exact as $P \rightarrow \infty$. Dark current, if present, contributes signal with $\eta = 1$ and Poisson distributed noise, and is indistinguishable from signal generated by illuminating visible light photons.

Together, then, Poisson plus gaussian distributed noise sources constitute the basic noise model describing the variation in S:

$$\sigma_S^2 = G^2 \sigma_P^2 + \sigma_R^2 \quad (\text{C.2})$$

Given sufficient counts, $\sigma_P^2 = \bar{P}$, and from C.1 $\bar{S} = G\bar{P}$, so

$$\sigma_S^2 = G\bar{S} + \sigma_R^2 \quad (\text{C.3})$$

The unknowns on the RHS of *C.3* are G and σ_R^2 . Once determined, the error (variance) on a measured pixel value \bar{S} is simply determined from this linear equation. The quantities \bar{S} , σ_S^2 , and σ_R^2 in *C.3* may all be calculated from direct measurement. It is possible to calculate these values for each pixel in the array, but a large volume of data must be collected in order to obtain good statistics. Alternatively, the statistics may be calculated over NxN arrays of adjacent pixels within a single CCD image taken under spatially uniform illumination. I chose the latter alternative given constraints on the volume of data that could be obtained with the *MOSES* without overloading the thermal capacity of the system.

In an ideal system, therefore, good statistics are obtainable from a single image and G is determined by rearranging *C.3*. In practice, G itself varies somewhat from pixel to pixel. This variation is known as flatfield variation, so called because it is typically mapped using deep exposures with flat illumination. Flatfields were measured by Fox (2011), using creativity to overcome lack of a flat EUV source. Flatfield variation is repeatable, not noise, but adds a variance term to *C.3* that goes as the square of \bar{S} when statistics are taken over a group of adjacent pixels. For that matter, spatial variation in the illumination of the CCD will also generate such a term, and will dominate the linear term whose slope allows determination of G . These quadratic terms may be removed by differencing, pixel by pixel, two identical exposures. Since uncorrelated random noise adds in quadrature the variance of this difference image is twice that of equation *C.3*. Therefore the difference image must be divided by $\sqrt{2}$ before calculating the variance called for in equation *C.3*. In practice the estimate for G is improved by taking exposures at varying signal levels, from a bias exposure up through saturation, and fitting a line to the measured difference image variance less the read out noise variance.

C.3 Methods

C.3.1 Light Source

The CCDs were illuminated with specially designed LED light sources, which operate at 635 nm. The wavelength was chosen so that $\eta = 1$. The LEDs were mounted in a light tight tube, which was threaded into a flange which bolted directly to the filter tube mounting holes on the camera housing. Mounted in the tube between the CCD and the LED was an opal glass diffuser, designed to approximate a Lambertian source. The CCD/light source system is closed to outside light. The LEDs are controlled by a driving circuit which turned on the lights when triggered by the shutter open signal from the *MOSES* flight computer. The LED on signal is a square pulse, one per *MOSES* exposure, and the time interval is set with a function generator. Knowing the exact on time of the LED is not critical, but it is important that back to back exposures could be made with the same LED on time, so that the difference images have the signal variance given in C.2.

C.3.2 Data

Data was collected on 2012 September 9. 10 bias exposures, exposure length 1 ms, were taken both at the beginning and the end of the experiment for measurement of read noise. Following the first 10 bias images, and prior to the last 10 bias images, 10 dark exposures with exposure times of 1 s were taken for measurement of the image pedestal. The dark sequences were triggered by the “DARK” uplinks on the *MOSES* ground station - no shutter open signal is sent, so the LED sources are not activated. The light exposures were done with the “DATA START” uplink. The light exposure sequence consisted of two one second exposures, with two exposures per sequence for difference image generation. The LED on time was set with the function generator,

with times ranging from $1\ \mu\text{s}$ to 0.4 s . After setting the LED on time, the sequence was initiated, with two exposures per sequence, each exposure sending the shutter open signal which triggered the LEDs. After the sequence was complete, the LED on time was increased, and another sequence was run. These 55 exposures cover the full range of the CCD analog to digital conversion, from bias to full well. 55 sequences, with 2 exposures per sequence, and 3 CCDs results in 330 light images at varying signal levels. A sample image is shown in figure C.1. The curve of signal variance versus signal is known as a photon transfer curve.

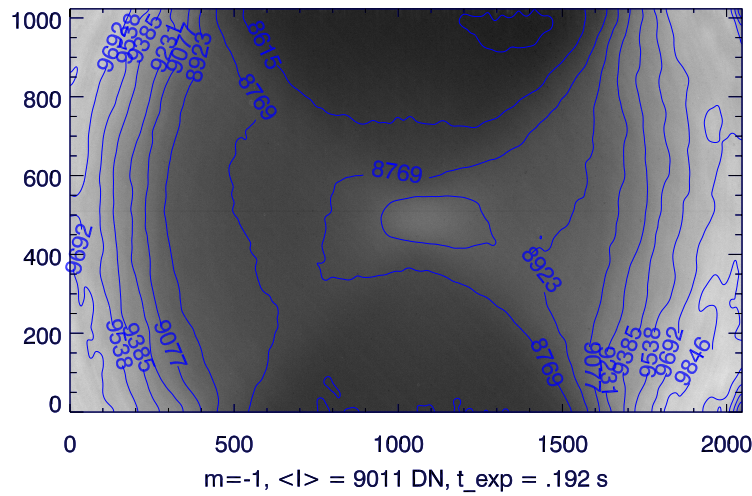


Figure C.1: Image produced with the illumination device described in §C.3.1. This image is taken with the $m = -1$ CCD; the other CCD illumination patterns are similar in appearance.

C.4 Analysis

C.4.1 Read Noise and Pedestal Measurement

This experiment was performed at room temperature. Signal accrues in the CCD pixels at all times due to dark current, which is subject to shot noise and thus

corrupts measurement of read out noise. Each CCD exposure consists of a flush, in which all charge is cleared from all pixels, integration of charge during the exposure time, followed by read out, where the accrued charge is converted to DN. The flush is a fast operation; all pixels are effectively zeroed at the same time. Read out, however, takes approximately four seconds. Each pixel is read sequentially, meaning the last pixel in the array has four seconds more time to accrue dark current. Thus, although the dark exposures have 1 ms exposure times, the last rows to be read have an effective exposure time of four seconds as far as dark current is concerned. Therefore read noise was estimated from the first two rows of the CCD to be read, giving 4096 pixels to produce statistics, with an effective exposure time of approximately 5 ms. For reasons similar to those described above, the image pedestal was measured using the first two rows of the 1 s dark exposures where the dark current is small.

C.4.2 Signal Mean and Variance Measurement

Difference images were generated by taking the two light exposures at each LED on time, differencing them, and dividing by $\sqrt{2}$. As discussed in section C.2 the factor of $\sqrt{2}$ is necessary because the noise present in the differenced images adds in quadrature leading to a factor of 2 on the right hand side of C.3 which must be accounted for. The mean image was the average of the two images, less the pedestal. Estimates of the signal and variance were generated by calculating the mean and variance of NxN arrays within the images, centered at random locations. 1000 estimates were made for each LED on time. N was varied to investigate the effect of box size on the results.

C.5 Results

Results for each CCD are shown graphically in figures *C.2*, *C.3*, *C.4* for the $m = -1$, $m = 0$, and $m = +1$ CCDs respectively. The data is plotted in log scale in order to show the variation in the curve in the read out noise regime. All three plots show a slope of 1 over the full A/D range after subtraction of the read out noise, indicating excellent agreement with the expected linear relationship between the mean signal and the signal variance. These curves show the mean signal and variance values generated using a box width of 45 pixels.

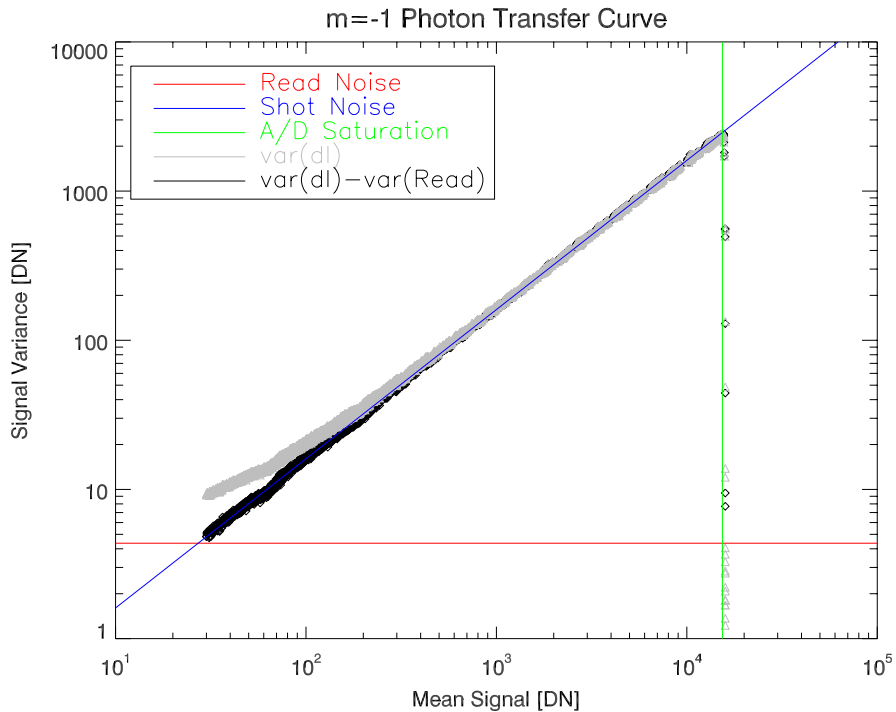


Figure C.2: Photon transfer curve for $m = -1$ CCD. The data is plotted on log-log axes to show the various signal regimes. At low signal, the presence of read noise (magnitude of variance indicated by horizontal red line) results in a deviation of the transfer curve from unity slope (gray curve). At higher signal the read noise becomes insignificant compared to the Poisson distributed shot noise, and the curve takes on a characteristic slope of one, until A/D saturation is reached and the variance drops precipitously, as all pixel values approach $2^{14}-1$ DN (vertical green line). When the read noise variance is subtracted from the total signal variance, the Poisson limited linear curve extends all the way to the zero signal level, indicating good estimation of the read noise variance. For reference the theoretical curve for pure Poisson noise is overplotted as a blue line of slope 1.

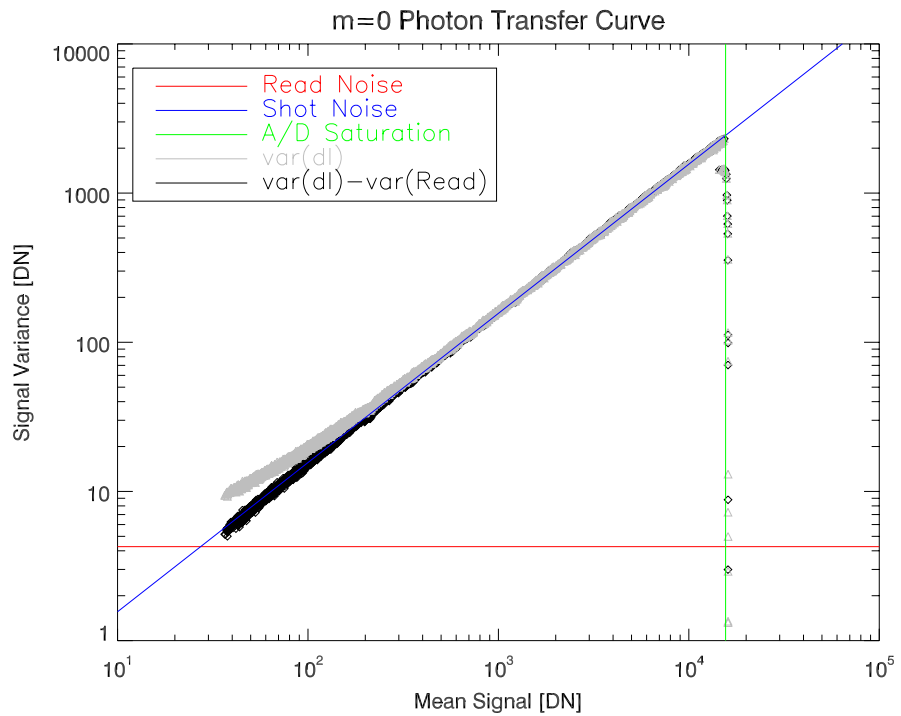


Figure C.3: m=0 CCD Photon transfer curve. See figure C.2 caption for further details.

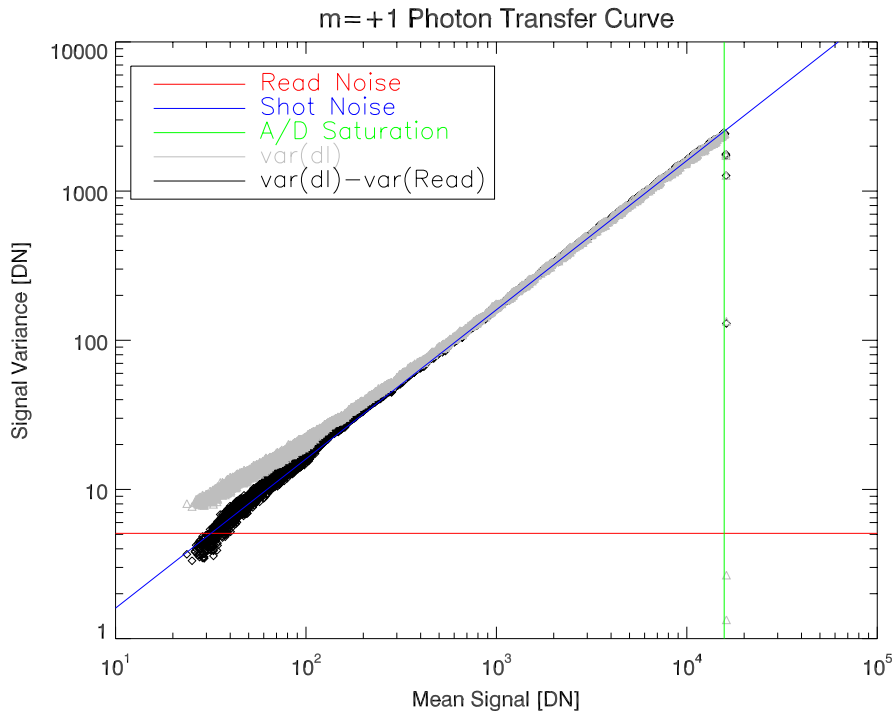


Figure C.4: $m=+1$ Photon transfer curve. See figure *C.2* caption for further details.

The gain G is estimated by dividing the signal variance, less the read noise variance, by the signal mean. The read noise estimate is accurate, as after subtraction from the total variance the transfer curve becomes linear even at low signal (figures *C.2*, *C.2* and *C.2*); however, I choose to estimate the gain using data points where the signal is between the values of 5000 DN and 14000 DN. At these signals, read noise is negligible, so any effect of read noise estimation errors on the gain estimation will be minimized. The upper bound keeps the estimates well below the region where the signal variance falls off due to A/D saturation. The gain estimates are shown graphically in figures *C.5*, *C.6*, *C.7* for $m = -1$, $m = 0$, and $m = +1$ respectively.

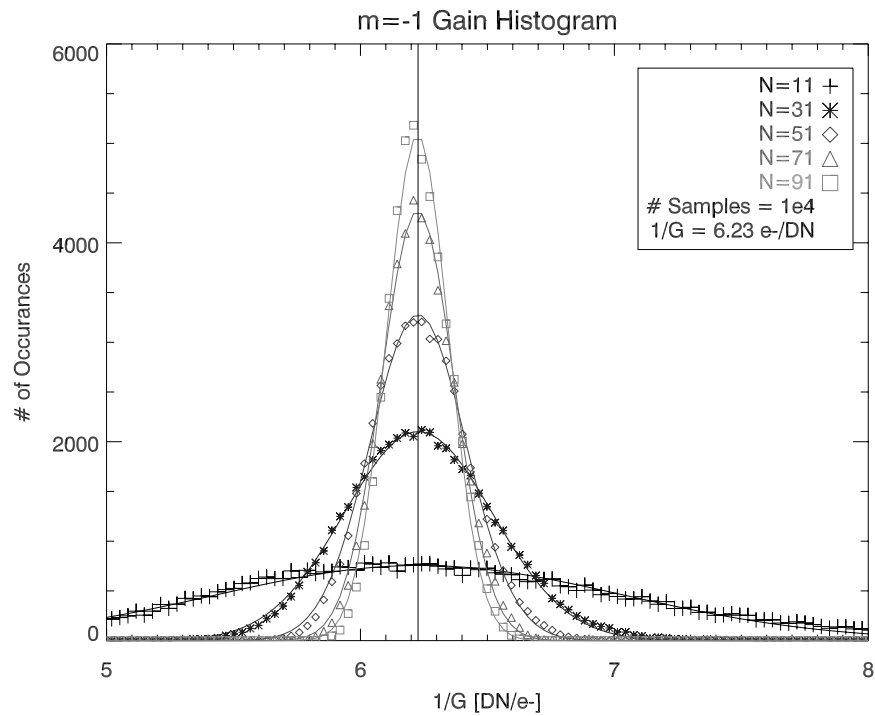


Figure C.5: Histograms of estimated value of $1/G$ for the $m = -1$ CCD. The statistics are generated using $N \times N$ sub arrays of the noise images. As N is varied, the width of the histogram (which may be taken as an error estimate on the gain) varies, but the centroid remains the same. The symbols represent data, the solid lines are gaussian fits. The gain estimate results from averaging the centroids of the gaussian fits.

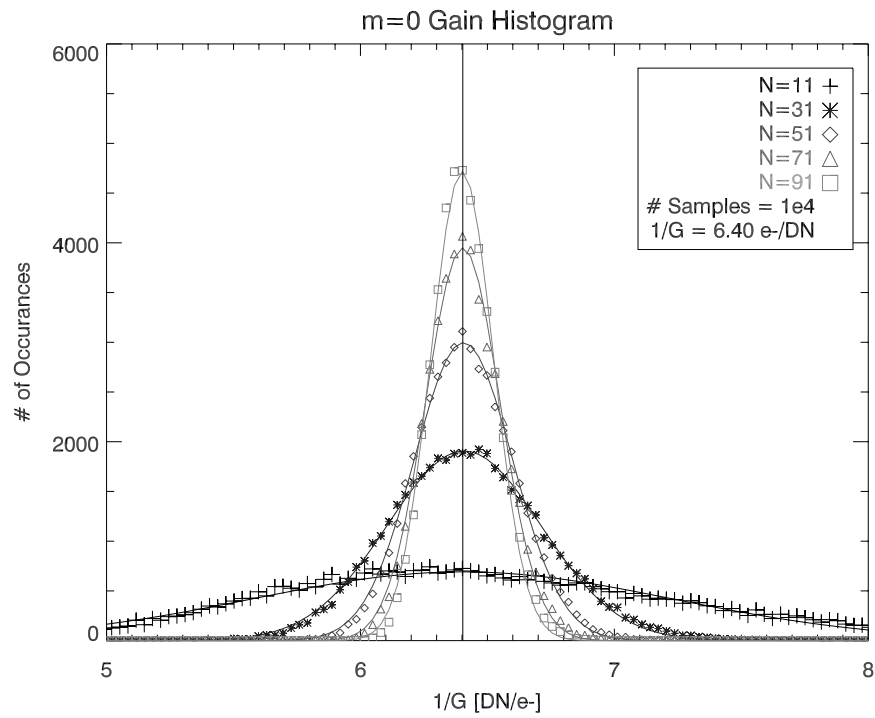


Figure C.6: Histograms of estimated value of $1/G$ for the $m = 0$ CCD. See caption of figure C.5 for further details.

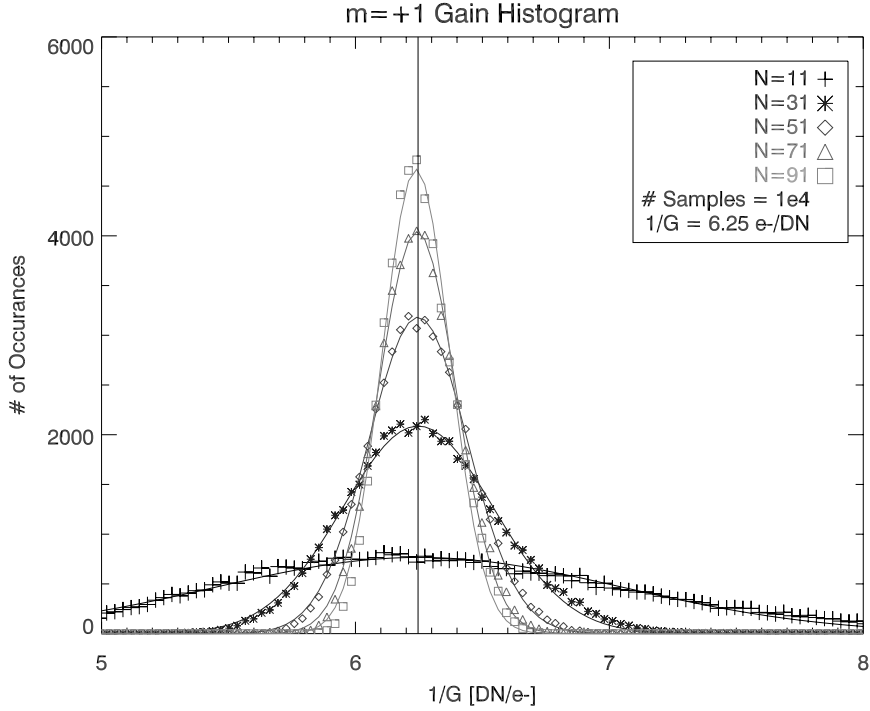


Figure C.7: Histograms of estimated value of $1/G$ for the $m = +1$ CCD. See caption of figure C.5 for further details.

The gain estimates are shown plotted as histograms. The different histograms correspond to different choices of box size in which the statistics were calculated. It is seen that box size affects the width of the histograms, but the centroid, which gives the gain, remains unchanged. The symbols represent measured histogram values; the solid lines are gaussian fits to the histograms. The gain histograms show a gaussian distribution, and the mean of the distribution is the estimate for the gain.

The measured noise in visible light is in excellent agreement with a model incorporating only photon shot noise and readout noise (i.e., eq. C.3). This model is fully determined by the gain G and variance of the readout noise σ_R . The measured values of these parameters are given in table C.1.

Table C.1: Noise Model Parameters. See equation C.3.

CCD	G [DN/e-]	$\sigma_R^2[DN]$
m=-1	0.161	4.4
m=0	0.156	4.3
m=+1	0.158	5.1

C.6 Noise at Operating Wavelength

Fox (2011) used an extreme ultraviolet source in combination with a nominal HeII 304 multilayer mirror to illuminate the *MOSES* CCDs at operating wavelength for measurement of the CCD pixel to pixel gain variation (flatfield). Metallic thin film filters were used to filter out visible light. These data are also useful for investigating the noise properties of the CCDs at operating wavelength. As noted above, one expected difference is the effective gain is different, as $\eta > 1$. For a wavelength of 30.4 nm, $\eta = 11.12$ e-/photon. The effective gain, then, at this operating wavelength for, e.g., the $m = -1$ detector is $G_{EUV} = G\eta = 1.77$ DN/photon.

A typical image is shown in figure C.8. Average exposure level is just over 10^4 DN, about 2/3 of the way to A/D saturation. This image is taken with the $m = -1$ detector. As above, the noise is accessed by differencing two images made under the same exposure conditions.

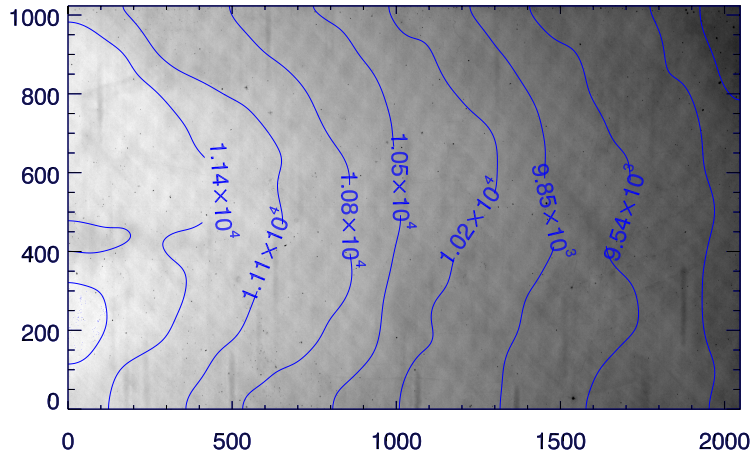


Figure C.8: Image produced with EUV illumination of the $m = -1$ CCD; the other CCD illumination patterns are similar in appearance. The contours are smoothed. The underlying grid pattern is produced by the thin metallic filter used to block visible light.

Comparison of the noise in the visible light images and the EUV images is facilitated by use of the generalized Anscombe transformation (Anscombe, 1948; Starck et al., 1998). Application of this transformation to an image containing (signal dependent) Poisson noise plus gaussian distributed read noise results in a new image, whose noise is gaussian distributed with standard deviation of 1. The Anscombe transformation is applied to the images prior to differencing, then the standard difference image is computed. The gain used for the visible light images ($m=-1$ detector) is that from table C.1; the gain used for the EUV data is G_{EUV} .

Figure C.9 shows overlapped 128x128 pixel sub images extracted from the noise from the (Anscombe transformed) EUV data (lower left), (Anscombe transformed) visible light data (center), and a gaussian distributed noise image, standard deviation 1, generated with a random number generator (synthetic noise).

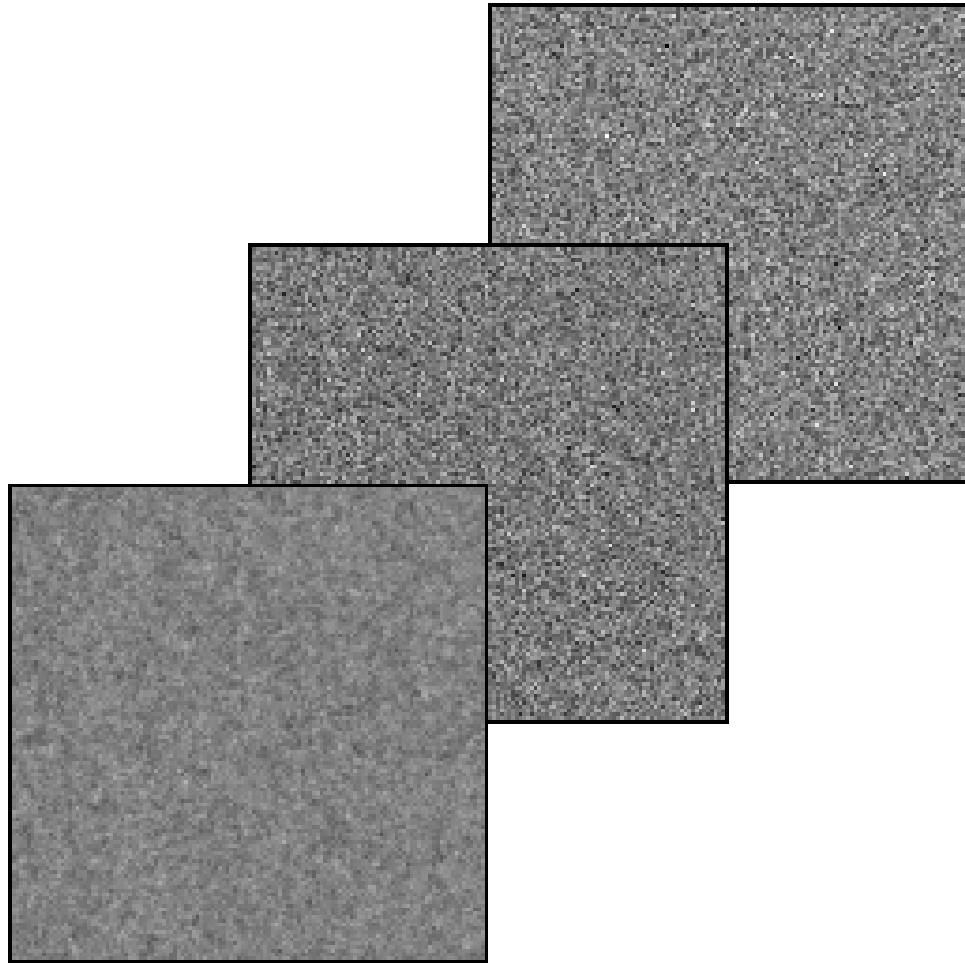


Figure C.9: Noise from various sources: Synthetic (upper right), visible light measurement, $m = -1$ CCD (center), and EUV measurement, $m = -1$ CCD (lower left). All noise images are displayed on the same scale.

The noise from the visible light data appears identical to the synthetic noise; the EUV noise appears to have been smoothed. This is likely due to imperfect charge collection efficiency at EUV wavelengths (Janesick, 2001). The *MOSES* CCDs are rear illuminated devices. For a variety of reasons it is impractical or not possible for the electric fields which define the pixel volumes to extend to the rear (illuminated) surface of the device, leading to a thin layer of field free material. The depth at which a typical EUV photon/electron interaction occurs is also very shallow, thus

many interactions occur in the field free regions. Electrons which are excited in the field free region will random walk through the material, until by chance they encounter the electric field defining a pixel and are captured. As lateral movement may occur in this walk the capturing pixel may not be the one closest to the site of excitation. This imperfect charge collection efficiency is sometimes referred to as charge diffusion or charge spreading. This is investigated in the following sections, first using power spectra derived with the Fourier transform. Subsequently the noise properties are examined in wavelet space.

C.6.1 Noise Power Spectra

Power spectra are estimated from the noise as the absolute square of the Fourier transform of 128x128 pixel sub images drawn from random locations in the noise images. 1000 power spectra are estimated from each noise source and averaged to reduce noise in the estimated power spectra. These power spectra are shown in figure C.10.

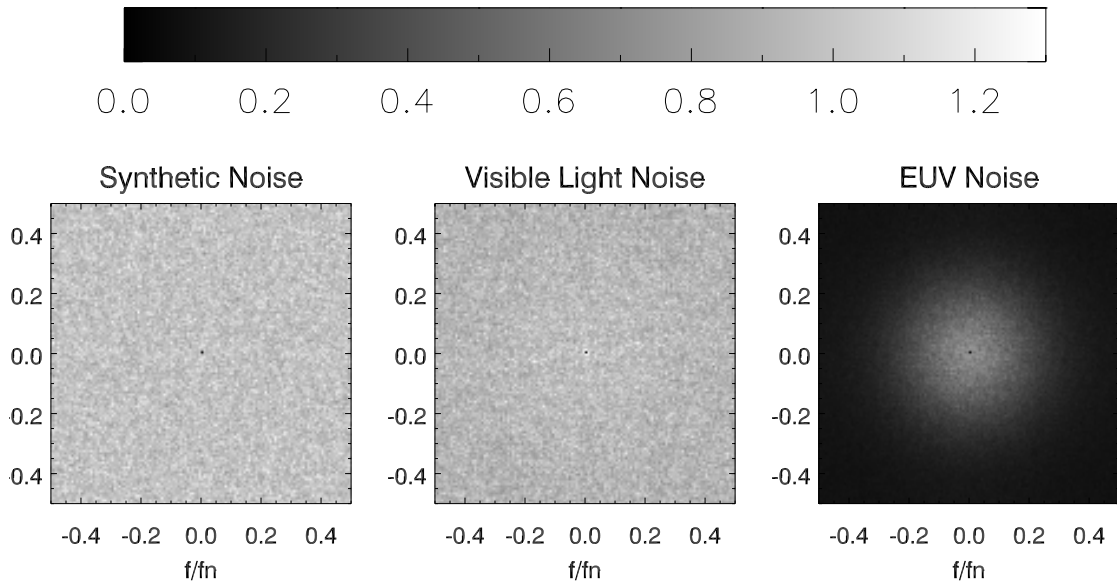


Figure C.10: Power spectral densities of noise from synthetic (left), visible light (center), and EUV (right) data. All panels are displayed with the same scale.

The synthetic, gaussian distributed noise has equal power at all frequencies, a property referred to as white noise. The visible light noise appears to share a white noise spectrum; the EUV noise, however, falls off isotropically as the magnitude of the frequency increases. This type of noise is referred to as red noise, as more power exists at low frequencies, and is most likely the result of charge diffusion at EUV wavelengths.

It is possible to attribute a smoothing kernel to this power spectrum. The interpretation of this kernel is the probability that an electron will be captured by a pixel in the neighborhood of the pixel nearest the interaction site. If randomly distributed noise ϵ is convolved with smoothing kernel κ , the power spectrum of the result is $PS = |\tilde{\epsilon}|^2 |\tilde{\kappa}|^2$. If the initial noise has a white power spectrum then $|\tilde{\epsilon}|^2 = 1$,

and the power spectrum of the smoothed noise is equal to the power spectrum of the kernel. Given the interpretation of the kernel it must be real, and I assume it is symmetric; such a kernel has a real Fourier transform, which is equal to the square root of its power spectrum, i.e., $\tilde{\kappa} = \sqrt{PS}$. Following this logic, the charge diffusion kernel is estimated by inverse transforming the square root of the EUV power spectrum. Very few pixels of the result differ appreciably from zero; a 3x3 kernel is sufficient to describe the diffusion. The kernel is normalized to sum to 1 as befits a probability distribution. The values of the charge diffusion kernel are shown in table C.2.

Table C.2: Charge Diffusion Kernel κ . Values represent the probability of a free electron being captured by a pixel in the neighborhood of the interaction site.

.034	.077	.034
.076	.558	.076
.034	.077	.034

C.6.2 EUV Noise in Wavelet Space

The wavelet transform is extremely useful for image processing where features of various size scales exist at well defined locations, as is typical for images of real world scenes, and therefore it is useful to discuss noise in the context of wavelets. Given discrete (pixellated) data, of interest is the discrete wavelet transform. The particular algorithm used here is the à trous discrete wavelet transform (see appendix B). Other algorithms would result in different numbers, but the same analysis may be applied.

Application of the à trous transform to an LxM size image results in an LxMxN array, consisting of N-1 wavelet coefficient images and one smoothed image. The

original image is recovered exactly by summing over the N dimension. In the presence of noise, the wavelet coefficients are randomly distributed about the true value, with the distribution based on the noise present in the image. Knowledge of the noise in wavelet space allows significance testing of coefficients, which is useful in wavelet noise reduction, deconvolution regularization, and other applications where one might wish to know whether a coefficient is indicative of real signal, or has arisen from random noise.

Wavelet coefficient significance levels are determined by the noise present in the data. The Anscombe transformation and generalizations thereof may be used to transform signal dependent (e.g., Poisson) noise present in the data to uniformly distributed gaussian noise. In such cases, the distribution of wavelet coefficients due to the noise is determined by applying the wavelet transform to uniform gaussian noise, and calculating the standard deviations σ_j of the coefficients at each scale j. Significance testing is carried out by comparing the wavelet coefficients of the Anscombe transformed data to the σ_j . Coefficients whose magnitudes are sufficiently in excess of σ_j can be said to indicate real signal, rather than having arisen from the noise.

In the presence of charge diffusion, I assume that a.) the A/D gain measured in visible light is correct, and b.) that the charge diffusion kernel is independent of signal level. Under these assumptions the significance levels are determined as above, with the wavelet transform applied to the Anscombe transformed EUV noise from §C.6, using G_{EUV} for the CCD gain.

The significance levels are shown in figure C.11 for uniform gaussian noise, (Anscombe transformed) visible light noise, and (Anscombe transformed) EUV noise.

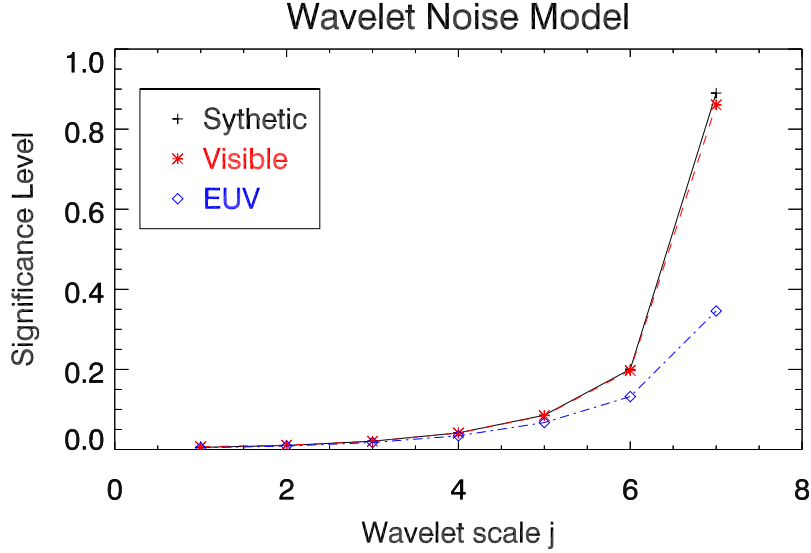


Figure C.11: Significance levels as function of wavelet scale for the à trous transform applied to different noise sources. The significance levels are reduced in the EUV data, as the noise is smoothed due to charge diffusion. Note that signal to noise does not increase, as the signal is smoothed accordingly.

Unlike the Fourier space power spectrum, white noise in wavelet space has increased variance at small scales, and decreases at larger scales. The Anscombe transformed visible light data shows the same significance levels as the synthetic noise, as indeed, it has been transformed into uniformly distributed gaussian noise. Of most interest for *MOSES* data analysis is the significance levels measured from the EUV noise, where charge diffusion results in lower variance in the noise at small scales, tracking again with the gaussian noise at larger scales. It is important to point out that this reduced variance does not improve detection, as the charge diffusion that smooths the noise also smooths the image signal, reducing intensity and sharpness of small scale image features.

This analysis was carried out for all three detectors. The $1-\sigma$ significance levels of Anscombe transformed *MOSES* data under the à trous transformation for each

detector are shown in table C.3.

Table C.3: Wavelet space significance levels from the à trous transform. Size scale decreases as j increases.

j	$m = -1$	$m = 0$	$m = +1$
1	.005	.005	.005
2	.01	.01	.01
3	.019	.019	.019
4	.037	.037	.037
5	.073	.073	.074
6	0.14	0.14	0.14
7	0.37	0.35	0.36

C.7 Acknowledgements

Many thanks to Pat Lokken for design and construction of the LED driver circuit, which was instrumental in obtaining good photon transfer data. I also wish to thank Lewis Fox and Roger Thomas for the use of their EUV flatfield data, Hans Courrier and Norm Williams for contributions to the design and fabrication the LED light sources, and Hans Courrier and Bo Glaspey for assistance in electronic integration of payload, function generator and LED driver circuit.

APPENDIX D

MOSES-06 POINT SPREAD FUNCTIONS

D.1 Introduction

The *Multi-Order Solar EUV Spectrograph* (*MOSES*) (Fox et al., 2010) is designed for slitless imaging spectroscopy of the solar transition region. Co-temporal image and spectral information are obtained over a wide field of view by recording images \mathcal{I}_m at three spectral orders $m = -1$, $m = 0$, and $m = +1$ of a concave diffraction grating. Spectra are recovered through a tomographic inversion.

Fox (2011) noticed significant differences between the point spread functions in each order, and discussed the potential for systematic error. The problem is discussed further in chapter 3. A reasonable estimate for the core of the point spread functions would at minimum contribute to understanding the propagation of systematic errors in *MOSES-06* inversions. Better, the estimates could be incorporated into the inversion algorithm to achieve reduced error and improve spatial and spectral resolution.

Features exist at a range of size scales and shapes in the *MOSES-06* data, but the smallest features in the image in a given order all take on very similar shape. I will argue that these features are unresolved, and the shapes are representative of the core of the point spread function in that order. Inspection of the full data sequence indicates gradual time variation in the point spread functions over the 5 minute flight. This is likely due to thermal expansion in the primary mirror mount.

The \mathcal{I}_0 images abound with unresolved features, and the point spread function is easy to see. Unresolved features are more difficult to find in the dispersed orders \mathcal{I}_{-1} and \mathcal{I}_{+1} because many compact features show strong doppler shifts (see chapter 2). A feature must be unresolved both spatially and spectrally for the point spread function to govern the shape. Such features exist in the data; they may be examples of transition region blinkers (Harrison, 1997). In this appendix I use wavelet methods

to estimate *MOSES-06* point spread functions directly from the data.

D.2 Partial Reconstruction

Wavelet methods have been used to reconstruct objects within an image based on a subset of image wavelet coefficients (Bijaoui & Rué, 1995; Bijaoui & Ru, 1995). This success of this approach reflects the fact that many objects are sparse in wavelet space. An object is generally described by a local maximum among positive, significant coefficients in wavelet space. Significant wavelet coefficients which are connected to the maximum in both scale and space are part of the same object. The object coefficients therefore occupy a volume in wavelet space.

The goal of partial reconstruction is to create an image whose wavelet coefficients are the same as those of the object, within the volume on which the object is defined. If the reconstructed image is p , the object coefficients are \tilde{q} , and A is the operator which transforms p and projects the result onto the support of \tilde{q} , the partial reconstruction problem is minimization of $\|Ap - \tilde{q}\|$. The solution method is iterative, beginning with $p(x, y) = 0$:

1. Initialize $p(x, y) = 0$
2. Calculate $Ap = \tilde{p}(x, y, j)$
3. Determine the additive error in the coefficients on the support of the object:

$$\tilde{\epsilon} = \tilde{p} - \tilde{q}$$

4. Threshold $\tilde{\epsilon}$; retain only statistically significant (3σ) coefficients
5. Calculate correction $\epsilon(x, y) = A^{-1}\tilde{\epsilon}$
6. Update $p = p + \epsilon$

7. Threshold $p > 0$
8. Iterate steps 2 through 7. Iterations end when no significant coefficients may be found in $\tilde{\epsilon}$

The operator A^{-1} is inverse to the operation A . A projects an image into a list of wavelet coefficients; A^{-1} back projects a list of wavelet coefficients into an image. See Bijaoui & Ru (1995). Step 3 was added as a wavelet based goodness of fit criterion.

D.3 Data

The data are from 2006 February 8 flight of *MOSES-06*. Images have been dark subtracted, corrected for flat field, cleaned of cosmic ray hits, and coaligned. Figure D.1 shows a full \mathcal{I}_0 image, overlaid with regions of interest. The field of view in the red square and its wavelet decomposition are shown in figure D.2. The green boxes indicate the locations of numerous compact sources in this image, shown in figure D.7 in §D.6.

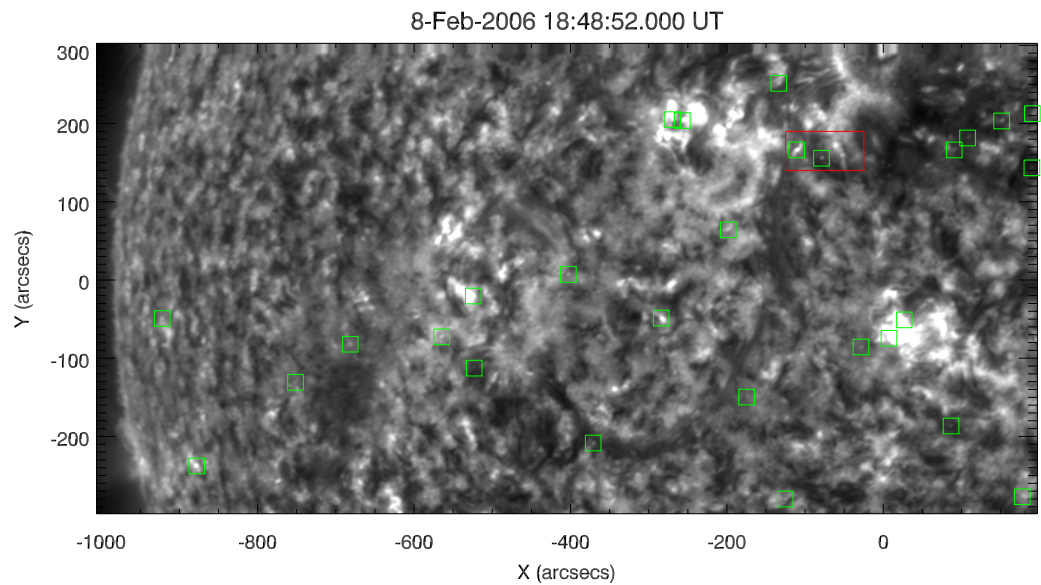


Figure D.1: Context image. Full *MOSES-06* field of view. Over plotted, the red square is shown close up in figure *D.2*. The green squares indicate the compact sources shown in figure *D.7*.

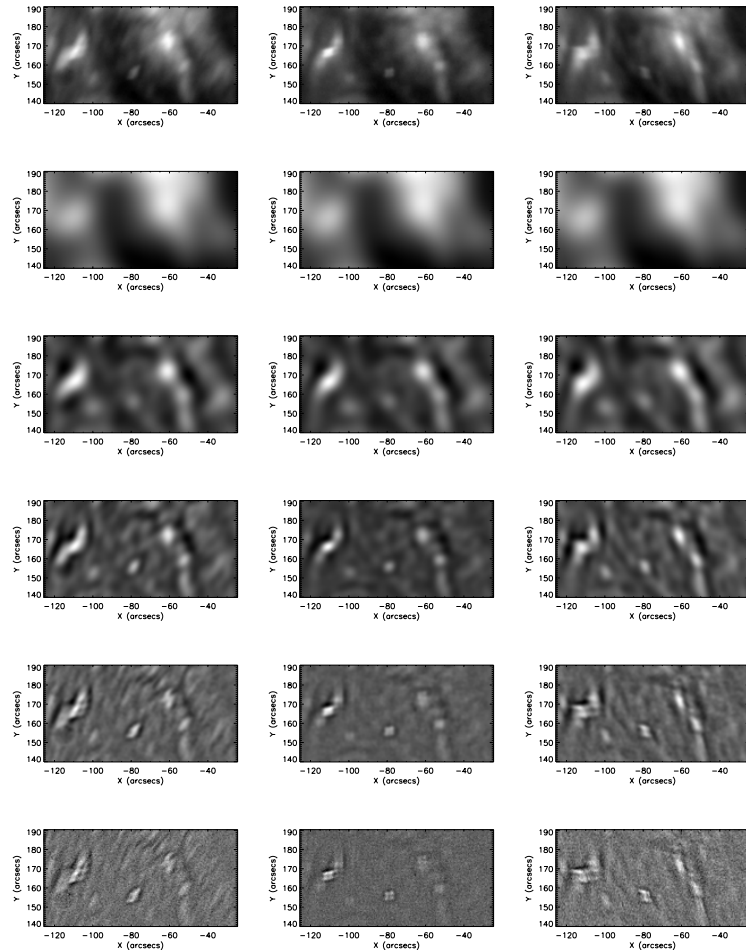


Figure D.2: Close up of the region bounded in red in figure D.1, and its wavelet transform up to scale 4. Original images top row, $m=-1,0,1$ left to right. Wavelet residual (smoothed images \mathcal{I}_s^N) second row. Wavelet scales 4 through 1 are third through last rows. The bright object center left was the subject of a paper by Fox et al. (2010). The shape of the core is dominated by the instrument point spread function, as is the compact source just below center frame.

The features in figure *D.2* clearly show the influence of the instrument point spread functions, particularly the bright core in the object center left and the compact object just below center. The imaging elements, different in each image – right leaning slash in \mathcal{I}_{-1} , rectangular shape in \mathcal{I}_0 , and left leaning slash in \mathcal{I}_{+1} , are seen all over the images (see §*D.6*), and gradually change with time (see §*D.5*)

D.4 PSF Results

An appropriate image feature was selected for point spread function estimation. The feature is long lived, lasting at least 15 exposures with minimal change in appearance and no strong spectral signatures. The object was defined in the first two wavelet scales. The reconstruction results for each spectral order are shown in figures *D.3-D.5*. Estimates are made from a single exposure, taken midway during the flight.

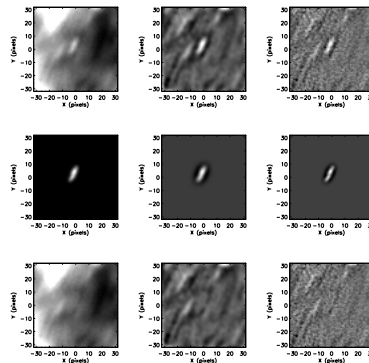


Figure D.3: Reconstruction of a compact source for point spread function estimation, $m=-1$ spectral order. Each row shows an image on left, with the first and second wavelet scales to the right. Top row: original image. Middle Row: Extracted object/point spread function estimate. Bottom Row: Original image minus object.

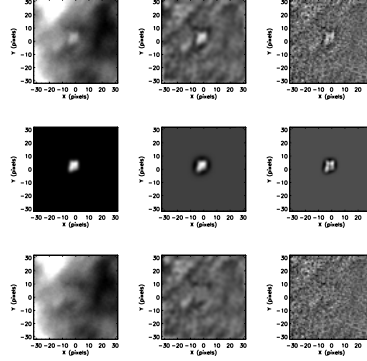


Figure D.4: Reconstruction of a compact source for point spread function estimation, $m=0$ spectral order. Each row shows an image on left, with the first and second wavelet scales to the right. Top row: original image. Middle Row: Extracted object/point spread function estimate. Bottom Row: Original image minus object.

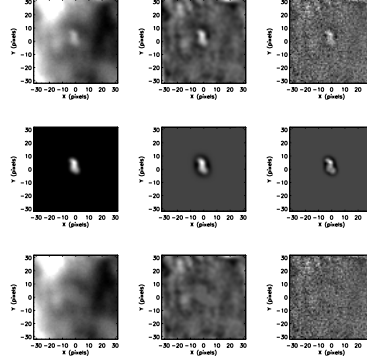


Figure D.5: Reconstruction of a compact source for point spread function estimation, $m=+1$ spectral order. Each row shows an image on left, with the first and second wavelet scales to the right. Top row: original image. Middle Row: Extracted object/point spread function estimate. Bottom Row: Original image minus object.

The reconstruction algorithm works very well, resulting in smooth reconstructions which are consistent with the noise in the images. Full width half max of the point spread function estimates are approximately 6 pixels in each order. This is well in excess of *MOSES-06* design resolution. The size and shapes of the point spread functions are consistent with significant defocus. This combined with the

design astigmatism in the dispersed orders (spherical mirror imaging off axis) results in the slashed appearance of those point spread functions. Six pixels corresponds to approximately 3.5" spatial resolution or 180 km s^{-1} spectral resolution.

D.5 Temporal Variation

Examination of a time series of compact sources shows that the point spread functions change over the course of the five minute flight. This may be a thermal expansion effect. Figure D.6 shows time series of \mathcal{I}_0 , centered on a small region in the *MOSES-06* field of view which shows considerable fine scale structure. The bright compact features all have a similar shape at a given time but that shape changes over the time of flight. The changing shape is likely due to changes in the instrument point spread functions, possibly due to thermal expansion effects.

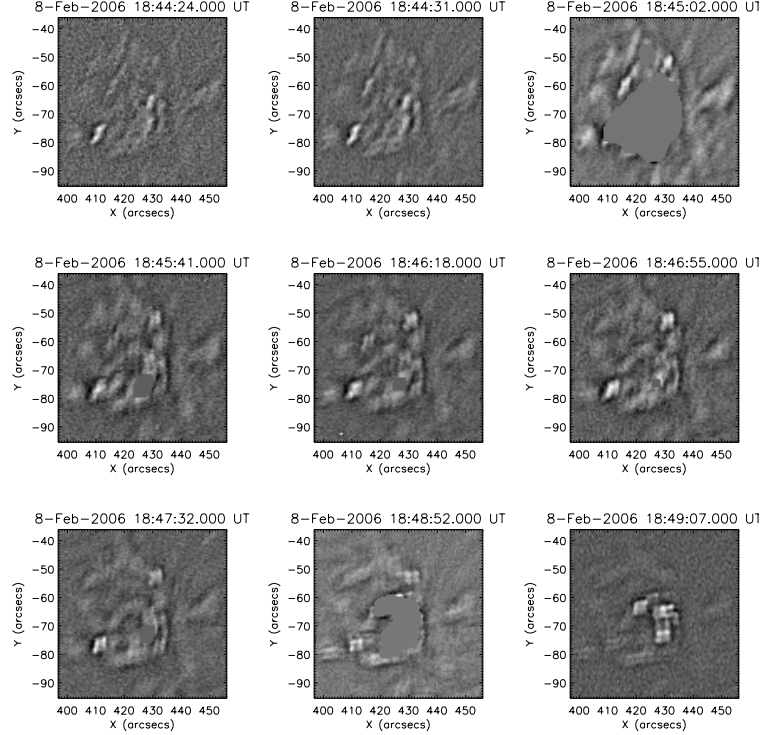


Figure D.6: The small active region, \mathcal{I}_0 data scale 1 wavelet coefficients. Each frame is at a different time, covering most of the flight with time increasing from upper left to lower right. Exposures numbers are 1, 2, 4, 6, 10, 14, 18, 23 and 25, of 27 total, going in order from upper left, left to right, top to bottom. UT shown in the titles of the individual panels.

D.6 Additional Compact Sources

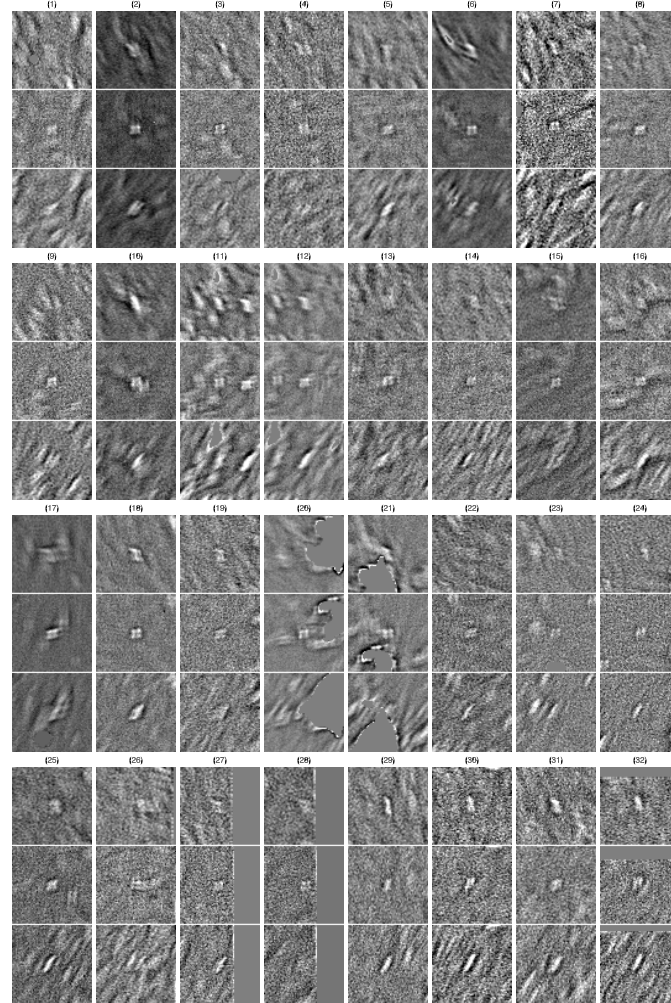


Figure D.7: Panels show the scale $j = 1$ wavelet coefficients of the compact objects from figure D.1. Each panel has three frames that show, from top to bottom, the $m = +1$, $m = 0$, and $m = -1$ data.

D.7 Conclusion

Repeated patterns observed in small scale coefficients of wavelet transformed *MOSES-06* image data can be explained only as artifacts due to the image point

spread functions. I selected a suitable compact, isolated emission source in the data that was then extracted via partial reconstruction from wavelet coefficients, yielding estimates for the instrument point spread functions. Point spread function widths are significantly in excess of the instrument resolution specification. The point spread function morphologies are consistent with telescope defocus, combined with design astigmatism.

Time variance is seen in the point spread functions, probably the result of thermal expansion in the optical system upon exposure to sunlight. The change in point spread function is most rapid during the first quarter of the flight; subsequent changes are more subtle. The point spread functions estimated in this chapter use data from mid flight and may not well represent the instrument point spread functions in early flight exposures.